ION IMPLANTATION DAMAGE IN QUARTZ

BY

R.G. MACAULAY-NEWCOMBE, B.Sc., M.Eng.

A Thesis

Submitted to the School of Graduate Studies

in Partial Fulfilment of the Requirements

for the Degree

Doctor of Philosphy

McMaster University

ION IMPLANTATION DAMAGE

IN QUARTZ

DOCTOR OF PHILOSPHY (1991) McMASTER UNIVERSITY

(Materials Science and Engineering) Hamilton, Ontario

TITLE: Ion Implantation Damage in Quartz

AUTHOR: Richard George Macaulay–Newcombe, B.Sc (McMaster University)
M.Eng. (McMaster University)

SUPERVISOR: Dr. D. A. Thompson

Number of Pages: xii, 135

Abstract

This thesis is a report on a series of measurements of ion-bombardment effects on α-quartz crystals. Damage was produced in α-quartz (single-crystal SiO_2) by bombarding with ions of $^4He^+$ to $^{209}Bi^{++}$ in the energy range of 15 - 200 keV, at both 300 K and $\leq$ 50 K. The samples were analysed *in – situ* with Rutherford backscattering/channeling, using 1 - 2 MeV $^4He^+$ ions; data was obtained from both the oxygen and silicon peaks, so that damage stoichiometry could be calculated. At low ion fluences ($\sim 10^{10}$ - 10^{11} ions/mm^2) the apparent damage level increases linearly with fluence, but at rates of about 3 - 19 times greater than predicted by the modified Kinchin-Pease equation. At higher fluences ($\sim 10^{11}$ - 10^{12} ions/mm^2) the rate of damage increases with fluence for elastic energy deposition rates of less than $\approx$ 0.08 eV/atom, but remains constant for greater elastic energy deposition rates. At even higher ion fluences saturation of the damage occurs. It has been observed that the analysis beam creates damage at a rate dependent on the level of damage already present in the crystal; furthermore, the damage created by the analysis ions appears to be predominantly due to the inelastically deposited energy. Strain effects seem to greatly exaggerate the level of damage indicated by simple channeling calculations. A simple model is proposed to explain both the high rates of damage production and the non-stoichiometry of the damage. The model indicates that the effects of elastic energy deposition, inelastic energy deposition, strain produced by damage, and lattice relaxation into a "quasi–amorphous" state. all contribute to the apparent damage levels synergistically.

ACKNOWLEDGEMENTS

I wish to thank my supervisors, Dr. D. A. Thompson, Dr. J. A. Davies, Dr. W. W. Smeltzer and Dr. G. R. Piercy for their patient support and guidance while this thesis was being produced.

I also wish to thank the many fellow students who have shared with me their knowledge and experience, and made the research process somewhat easier and much richer than it would have been otherwise, especially Doris Stevanovic, M. Eng., Dr. Nalin Parikh, Dr. Skip Poehlman, Dr. Usman Akano and Dr. Ahmed Ibrahim.

This thesis was typeset using TEX, which in itself was an educational process, and would have been impossible without the considerable help and expertise of Jon Simkins of Softfocus.

Thanks are due to the many technicians and machinists whose help enabled me to get my experiments started, and get them going again when things went wrong.

I want to thank my many friends for their encouragement and pointed humour as I made "just a few more changes", especially Connie and Terry DeForest, Jon Simkins, Cheryse LaRocque, F. Gherys and all the members of my family.

Most of all, I thank my wife and best friend, Gale, for the love and humour which has sustained me, and the patient typing and editing as we journeyed from word processor to word processor.

Table of Contents

Table Captions

Figure Captions

CHAPTER I: INTRODUCTION

Quartz, silicas, glasses and other silicates have been objects of study for thousands of years. This is not surprising, since silicon and oxygen together make up 75% of the Earth's crust. Almost as soon as radiation was discovered, its effects on glasses began to be noticed. It was observed that impact by high-energy particles and photons made glasses glow, and caused chemical and structural changes. Later it was noticed that natural quartz crystals which contained radioactive materials (such as uranium) had developed "quasi-amorphous" regions. These regions were different both in density and structure from amorphous silica, and were labelled "metamict."

A considerable amount of effort has gone into the study of radiation-induced changes in the optical properties of quartz and silica. This knowledge has been applied to the manufacture of optical filters, to electro-optics (especially for the formation of waveguides on electro-optic devices), and to quartz crystals made for use as oscillators in high radiation environments.

More recently, silicate-based glasses have become candidates for nuclear waste disposal, the idea being that high-level wastes could be mixed into melted glass. After solidification the mixture would be sealed in steel drums and deposited in deep vaults within a stable hard-rock formation of the Canadian Shield, or some similar location. Hence it is necessary to establish how the radiation damage may affect the structural stability of the waste-glass matrix and the rate of leaching by groundwater. Since the glass will be required to contain the nuclear waste over a very long time scale (of the order of a million years), it is important to determine how the radiation damage builds up with time (dose). Table 1.1 contains estimates by Tait [1981] of the integrated doses to waste glasses with 1% elemental fission product loading, the products of

reprocessing UO_2 fuel or ThO_2/PuO_2 fuel.

Table 1.1: Integrated dose (α/g) for reprocessed waste–glass
(waste from reprocessing partially–burned fission reactor fuel)

	Time (y)		
Fuel	100	10^4	10^6
UO_2	2.9×10^{16}	1.9×10^{17}	6.3×10^{17}
ThO_2/PuO_2	1.93×10^{17}	1.25×10^{18}	4.42×10^{18}

Typical proposed loading levels of actinides in glass will result in an expected alpha–decay level of the order of 10^{18} events/g over the period for which the glass is expected to retain the radioactive waste. This level would be produced by an average atom fraction of actinide atoms in the glass matrix of approximately 3×10^{-5}, resulting in an average volume of glass per decaying actinide atom of about 4×10^{-16} mm^3. For the average alpha–decay we can assume that a particle of atomic mass > 200 and energy of about 80 keV will be created (for examples, see Table 1.2; data is derived from the Nuclear Data Sheets [1973]). Using appropriate longitudinal and transverse straggling values [Winterbon, 1975], an approximate cascade volume will be about 5×10^{-15} mm^3, i.e. considerably larger than the glass volume per actinide atom.

Table 1.2: Examples of actinides which decay by alpha–emission

Isotope	*Half-life*	*Decay Products*	*Recoil Energies*
$^{238}_{94}Pu$	87.74 y	α, $^{234}_{92}U$	5.50 MeV, 89 keV
$^{238}_{92}U$	4.47×10^9 y	α, $^{234}_{90}Th$	4.20 MeV, 68 keV
$^{234}_{92}U$	2.45×10^5 y	α, $^{230}_{90}Th$	4.78 MeV, 78.5 keV

Consequently, over the lifetime of the nuclear waste storage system, damage regions resulting from neighboring actinide decays will overlap many times, resulting in a glass matrix that will have radiation damage over its entire volume, unless the damage produced by one recoil were to fully anneal before another decay event damaged the same volume element. In addition, the MeV α–particle may make a

significant contribution to the damage level as it passes through partially damaged regions. The damage produced by the alpha particles is qualitatively different from that produced by heavier particles, and dependent upon the amount of damage already present. During the heavy-ion (actinide recoil particle) damage buildup, three regions of interest can be identified: (1) the damage produced within an individual collision cascade; (2) the damage resulting when collision cascades overlap; and (3) damage saturation, when further irradiation causes no observable changes. As a first approximation, this is considered to occur when each lattice atom has been displaced at least once.

Heavy ion bombardment represents a valuable method of achieving damage levels within each of the three regions of interest, thereby yielding information potentially useful for determining the long–term stability of glasses containing nuclear wastes. In addition, $^4He^+$ ion bombardment may be used to simulate the effect of the alpha–particles emitted from the decaying actinides.

This thesis contains an attempt at a systematic investigation of ion–bombardment damage effects in single crystals of quartz at low temperature [< 50 K] and, for comparison, some results at room temperature [300 K]. The crystals were implanted with 15 – 200 keV He, Ne, Ar, Kr, Sb, and Bi ions, and analysed with 1 – 2 MeV $^4He^+$ ions, using the Rutherford backscattering/channeling technique.

Appendix I contains a description of the properties of quartz and its polymorphs: the density, structure, bonding, and optical properties of alpha–quartz, beta–quartz, tridymite, cristobalite, silica and metamict SiO_2; and a brief description of some of the electronic properties of α–quartz and silica.

The theories of radiation effects in insulators are discussed in Chapter II. In-

cluded is a basic discussion of the deposition of energy in solids by energetic particles, a discussion of the creation of point defects by elastic collisions and ionization effects, and the effects of these defects on the properties of SiO_2. In addition, several "spike" theories are discussed: thermal spikes, ionization spikes and displacement spikes. Finally, other relevant factors, such as impurities and synergistic effects are mentioned.

In Chapter III the analysis techniques are presented. Rutherford backscattering is introduced, followed by a discussion of channeling. The application of channeling to quartz is detailed, with the appropriate constants given or derived. The special difficulties of channeling analysis in a diatomic, insulating, damaged crystal are discussed.

Chapter IV contains a description of the experimental apparatus and conditions. This includes sample preparation techniques, as well as the ion–bombardment and analysis system.

In Chapter V, the results of Rutherford backscattering/channeling observations and calculations are given. This includes the results of sputtering experiments, observed damage buildup with ion fluence, damage vs depth profiles, damage stoichiometry and dechanneling, both at low temperatures and at room temperature. Also described are the effects of the MeV $^4He^+$ analysis beam. These results are compared with those of other researchers.

Chapter VI contains the interpretation and discussion of the results of Chapter V, based on the theories and data presented in Chapters II and III and Appendices I and II. In Chapter VII the conclusions are summarized.

CHAPTER II: ION BOMBARDMENT EFFECTS ON SOLIDS

2.1 Introduction

An energetic ion incident upon a solid target deposits its energy into ionization and electronic excitation through inelastic collisions, and into atomic displacements through elastic collisions. The energy transfer in individual inelastic collisions is usually small because of the small mass of electrons relative to that of the nuclei; i.e., the electrons carry a small fraction of an ion's kinetic energy because they constitute a small fraction of its mass. For example, the electron of a 1 MeV $^4He^+$ ion carries 0.14 keV as its share of the kinetic energy, all of which could be transferred to a target electron in a head-on collision; if the nucleus of the ion struck a target electron it could transfer a maximum of 0.54 keV of its kinetic energy because of the mass difference.

By contrast, in elastic collisions between nuclei of similar masses the transferred energy can be a large fraction of the incident energy: in the case of identical massses and a head-on (elastic) collision, all of the kinetic energy is transferred. Both the incident particle and the recoiling particle may create further recoils, which may create further recoils, and so on, resulting in a "collision cascade", as shown schematically in figure 2.1.

In the energy regime considered in this thesis, the description of the collision cascade is often simplified by using the following assumptions: (a) the collisions are binary, i.e., each collision involves one moving particle interacting with one stationary particle; (b) the collisions are non-relativistic, and can be described classically, i.e., the particle wavelength $\lambda = \frac{\hbar}{\sqrt{2M_1E}} << p$ (the impact parameter) and (c) the losses of

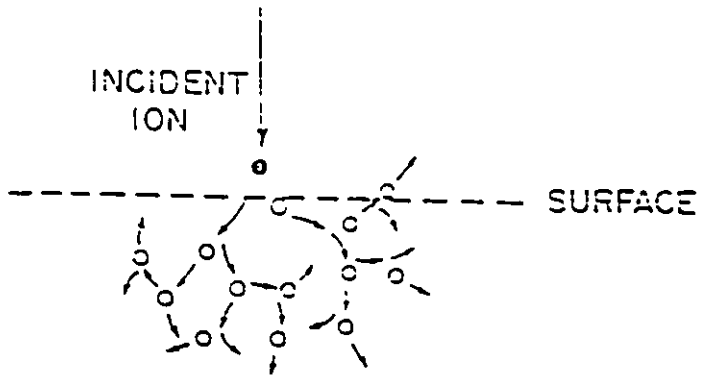

Figure 2.1: Schematic diagram of a collision cascade.

energy through elastic and inelastic collisions can be treated as if they were independent. Winterbon [1976] and Lindhard and Scharff [1961] have shown that assumption (c) is usually reasonable.

The first assumption will break down for the lower energy recoil particles in a cascade, particularly in the case of heavy ion bombardment when the mean distance between displacement collisions is of the order of the mean interatomic spacing. Although this will have a negligible effect upon the spatial distribution of the energy deposited in the cascade, it may strongly influence the response of the target lattice to the bombardment, as in the cases of "thermal spikes" and "displacement spikes", which will be discussed in section 2.3. Futhermore, Biersack [1982, 1987] suggests that, in the case of low-energy charged particles in ionic crystals, the effect of long-range Coulomb forces may significantly enhance the elastic energy deposition rate. As discussed in Appendix I, the bonding in quartz is at least 20%, and possibly as much as 51% ionic.

2.2 The Collision Events

2.2.1 The Elastic Collision

Figure 2.2 shows a typical elastic two–body collision, in both the laboratory frame of reference [2.2 (a)] and the centre–of–mass frame of reference [2.2 (b)]. Using the centre–of–mass frame of reference to simplify the calculations [Goldstein, 1958], the scattering angle θ_{cm} is given by

$$\theta_{cm} = \pi - 2p \int_0^{U_o} \frac{du}{\sqrt{1 - \frac{V(u)}{E'} - p^2u^2}} \qquad 2.01$$

where: p is the impact parameter

$U_o = \frac{1}{p}$

$u = \frac{1}{r}$

r is the distance between the particles

$V(u)$ is the interaction potential

$E' = \frac{EM_2}{M_1+M_2}$ 2.02

E is the incident particle energy (laboratory frame)

M_1 is the mass of the incident particle, and

M_2 is the mass of the struck particle.

The elastic energy transferred, T, is

$$T = T_m \sin^2\left(\frac{\theta_{cm}}{2}\right) \qquad 2.03$$

where: $T_m = \gamma E$, with 2.04

$\gamma = \frac{4M_1M_2}{(M_1+M_2)^2}$. 2.05

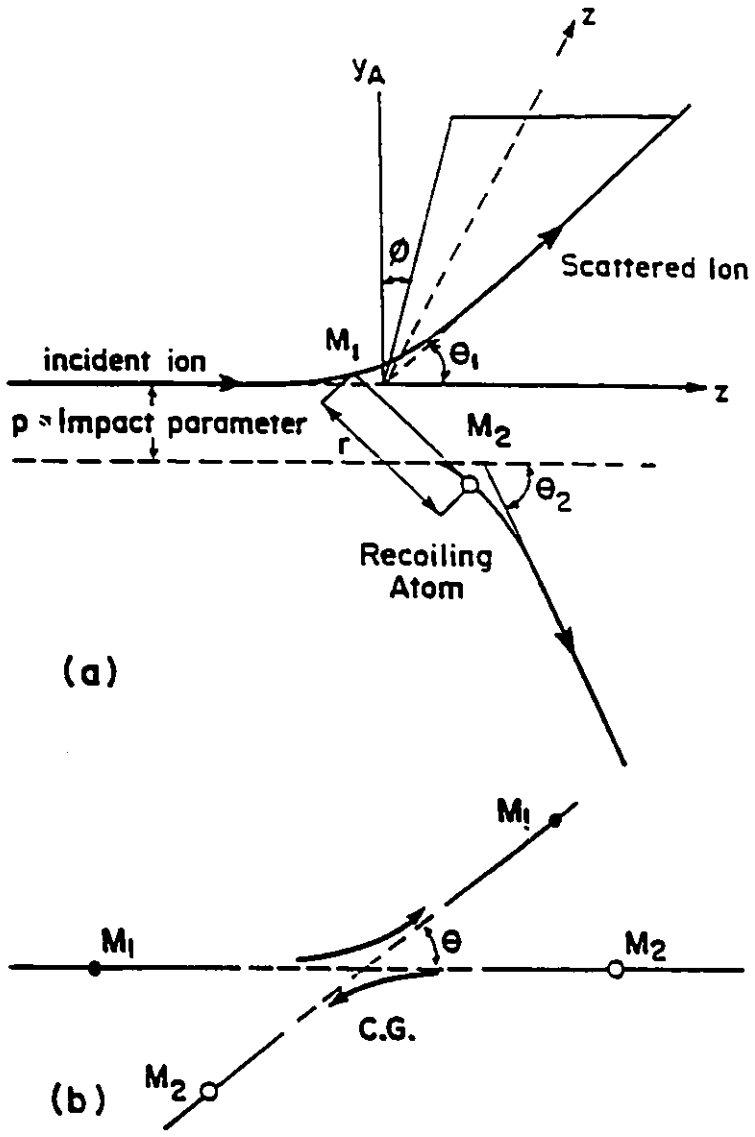

Figure 2.2: Schematic diagram of a binary collision in: a) Laboratory Coordinate System; and b) Centre of Mass Coordinate System

The probability that a particle will be scattered between θ and $\theta + d\theta$ is given by:

$$P(\theta)d\theta = N d\sigma_n(\theta) \qquad 2.06$$

where: $d\sigma_n(\theta)$ is the "differential cross–section" for an elastic collision at angle θ, and can be written as $2\pi p dp$, and

N is the areal density of the target atoms, i.e., $N = \rho\Delta x$. 2.07

ρ is the density of the target (e.g., atoms/mm^3), and

Δx is the thickness of the target (mm).

Any particles striking other particles with an impact parameter between p and $p + dp$ will scatter through an angle between θ and $\theta + d\theta$. Clearly, Δx must be smaller than the ion range for equation 2.06 to be physically meaningful, i.e., $P(\theta)d\theta < 1$. Cross–sections can be calculated in a similar fashion for any collision event.

2.2.2 The Interaction Potential

The force between two atoms is a strong function of the distance between them. For an elastic collision with $r < d$ (where d is the equilibrium lattice spacing in the target), the electrostatic repulsion between two positively charged nuclei dominates the interaction: at larger distances, the electron shells of the particles screen out most of the repulsion; as the separation decreases, the screening effect is reduced until, at very small separations, the potential is a simple Coulombic repulsion between two bare nuclear charges. At distances of the order d, the interaction potential may be attractive due to chemical bonding effects such as the electron exchange interaction in covalent solids, or the Coulombic attraction in ionic solids. At distances of the order of the diameter of the nucleus the potential will be dominated by nuclear forces.

When the impact parameter is in the range of about $1 - 10^{-4}$ nm, the potential is well-described by the Hartree–Foch treatment [Hartree, 1957]. However, the Hartree–Foch potential is very difficult to calculate because of its complexity. The Born–Mayer [1932] potential is an approximation which applies for $r < d$:

$$V(r) = Ae^{-r/B} \qquad 2.08$$

where A and B are constants which can be determined from the elastic moduli of the target. However, it is too weak for $r << d$. The Thomas–Fermi potential [Firsov, 1958] applies well to the interactions between 1 – 2000 keV ions and target atoms. This potential is given as:

$$V(r) = \frac{Z_1 Z_2 e^2}{r} \cdot \phi_{TF}\left(\frac{Z_1}{Z_2}, \frac{r}{a}\right) \qquad 2.09$$

where ϕ_{TF} is a screening function (tabulated by Gombas [1956]) that approaches unity as r goes to zero, and a is the Thomas–Fermi screening distance for an isolated atom, given as:

$$a = 0.8853 a_o Z_2^{-\frac{1}{3}} \qquad 2.10$$

where: $a_o = \frac{\hbar^2}{m_o e^2}$ is the first Bohr radius, 0.053 nm
m_o is the mass of an electron, and
e is the electronic charge.

The scattering angle θ_{cm} is a function of three parameters: $\frac{Z_1}{Z_2}$, $\frac{a}{b}$ and $\frac{p}{a}$,

where: $b = \frac{Z_1 Z_2 e^2}{E}$ is called the collision radius, and
$\epsilon = \frac{a}{b}$ is the reduced (dimensionless) energy,

as defined by Lindhard et al. [1968]. They redefined the screening radius, a, in order to simplify the calculation of the scattering angle. With a now the *effective*

screening radius for a binary collision,

$$a = 0.8853 a_o Z^{-\frac{1}{3}} = 0.8853 a_o \left(Z_1^{\frac{2}{3}} + Z_2^{\frac{2}{3}}\right)^{-\frac{1}{2}} \qquad 2.11$$

the scattering angle, θ_{cm}, is a function only of ϵ and $\frac{p}{a}$. This was then further reduced to give one independent parameter, t:

$$t = \frac{\epsilon^2 T}{T_m} = \epsilon^2 \sin^2\left(\frac{\theta_{cm}}{2}\right) \qquad 2.12$$

with the result that the elastic scattering cross-section could be approximated as:

$$d\sigma_n = \pi a^2 t^{-\frac{3}{2}} f(t^{\frac{1}{2}}) \qquad 2.13$$

The function $f(t^{\frac{1}{2}})$ is a universal screening function, which was approximated by Winterbon et al. [1970] as:

$$f(t^{\frac{1}{2}}) = \lambda t^{\frac{1}{2}} \left[1 + \left(2\lambda t^{\frac{2}{3}}\right)^{\frac{2}{3}}\right]^{-\frac{3}{2}} \qquad 2.14$$

and the parameter, λ, was determined by fitting equation 2.14 to values of $f\left(t^{\frac{1}{2}}\right)$ calculated numerically from the Thomas-Fermi potential.

Lindhard et al. [1968] also produced a simple approximation called the power cross-section:

$$f(t^{\frac{1}{2}}) \approx \lambda_m t^{(\frac{1}{2}-m)} \qquad 2.15$$

The values of m range from 0 – 1. Table 2.1 shows four sets of values commonly used, and the reduced energy ranges to which they apply. Some of these functions are plotted in figure 2.3.

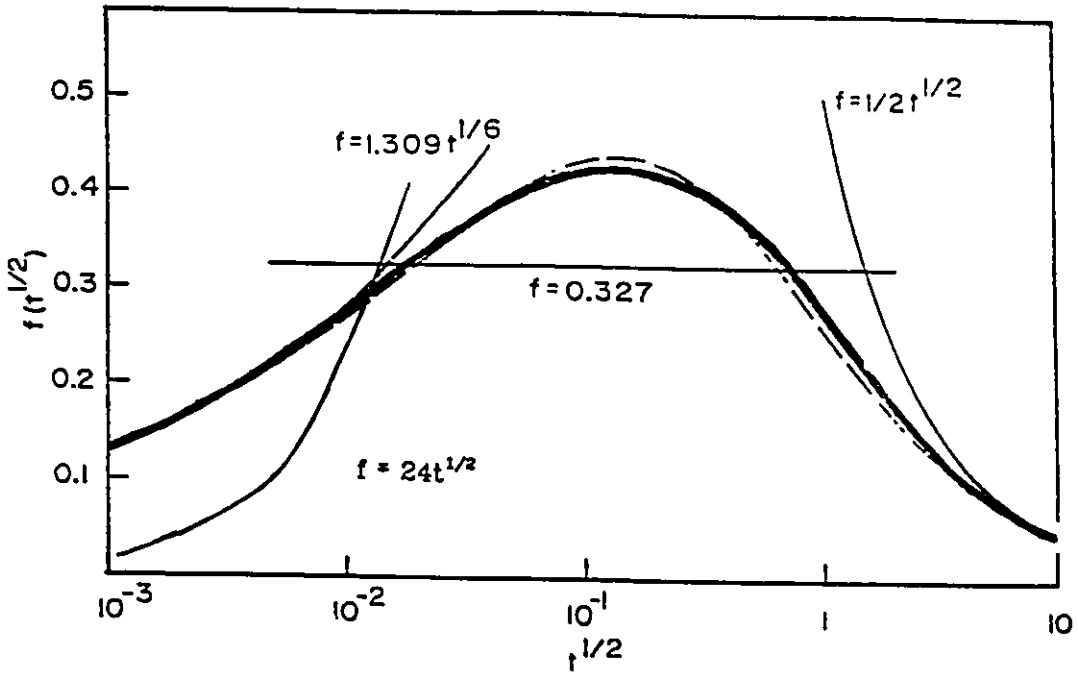

Figure 2.3: The universal screening function, $f(t^{1/2})$:
thick solid line, calculated from the Thomas–Fermi potential;
dashed line, from the numerical approximation, eq. 2.14;
and some power cross–section approximations (see Table 2.1).
Adapted from Winterbon (1970).

Table 2.1: Power Cross–Section Parameters

ϵ	m	λ_m	Type of potential	Screening Function $f(t^{\frac{1}{2}})$
>2	1	0.5	simple Coulomb scattering $V(r) \propto \frac{1}{r}$	$\frac{1}{2t^{\frac{1}{2}}}$
$0.01 < \epsilon < 2$	$\frac{1}{2}$	0.327	$V(r) \propto \frac{1}{r^2}$	0.327
< 0.03	$\frac{1}{3}$	1.309	$V(r) \propto \frac{1}{r^3}$	$1.309t^{\frac{1}{2}}$
<0.001	0	24	Born–Mayer potential	$24t^{\frac{1}{2}}$

2.2.3 Inelastic Energy Loss

Inelastic energy loss is the result of the interactions of moving particles with

electrons of the target atoms. One or more electrons may be knocked out of their potential well (ionization), or electrons may be raised to a higher energy level (excitation). Both events create holes in the quantum–energy structure of the atoms, which results in photon or Auger–electron emission. These emitted particles may themselves produce damage, especially in electrically non–conducting solids such as SiO_2.

2.2.4 Stopping Powers

The elastic (or nuclear) stopping power, $\left(\frac{dE}{dx}\right)_n$ is defined as the rate of energy loss with distance into elastic collisions, i.e.,

$$\left(\frac{dE}{dx}\right)_n = -NS_n(E) = -N\int_0^{T_m} T d\sigma_n \qquad 2.16$$

where $S_n(E)$ is the elastic stopping cross–section and x is the depth of the ion in the target. Applying equation 2.13, one can obtain:

$$\left(\frac{dE}{dx}\right)_n = \frac{-N\pi a^2 T_m}{\epsilon^2}\int_0^{\epsilon} f(t^{\frac{1}{2}})d(t^{\frac{1}{2}}) \qquad 2.17$$

When one substitutes a dimensionless depth parameter,

$$\rho = N\pi a^2 \gamma R \qquad 2.18$$

where R is the depth, or range, of the ion, then a universal elastic stopping cross–section is obtained:

$$s_n(\epsilon) = -\left(\frac{d\epsilon}{d\rho}\right)_n = \frac{1}{\epsilon}\int_0^{\epsilon} f(t^{\frac{1}{2}})d(t^{\frac{1}{2}}) \qquad 2.19$$

The power approximation for $f(t^{\frac{1}{2}})$ gives

$$s_n(\epsilon) = \frac{\lambda_m t^{(1-2m)}}{2(1-m)} \qquad 2.20$$

Then:

$$\text{for } m = 1, \quad s_n(\epsilon) = \frac{\epsilon}{2} ln(1.29\epsilon) \tag{2.21}$$

$$\text{for } m = \frac{1}{2}, \quad s_n(\epsilon) = 0.327 \tag{2.22}$$

$$\text{for } m = \frac{1}{3}, \quad s_n(\epsilon) = 0.981\epsilon^{\frac{1}{3}} \tag{2.23}$$

$$\text{for } m = 0, \quad s_n(\epsilon) = 12\epsilon \tag{2.24}$$

The inelastic (or electronic) stopping power was approximated as

$$s_e(\epsilon) = -\left(\frac{d\epsilon}{d\rho}\right)_e = k\epsilon^{\frac{1}{2}} \tag{2.25}$$

by Lindhard and Scharff [1961]. There is no universal equation for s_e, because k is a function of M_1, M_2, Z_1 and Z_2: figure 2.4 shows $s_n(\epsilon)$ and $s_e(\epsilon)$, for $k = 0.15$ and $k = 1.5$.

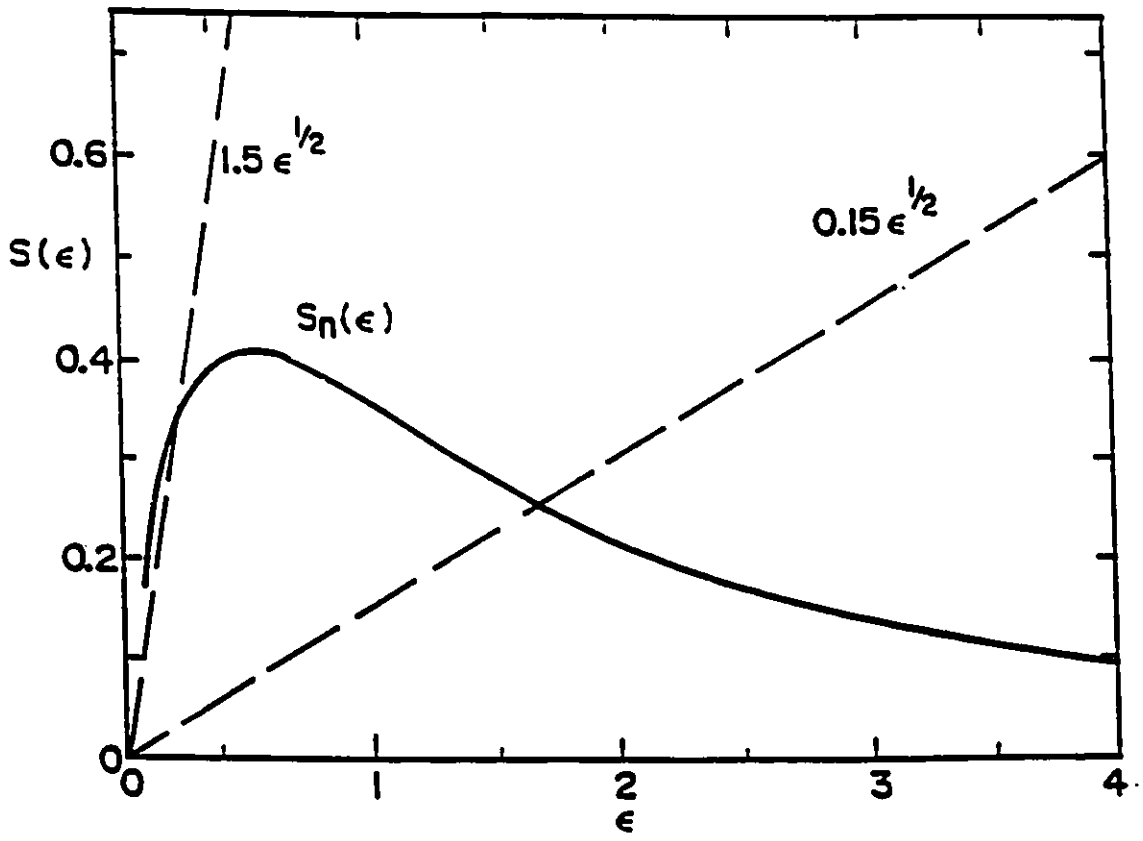

Figure 2.4: Nuclear (elastic) and electronic (inelastic) stopping powers in reduced units: solid line is nuclear and dashed lines are electronic, for k is 0.15 and 1.5; from Walker (1977).

Equation 2.25 and Lindhard and Scharff's [1961] formula for k produce a monotonic dependence of s_e with Z_1, while experimental data shows an oscillatory dependence of s_e with Z_1, due to the electronic shell structure of atoms. The approximation is good to first order, but it can be wrong by as much as a factor of 2 for low velocity ions ($v < \frac{v_0}{2}$) as shown in figure 2.5 from Hvelpund and Fastrup [1968].

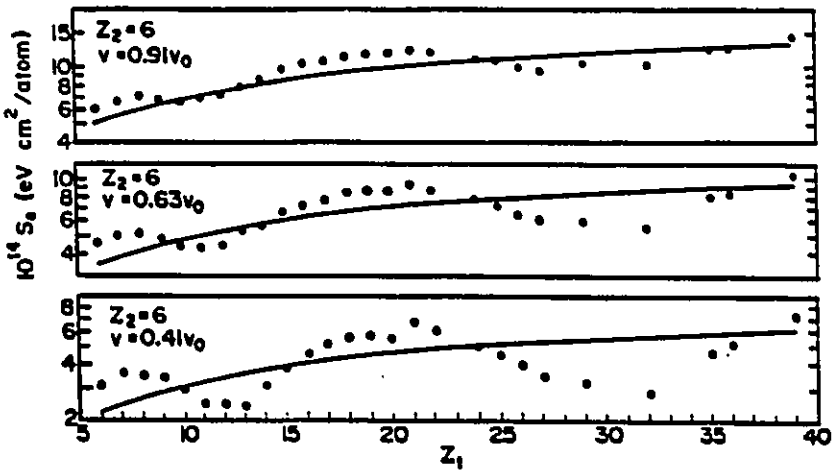

Figure 2.5: Theoretical dependence of electronic stopping power on Z_1, compared to experimentally determined values (Hvelpund and Fastrup, 1968).

Biersack [1987] uses a similar approach:

$$S_e(v) = z_{\text{eff}}^2(v) \cdot S_p(v). \qquad 2.25a$$

Here, the stopping power is the product of the square of the effective charge of the ion at a given velocity, times the stopping power of a proton at that velocity. A formula for z_{eff} was determined by Northcliffe [1960], refined by Brandt and Kitigawa [1982], and further refined by Ziegler et al. [1985] to get S_e to match the experimentally determined values shown in figure 2.5.

If assumption (c) in section 2.1 is correct, then

$$\frac{dE}{dx} = \left(\frac{dE}{dx}\right)_n + \left(\frac{dE}{dx}\right)_e, \text{ and} \tag{2.26}$$

$$E = \nu(E) + \eta(E) \tag{2.27}$$

where $\nu(E)$ is the energy deposited into elastic collisions, and $\eta(E)$ is the energy deposited into inelastic collisions. Since the recoil atoms lose some energy into inelastic collision, whereas almost none of $\eta(E)$ creates recoil atoms, then

$$\nu(E) < \int_{\text{all } x} \left(\frac{dE}{dx}\right)_n dx. \tag{2.28}$$

2.2.5 Range and Energy Deposition Distributions

Winterbon et al. [1970, 1975] have determined approximate range and energy distributions from LSS theory [Lindhard et al., 1963a, 1963b, 1968]. LSS theory assumes a random distribution of atoms in a uniform and infinite solid. It considers three distributions functions: $F_R(\overline{r}, E)$, the ion range distribution, or the final distribution of the implanted ions in the target; $F_N(\overline{r}, E)$, the distribution of energy deposited into elastic (nuclear) collisions; and $F_I(\overline{r}, E)$, the distribution of energy deposited into inelastic (electronic) processes. These functions are, of course, very interdependent.

The spatial moments of these distributions are defined as:

$$\langle r^n \rangle = \int r^n F(\overline{r}, E) d^3\overline{r} \tag{2.29}$$

At $n = 0$, equation 2.29 gives the normalization factors: $\int F_R(\overline{r}, E) d^3\overline{r} = 1$. because the ion must stop somewhere in the infinite solid; $\int F_N(\overline{r}, E) d^3\overline{r} = \nu(E)$: and $\int F_I(\overline{r}, E) d^3\overline{r} = \eta(E)$.

Given assumptions (a), (b) and (c) in section 2.1, $F(\overline{r}, E)$ can be described by a linear Boltzmann transport equation:

$$F(\overline{r}, E) = N\delta\overline{r} \int d\sigma_{N,I} \Big[F(\overline{r} - \delta\overline{r}, E - T_N - \sum_i T_{Ii}) + F(\overline{r} - \delta\overline{r}, T_N - E_d) + \sum_i F_e(\overline{r} - \delta\overline{r}, T_{Ii} - V_i) \Big] + (1 - Nd\overline{r} \int d\sigma_{N,I}) F(\overline{r} - \delta\overline{r}, E) \qquad 2.30$$

in the case of $Z_1 = Z_2$,

where: $N(\delta\overline{r})d\sigma_{N,I}$ is the probability that an elastic or inelastic collision occurs within $\overline{r}$ to $\overline{r} + \delta\overline{r}$,

T_N is the energy transferred to an elastic recoil,

T_{Ii} is the energy transferred to the i^{th} electron,

E_d is the energy required to displace a recoil atom from its lattice site,

V_i is the ionization energy of the i^{th} electron,

F_e the spatial distribution function for the electrons.

As it stands now, this equation cannot be solved exactly. However, by multiplying both sides of equation 2.30 by r^n and integrating by parts, the moments can be determined exactly (see Lindhard et al. [1963a], and Winterbon et al. [1970]).

Winterbon [1975] has tabulated the first four longitudinal moments and the second transverse moment for all three distributions, for various ion–target–energy combinations, from which the moments for other energies and mass ratios can be interpolated. When these moments are applied to the Edgeworth expansion [Baroody, 1965], one obtains a fairly good approximation of the actual distributions. The Edgeworth expansion is a weighted–Gaussian function, used because it is relatively simple to calculate and because ion range and energy distributions are often similar to a Gaussian distribution. For the first four moments, the Edgeworth series expansion of the longitudinal distributions is:

$$F(z, E) = \frac{gf(\xi)}{\sqrt{2\pi\mu_2}} e^{-\xi^2/2} \qquad 2.31$$

where: z is the longitudinal distance (depth),

g is the 0^{th} moment described in equation 2.29. i.e.,

$g_R = 1$ is the range normalization factor,

$g_N = \nu(E)$ is the elastic energy deposition normalization factor, and

$g_I = \eta(E)$ is the elastic energy deposition normalization factor;

the Edgeworth moments, for $n = 1$ to 4, are:

$$\mu_n = \langle (z - \langle z \rangle)^n \rangle, \qquad 2.32$$

$$\xi = \frac{(z - \langle z \rangle)}{\sqrt{\mu_2}}, \qquad 2.33$$

and

$$f(\xi) = 1 - \left(\frac{\mu_3}{6\mu_2^{3/2}}\right) \cdot (3\xi - \xi^3) + \frac{1}{24}\left(\frac{\mu_4}{\mu_2^2} - 3\right) \cdot (3 - 6\xi^2 + \xi^4) - \left(\frac{\mu_3^2}{72\mu_2^3}\right) \cdot (15 - 45\xi^2 + 15\xi^4 - \xi^6) \qquad 2.33a$$

The results of these calculations are depth profiles such as those shown in figure 2.6. Of particular interest are the values of: $f_D(0)$, the rate of elastic energy deposition at the surface, which is a critical number for sputtering calculations (see section 2.2.8); and f_D^{max}, the peak of the elastic energy deposition profile.

These distributions describe what is effectively the average of an infinite number of individual ion range and energy distributions. They may differ significantly from actual individual ion tracks, i.e., the path of an individual ion or its deposited energy distribution. Walker [1977] has compared Edgeworth distributions (using moments from Winterbon[1975]) to Monte–Carlo calculations of individual ion cascades (displaced atom distributions) in Si and Ge, and determined approximate values of R_v, the average ratio between the volumes of individual ion cascades and those of statistical cascades (from the LSS and Edgeworth calculations). Figure 2.7 [Walker, 1977] shows three examples of Monte Carlo calculations of ion cascades in Si, with statistical cascade dimensions sketched around them at the points where the energy

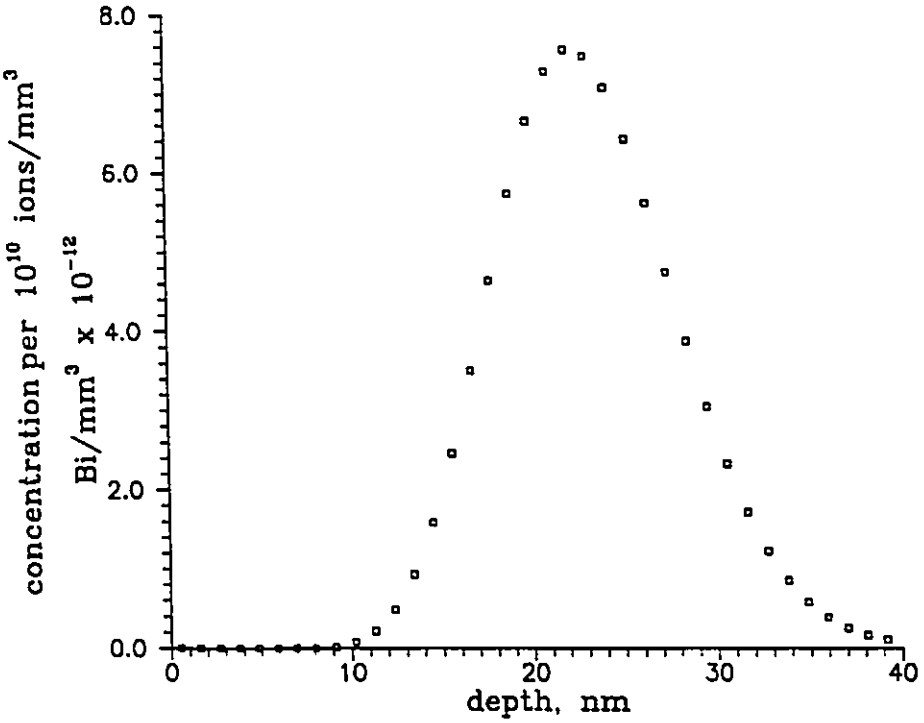

Figure 2.6(a): Range distribution of 60 keV Bi^+ ions in quartz, calculated from Edgeworth moments determined by interpolation from the Winterbon (1975) tables.

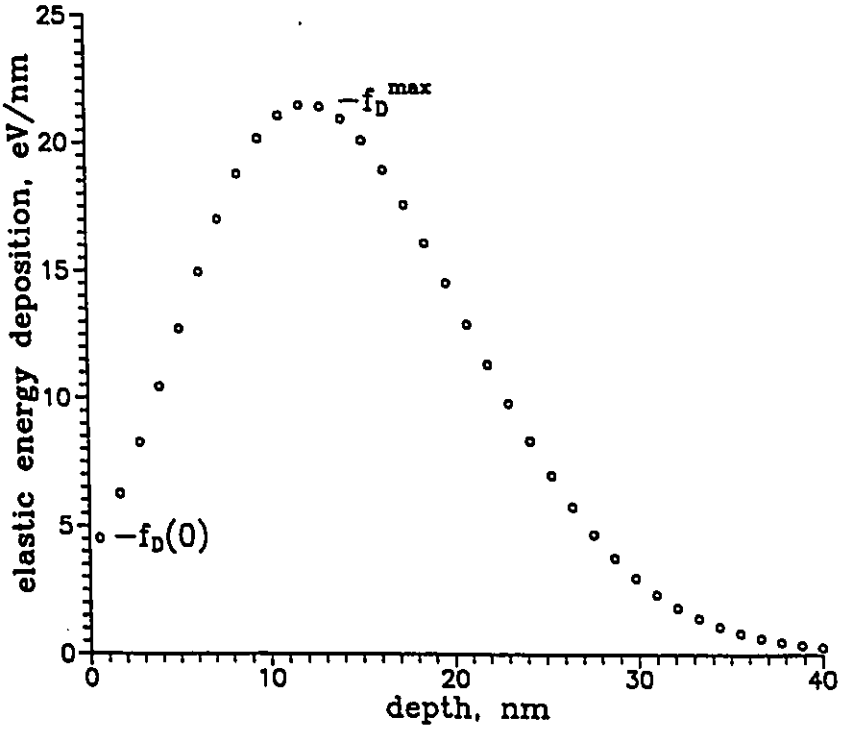

Figure 2.6(b): Depth profile of 60 keV Bi^+ elastic energy deposition in quartz, calculated from Edgeworth moments determined by interpolation of the Winterbon (1975) tables.

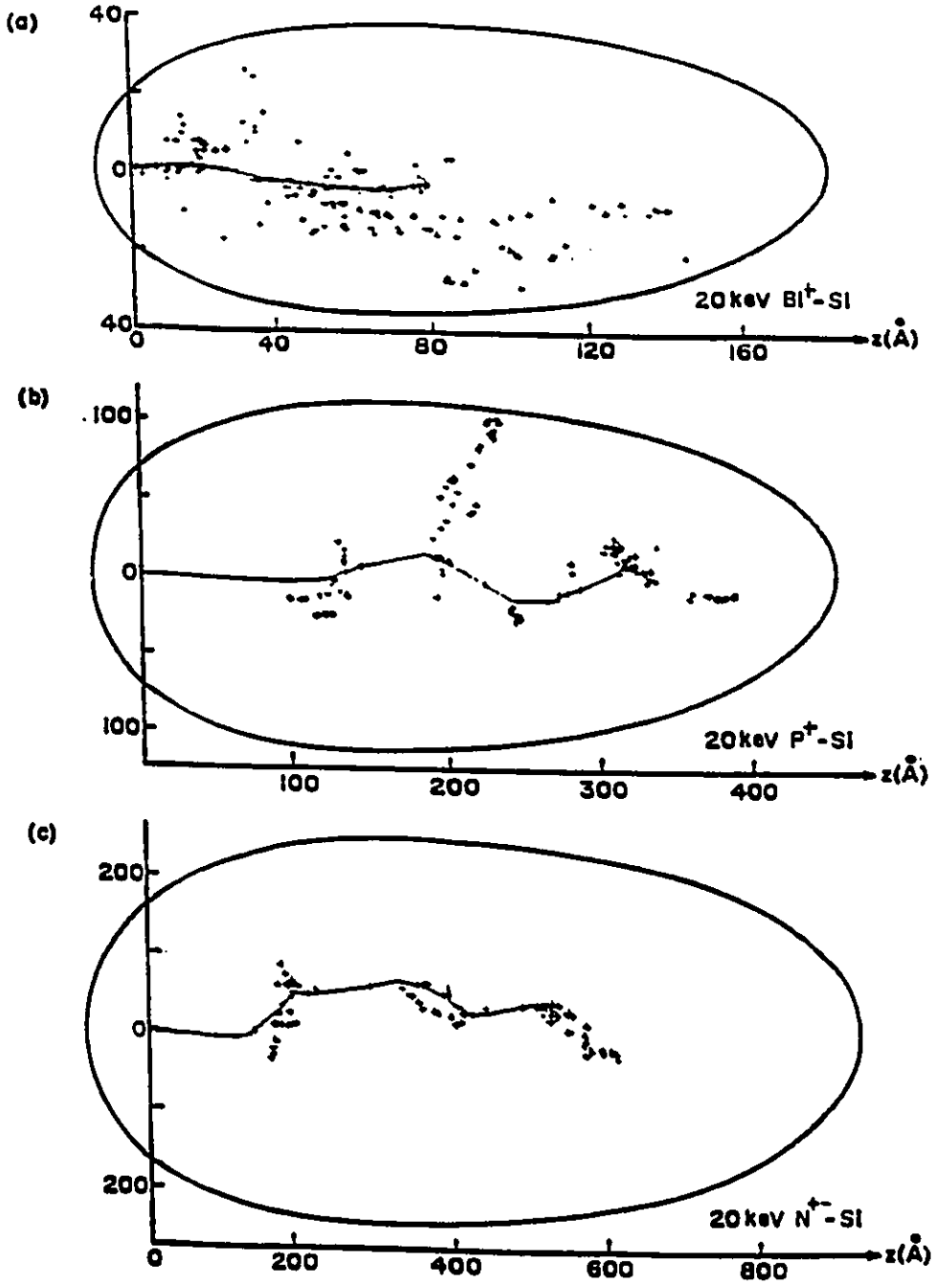

Figure 2.7: A comparison of individual and statistical cascade dimensions for three mass ratios; the statistical cascade dimensions (solid curve) are the contours containing the region with greater than one-tenth of the maximum rate of nuclear energy deposition. Displaced atoms are indicated by a + sign. The ions' trajectory and final location are also shown; from Walker (1977).

deposition into elastic collisions is about one tenth the maximum. Figure 2.8 [Walker. 1977] shows the one-dimensional cascade ratio, $\delta = R_v^{\frac{1}{3}}$, as a function of mass ratio, $\frac{M_2}{M_1}$, as calculated for various ions incident upon Si and Ge. Walker [1977] has shown that δ is independent of energy for $M_2 < M_1$ in the range 10 – 100 keV. Also shown is a theoretical curve from Sigmund et al. [1968].

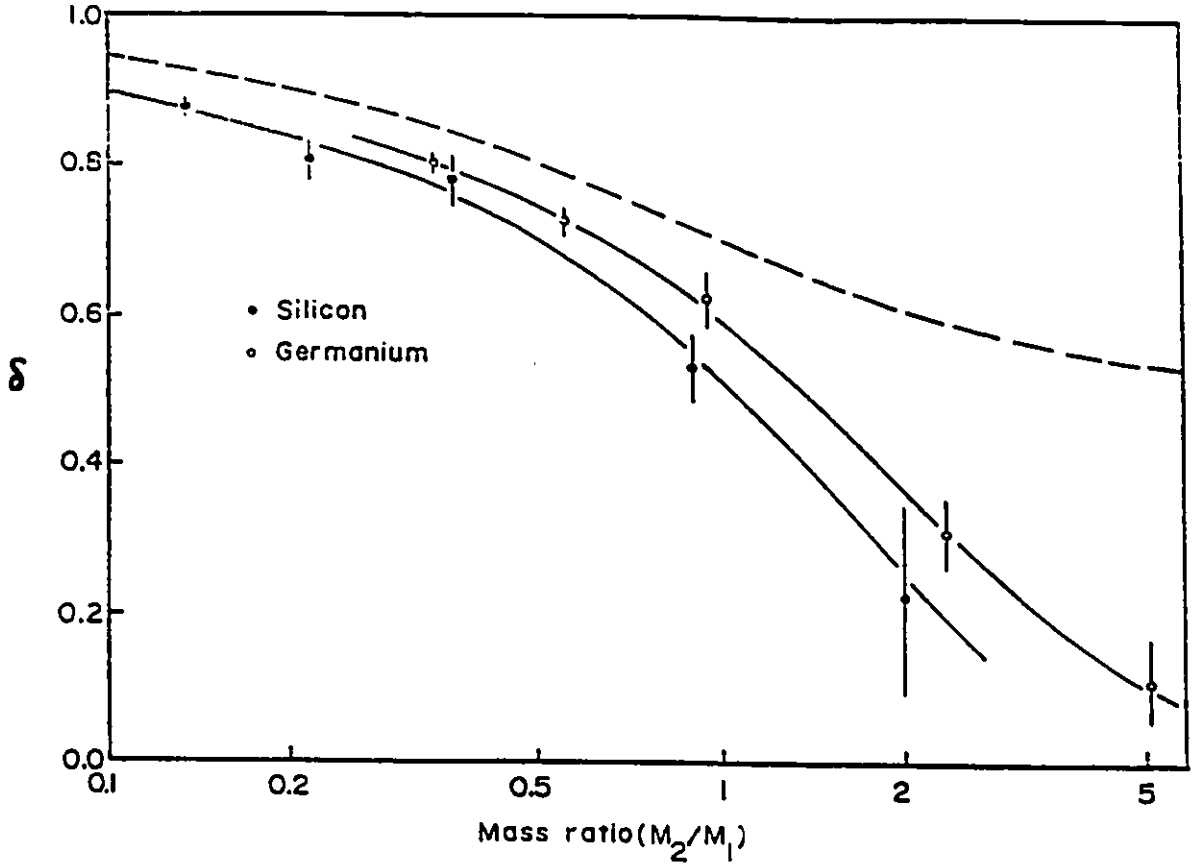

Figure 2.8: The one-dimensional cascade ratio, δ, as a function of mass ratio. The dashed line is from Sigmund (1968) and the points are Monte Carlo results from Walker (1977).

These figures indicate that the energy deposited into elastic collisions, which generally determines the damage distribution, is deposited within a smaller volume

than the statistical cascade dimensions would imply. Walker [1977] calculated the average energy density, $\bar{\theta}_\nu$, within the volume

$$V = \frac{4}{3}\pi(\Delta x^2)_D^{\frac{1}{2}}\langle y^2\rangle_D. \tag{2.34}$$

Here, $(\Delta x^2)_D^{\frac{1}{2}}$ is the mean longitudinal straggling of the damage profile, and $\langle y^2\rangle_D^{\frac{1}{2}}$ is the mean lateral straggling. Then V is the volume within one standard deviation of the centre of the statistical cascade. The average energy density is

$$\bar{\theta}_\nu \approx \frac{0.2\nu(E)E}{N_v} \tag{2.35}$$

where N_v is the number of atoms within V. The effective *individual* cascade volume is actually $N_v \cdot R_v$, so the average deposited elastic energy density becomes

$$\bar{\theta}_\nu \approx \frac{0.2\nu(E)E}{N_v R_v}. \tag{2.36}$$

$\bar{\theta}_\nu$ and the actual energy deposition density profile are important when calculating thermal spike and displacement spike effects, as in section 2.3.

2.2.6 Simple Elastic–Collision Defect Creation

Kinchin and Pease [1955] developed a simple model to calculate the number of atoms displaced by an ion of energy E, assuming that the loss of energy to inelastic events is negligible, and that the atoms are hard spheres. They set up an equation similar to equation 2.30:

$$\int_0^E \frac{d\sigma_n}{dT}\left[N(E) - N(E-T) - N(T)\right]dT = 0 \tag{2.37}$$

where $N(E)$ is the number of Frenkel pairs (vacancy–interstitial pairs) created by a primary recoil atom, and T is the energy of the primary recoil atom. They defined the following boundary conditions:

$$N(E) = 0 \text{ if } E < E_d \tag{2.38}$$

$$N(E) = 1 \text{ if } E_d \leq E \leq 2E_d \qquad 2.39$$

and determined that

$$N_{KP}(E) \approx \frac{E}{2E_d} \qquad 2.40$$

Sigmund [1969a] showed that, for $E >> E_d$, a more exact solution is:

$$N_{KP}(E) \approx \frac{0.42\nu(E)}{E_d} \qquad 2.41$$

This frequently used equation is called the "modified Kinchin–Pease" equation. It assumes that the inelastic energy deposition has little effect on the number of displaced atoms, except by reducing the total amount of energy available for elastic collisions.

In obtaining the calculated values for the number of displaced atoms/ion it is necessary to know the displacement energy, E_d. Hobbs et al. [1980] used 5 eV as the Si–O bond energy; this leads to a minimum displacement energy for oxygen of 10 eV, since two bonds need to be broken, and 20 eV for silicon, since four bonds need to be broken. Das and Mitchell [1974] observed a threshold energy of approximately 50 keV for electron-bombardment-induced damage creation in quartz. They calculated the maximum energy which could be transferred from an electron to an atom of silicon or oxygen, using equations 2.04 and 2.05, and obtained values of 5.4 eV for $E_d(Si)$ and 9.5 eV for $E_d(O)$. Das and Mitchell implied that these displacement energies are both appropriate, but they stated no reason to believe that the damage which they observed could not be due to displacements of only one kind of atom, Si or O. By comparison with the results of Hobbs et al. [1980] it seems reasonable to assume that the damage at the threshold was displaced oxygen atoms: the values of 10 eV and 9.5 eV are in good agreement. It seems reasonable that the silicon atoms would be more strongly bonded than the oxygen atoms, and therefore Hobbs et al.'s value of

$E_d(Si)$ = 20 eV is used in the following calculations. (Note: there would appear to be an error somewhere in Das and Mitchell's calculations, or a misprint in their paper. When using $E_{threshold}$ = 50 keV, equations 2.04 and 2.05 result in values of $E_d(O)$ = 6.8 eV and $E_d(Si)$ = 3.9 eV.)

Another approach, proposed by M.T. Robinson [1969], is to calculate E_D, the energy deposited by an ion with energy E into elastic collisions per atom·mm^{-2} of the target:

$$E_D = \int_0^{T_m} \frac{d\sigma_n}{dT} \nu(T) dT \qquad 2.42$$

where, as before, $T_m = \gamma E$. This is generally applied to high energy ions ($\epsilon > 100$) which have a relatively low probability of transferring $T >> E_d$. What is needed is an approximation of the values of $\nu(T)$ of the recoil atoms. Robinson used

$$\frac{d\sigma}{dT} = 6.495 \times 10^{-14} \cdot \frac{(Z_1 Z_2)^2}{E} \cdot \frac{(M_1/M_2)}{T^2} \qquad 2.43$$

(given for units of mm^2·eV) from Sigmund [1969b], where

$$\nu(\epsilon) = \frac{\epsilon}{1 + k_L g(\epsilon)}, \qquad 2.44$$

ϵ is the reduced energy of the recoils,

$$\epsilon = \frac{T}{E_L}, \qquad 2.45$$

$$E_L = 86.931 Z_2^{\frac{7}{3}}, \qquad 2.46$$

$$k_L = 0.133745 Z_2^{\frac{2}{3}} M_2^{\frac{1}{2}}, \qquad 2.47$$

$$and\ g(\epsilon) = 3.4008\epsilon^{\frac{1}{3}} + 0.40244\epsilon^{\frac{2}{3}} + \epsilon. \qquad 2.48$$

Equation 2.44 assumes the atoms of the target are all the same, so applying this equation to a compound such as SiO_2 will introduce some uncertainty in the results.

For 2 MeV $^4He^+$ incident on quartz. equation 2.42 becomes

$$E_D = 2.66 \times 10^{-17} \int_0^{1.08\text{MeV}} \frac{\nu(T)}{T^2} dT \text{ mm}^2\text{eV} \qquad 2.49$$

where:

$$\nu(T) = \frac{\epsilon}{1 + 0.134(3.4\epsilon^{\frac{1}{3}} + 0.402\epsilon^{\frac{3}{4}} + \epsilon)} \qquad 2.50$$

This was integrated numerically to obtain $E_D \approx 1.8 \times 10^{-15}$ eV· mm^2/atom, which can then be converted into an equivalent of $\nu(E)$ by multiplying by the areal density of atoms of quartz in the surface region where the $^4He^+$ ions are creating damage. Then the cross–section for creating elastic displacements with a 2 MeV $^4He^+$ ion is $\sigma_{\text{He}} \approx \frac{0.42E_D}{E_d} \approx 5.7 \times 10^{-17}\text{mm}^2$. Then, if the number of atoms of SiO_2 in the region of interest is $N = 4 \times 10^{14}$ atoms/mm^2 (the size of the RBS/channeling surface peak of an aligned, undamaged quartz crystal), the number of displaced atoms is $N \cdot \sigma_{\text{He}} \approx 0.017$ atoms/ion: an average of about 1 in 60 ions would create an elastic displacement. Here, E_d is taken as $\approx$ 10 eV for oxygen and $\approx$ 20 eV for silicon, as derived above.

Another approach is that of Kool et al. [1976, 1978] and Wiggers et al. [1979] who calculated that the cross–section for creating a Frenkel pair by elastic collisions is approximately

$$\sigma_F \approx \frac{200\pi a^2 M_1 {Z_1}^2 {Z_2}^2 E_R^2}{M_2 E E_d} ln\left(\frac{E}{E_d}\right) \qquad 2.51$$

where E_R is the Rydberg energy, 13.606 eV. For the above example, this would result in a cross–section of $\sigma_F \approx 1.1 \times 10^{-16}\text{mm}^2$, in fairly good agreement with the previous calculation.

Burnett and Page [1986] plotted the ionicity versus G, the experimentally measured total ion fluence required to amorphise a crystal multiplied by the ion

energy. If the ionicity of bonding in quartz is 20%, this approach predicts that one requires 15 – 32 eV/atom to amorphise quartz; if the ionicity is 51%, then it predicts a requirement of 1.2 – 1.4 keV/atom. The breadth of this range may be due to the differences in the definition of amorphous in measurements of damage in covalent semiconductors and ionic ceramic oxides.

2.2.7 Simple Ionization–Induced Defect Creation

When an electron is ejected from an atom in a solid, many things can happen. If the electron is part of a bond, the bond will break; in the open structure of quartz, this often leads to relaxation of several atoms, preventing the bond from forming again. If it is an inner–shell electron, an instability is created, resulting in a higher level electron eventually dropping into the position vacated by the ejected electron, accompanied by the emission of either: (a) a photon with energy corresponding to the difference in energy between the two levels; or (b) another outer electron with the energy difference as kinetic energy. This latter process is called Auger–electron emission. The emitted electron is the more probable process for low–Z atoms such as silicon and oxygen. Both processes will result in ionization and/or excitation elsewhere in the solid; both processes can repeat until all of the missing electrons are in the valence (binding) shell.

If the local ionization density is large, there may be enough ionization for an "intrinsic photolysis process" [Tanimura et al., 1983, 1984] to occur. In this process ionization creates a very close vacancy/interstitial pair, usually with oxygen atoms. The presence of local strain or damage may stabilize these otherwise short–lived defects. Tanimura et al. show that the optical effects attributed to these defects decay after about 1 ms at temperatures of less than 150 K, and after only 0.01 ms

at temperatures of > 220 K. This rapid decay is in a crystal which is otherwise undamaged, where the optical defects are quite well separated. The ejected electrons usually bond to an oxygen atom when they come to rest, resulting in a charged defect.

2.2.8 Sputtering

When energetic ions bombard a material, atoms within the first few monolayers of the surface may be ejected: this is called sputtering. The sputtering yield S depends upon the binding energies of the target atoms and the energy deposited into elastic collisions at the surface. This surface–deposited energy depends upon the ion energy, the atomic masses and numbers of both the ion and the target atoms, as previously described in section 2.2.5. The values may be obtained from equation 2.31, using the depth $z = 0$. Sigmund [1969c] developed a model for sputtering of elemental targets, assuming a planar surface, which fits the available experimental data quite well, as long as the deposited energy density at the surface is less than approximately 10 eV·nm²/atom [Thompson. 1981]. Sigmund's [1969c] model gives the sputtering yield as

$$S = \frac{\Delta x f_D(0)}{\pi^2 U_o} \qquad 2.52$$

where: U_o is the surface binding energy per atom,
$f_D(0)$ is the energy deposited into elastic collisions at the surface (depth = 0),
Δx is the depth over which the deposited energy contributes to sputtering.

Sigmund [1969c] uses

$$\Delta x \approx \frac{3}{4NC_o} \qquad 2.53$$

which is approximately the range of an average recoiling atom, i.e., about 0.5 - 1.0

nm. Here, N is the number density of atoms in the target, and C_o is a constant which Sigmund used for a low energy collision cross-section approximation.

If the target is a compound, complications may arise due to: (a) the different masses of the target atoms, which affect the collision cross-sections, the recoil ranges, and the energy transferred in collisions; and (b) different surface binding energies. There are many theories describing preferential sputtering of one constituent of a binary compound [Kelly and Lam, 1973; Kelly, 1978; Haff, 1977; Shimizu et al., 1973; Pickering, 1976; Collins, 1978; Webb et al., 1978]. Effect (a) tends to cause preferential sputtering of the lighter atoms, but is small except for very large mass differences ($\frac{M_A}{M_B} > 2$) [Kelly, 1978].

In the case of quartz, $\Delta x \approx 1$ nm, and $U_o \approx 5$ eV for oxygen (Kelly and Lam [1973] quote 5 eV $\pm$ 1 eV) and 10 eV for silicon. Since there are twice as many oxygen atoms as silicon atoms present, as a first rough approximation, one expects the ratio of the sputtering yields to be

$$\frac{S_O}{S_{Si}} \approx 2\left(\frac{10eV}{5eV}\right) \approx 4$$

[Kelly, 1978]. The magnitude of the sputtering yield is then predicted, using equation 2.52, to be approximately

$$S_{tot} = S_O + S_{Si} = \frac{1}{\pi^2} f_D(0)\left[\frac{1}{3}U_o(Si) + \frac{2}{3}U_o(O)\right] \text{ at/ion} \qquad 2.54$$

For $f_D(0) \approx 450$ eV/nm (i.e. the surface elastic energy deposition rate for 60 keV Bi^+ ions in quartz, obtained by interpolation of the data in Winterbon's [1975] tables: see figure 2.3), S_{tot} becomes 7.5 at/ion.

Again, this assumes a perfect surface (no defects or impurities) and no significant contribution due to inelastic energy deposition. In a real quartz crystal under

ion–bombardment, there are dangling bonds, electronic sputtering by ionization of the last bond of a surface atom and as much as 10% water impurities (see Appendix I), further lowering the average bonding, thereby increasing the sputtering yield.

In quartz, the ionization–sputtering process would predominately affect surface oxygen atoms: many of these atoms, held by two bonds, could have a bond ionized, leaving them held by only one bond; because of the open structure of quartz considerable relaxation would often occur before the broken bond could reform. Then, upon being ionized again, they would be sputtered. The "intrinsic photolysis process" of Tanimura et al. [1983, 1984] appears to be the same thing as the above process. The very close vacancy/interstitial pairs created are very short–lived in the bulk of the crystal ($10^{-3}s$ at $T \leq 150K$; $10^{-5}s$ above $220K$), but at the surface might often result in the loss (electronic sputtering) of the oxygen atom.

Kelly and Lam [1973] and Kelly [1978, 1987] suggest that there may be a significant thermal sputtering component for some ion–oxide combinations, but that this does not seem to be important unless: (a) the target is at a temperature very near to its melting point; or (b) a very high density deposition of energy creates a "thermal spike" which raises the temperature to about the melting point, near the surface. Then:

$$S_{\text{thermal}} \approx \frac{p\pi\langle\Delta y^2\rangle\tau_s}{\sqrt{2\pi mkT}} \qquad 2.55$$

where: p is the equilibrium vapour pressure
m is the mass of the target atom
k is Boltzmann's constant
T is the maximum "temperature" of the thermal spike, near the surface
$\langle\Delta y^2\rangle^{\frac{1}{2}}$ is the lateral radius of the spike near the surface

τ_s is the length of time the spike region is "hot".

The values for T and τ_s will be determined in section 2.3.3.

2.3 Spike Theories

When an incident ion deposits energy at a high rate, assumption (a) in section 2.1 breaks down: the collisions are no longer binary. This may result in the damage and sputtering being enhanced by "spike" processes [Thompson, 1981]. There are three main categories of "spike" processes: the displacement spike, the ionization spike and the thermal spike.

2.3.1 Displacement Spikes

Brinkman [1954, 1956] proposed a model in which an incident ion of low enough energy ($\epsilon < 0.1$) displaces one or more atoms in every plane of the target through which it passes, creating a trail of vacancy–rich material surrounded by a "halo" of interstitial atoms. The effective displacement energy, $(E_d)_{\text{eff}}$, is reduced by the fact that atoms are displaced simultaneously or nearly simultaneously with other atoms to which they were bonded. The result of this is that more atoms are displaced, and the local damage density is quite large. Figure 2.9 is a schematic diagram of a displacement spike, taken from Monnin [1973].

2.3.2 Ionization Spikes

When high energy ions strike an insulating target, large numbers of electrons may be driven away from the ion path, creating a track which contains a high density of positive ions [Fleischer et al., 1965, 1968]. These ions repel each other, and, if

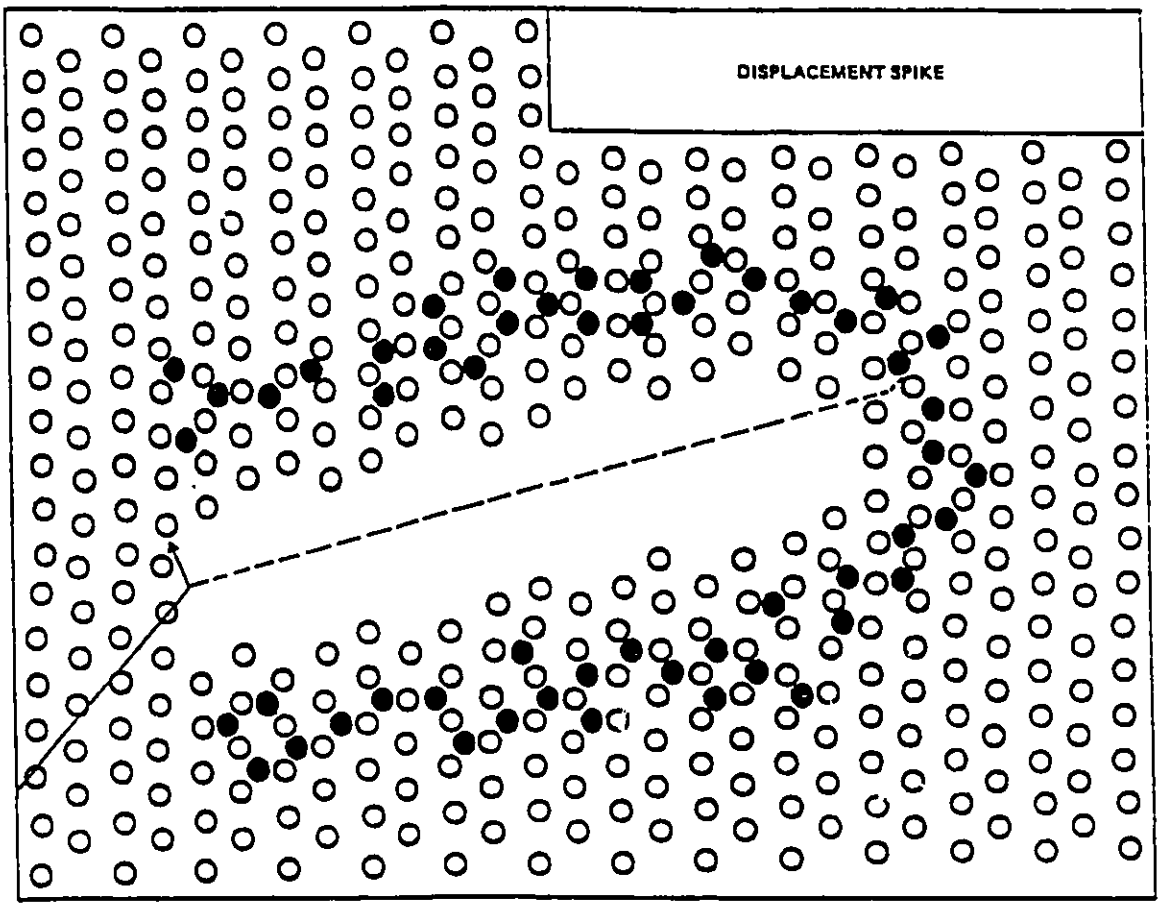

Figure 2.9: Schematic diagram of a displacement spike.

the force is great enough (i.e. if the charge density is large enough) and the time for the electrons to diffuse back to the positive ions is greater than the time required to create an interstitial ($\approx 10^{-13}s$), then many interstitials are created by ions pushing away from the track. The track then becomes a vacancy-rich region surrounded by a "halo" of interstitials, similar to the displacement spike. Another name for this is a

"Coulomb explosion". Figure 2.10 is a schematic diagram of an ionization spike, taken from Monnin [1973]. Monnin concludes that the ionization spike is responsible for the fission fragment tracks observed in many inorganic insulators such as quartz and mica, by creating a damaged region which etches much faster than the surrounding material. Monnin [1973] suggests that the criteria for such a spike is an ion velocity $v > \frac{Z_1 e^2}{\hbar}$, or an electronic energy loss of 10^4 eV/nm.

Fleischer et al. [1965] called the ionization spike "in essence a multiple Varley process." The Varley process describes the creation of Frenkel pairs in an ionic or partially ionic material by electronic energy deposition [Varley, 1954a.b; Howard et al., 1959, 1961; Dexter, 1960; Williams, 1962]. It is possible that the "intrinsic photolysis" observed by Tanimura et al. [1983, 1984] is the Varley effect in quartz. They found that most of the defects created decayed after 0.9 ms at $T < 170$ K, and decayed faster at higher temperatures. By comparing the temperature dependence of the decay time to that of various optical defects, they were able to identify the most prominent defect as an E_1' centre, which is a charged oxygen Frenkel pair [Feigl et al., 1974]. They observed a very high efficiency for defect creation: $(E_d)_{\text{eff}} \approx 50 \pm 30$ eV, comparable to the elastic displacement energy. The short lifetime of the defect indicates that very close vacancy–interstitial pairs are created.

The "intrinsic photolysis" seen by Tanimura et al. [1983, 1984] was caused by 2 MeV electrons, with an ionization energy deposition rate of 10^{-3} eV/nm, so the photolysis defects created are very isolated, approximately one every 50 μm. In contrast, a 1 keV electron (typical energy of an Auger electron) deposits about 50 eV/nm in quartz, or one photolysis defect every other atomic layer, given the same process. A 2 MeV $^4He^+$ ion deposits ionization energy at approximately 400 eV/nm or several photolysis defects in every atomic layer. The peak of a 60 keV Bi^+ elastic

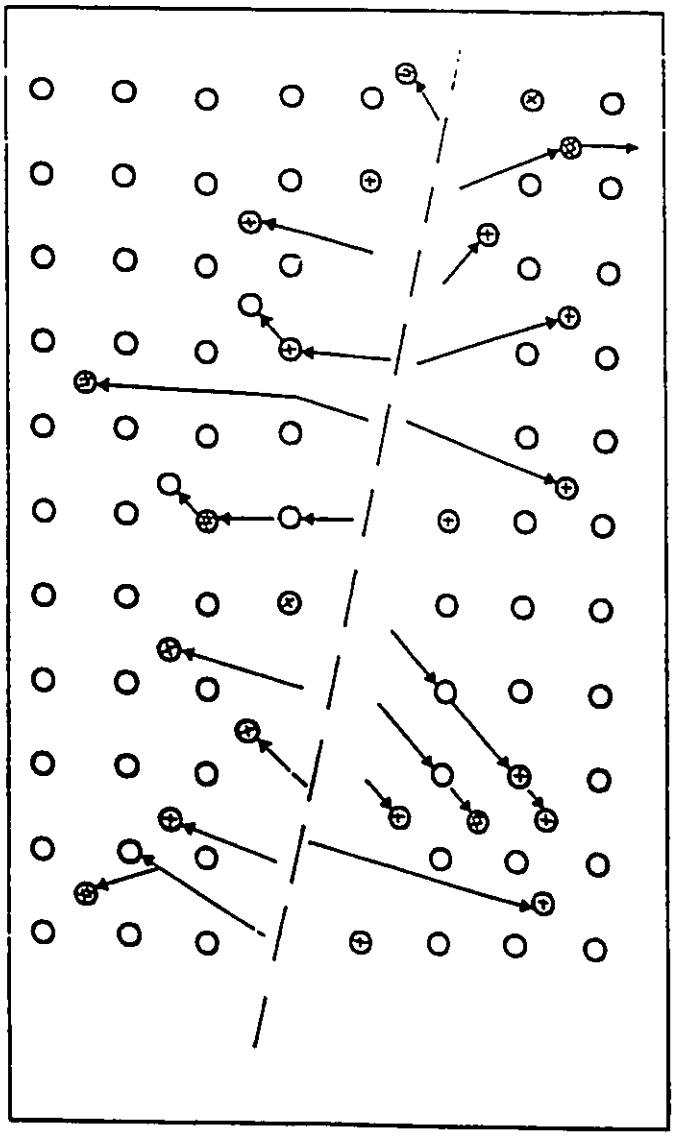

Figure 2.10: Schematic diagram of an ionization spike.

energy deposition profile, as calculated using the data of Winterbon [1975], is even greater, about 1 keV/nm. There is, then, a fair probability for an Auger electron to create photolysis defects close enough to each other that the strain field of one would

stabilize the other. For a 2 MeV $^4He^+$ or a 60 keV Bi^+ ion, a large fraction of the defects might stabilize, especially in the presence of previously created damage, or strain due to impurities.

Arnold and Mazzoldi [1987] take a similar approach, showing several ways in which close oxygen vacancy/interstitial pairs could be stabilised: by peroxy bond formation, by hydroxy bomd formation in the presence of hydrogen or water impurities, or by Si–Si bond formation. They quote work by Griscom [1984, 1985] and Freibele et al. [1979].

Townsend [1990] observes that ionisation by MeV $^4He^+$ ions creates colour centres and other defects, but at a rate which is low compared to the elastic damage at the end of the ion range. He notes that the presence of elastic damage enhances the ionisation damage rate.

Jollet et al. [1990] state that for energetic ions (> 1 MeV/amu) damage is primarily by ionisation. Toulemonde et al. [1990] agree, and show that the ionisation damage efficiency increases with ionisation density, by as much as a factor of 10^4, although, for reasons not clear from their paper, they state that 1 MeV $^4He^+$ is an exception.

Griscom et al. [1990] and Devine [1990] show that ionisation damage in silica is enhanced by the presence of OH impurity. Devine states that the presence of strained Si–O–Si bonds can increase ionisation damage efficiency by several orders of magnitude.

2.3.3 Thermal Spikes

Both the elastically and inelastically deposited energy in a cascade eventually become dissipated as atomic vibrations: the elastic energy, when the moving particles are slowed to the point where they cannot create further displacements [Seitz et al., 1956] and the inelastic energy when the electrons transfer energy to the atoms, a process requiring $> 10^{-11}$s [Davies et al., 1981].

Since the cascade lifetime is 10^{-13}s, about the time for one atomic vibration, the elastic energy might be converted to something approximating a Maxwell–Boltzmann distribution in 10^{-12}s [Sigmund, 1977], allowing the interpretation of the energy as local heating. Kelly [1978] quotes a maximum temperature rise of

$$\Delta T_{\max} \approx \frac{\Delta E}{\langle \Delta x^2 \rangle^{\frac{1}{2}} \langle \Delta y^2 \rangle 3Nk} \qquad 2.56$$

assuming that the heat capacity per atom is $3k$, where ΔE is the energy dissipated, $\langle \Delta x^2 \rangle^{\frac{1}{2}}$ is the mean depth-straggling of the ion, and $\langle \Delta y^2 \rangle^{\frac{1}{2}}$ is the mean lateral straggling. Then the duration of the cascade is approximately

$$\tau \approx \frac{\langle \Delta y^2 \rangle}{\kappa} \qquad 2.57$$

where κ is the thermal diffusivity. In quartz at 1000 K, $\kappa \approx 0.75$ mm^2/s, so if $\langle \Delta y^2 \rangle^{\frac{1}{2}} \approx 4$ nm, $\tau \approx 2 \times 10^{-11}$s.

Brinkman [1954,1956] noted that a thermal spike could be triggered by a displacement spike. Morgan et al. [1970] suggested the same for an ionization spike. Since, in the above example, τ is about the time required for energy to be transferred from the electrons to the atoms, much of the energy of the ion will go into a temperature rise before the heat is dissipated. Then, using equation 2.56, $\Delta T_{\max}$ for a 60

a 60 keV Bi^+ ion in quartz ($\langle\Delta y^2\rangle^{\frac{1}{2}} \approx 4.2$ nm, $\langle\Delta x^2\rangle^{\frac{1}{2}} \approx 7.7$ nm) is

$$\Delta T \approx \frac{60\text{keV} \cdot 0.2}{7.7\text{nm}(4.2\text{nm})^2(79.7\text{atoms/nm}^3) \cdot 3 \cdot 8.6 \times 10^{-5} eV/K} \approx 4300K$$

where 0.2 is the approximate fraction of the ion's energy deposited in the volume defined by $\langle\Delta y^2\rangle^{\frac{1}{2}}$ and $\langle\Delta x^2\rangle^{\frac{1}{2}}$ [Thompson et al., 1978]. A similar alternative is Carter et al.'s [1978] formula:

$$\Delta T_{\max} \approx \frac{\nu(E)}{(2\pi)^{\frac{1}{2}} C N \langle\Delta x^2\rangle^{\frac{1}{2}} \langle\Delta y^2\rangle} \qquad 2.58$$

where C is the heat capacity. An estimate of the high–temperature value for C was determined from the data of Armstrong et al. [1978] and Block et al. [1978] to be 3.7×10^{-4} eV/at·K. Then, $\Delta T_{\max}$ by equation 2.58 is approximately 3000 K. Equation 2.58 assumes that the inelastically deposited energy does not contribute to the spike; however, it is likely that ionization will contribute to the spike in an insulating material such as quartz.

Since quartz melts at 1883 K, these rough estimates indicate that the centre of the 60 keV Bi^+ cascade might resemble molten quartz for up to about 10^{-11}s, i.e. about 100 atomic vibrations. Then S_{thermal}, from equation 2.55, could attain values as high as $S_O \approx 4$ at/ion and $S_{Si} \approx 3$ at/ion for 60 keV Bi^+ in quartz. These values still result in an insignificant contribution by sputtering to the present damage observations.

2.4 Amorphisation due to Lattice Relaxation

In an extensive review of information on radiation damage in a large number of non–metallic solids, Naguib and Kelly [1975] proposed three criteria to determine whether a particular material would amorphise under ion impact, or remain crystalline. First Matzke and Whitton [1966] showed that anisotropic solids tend to

amorphise while cubic solids tend to remain crystalline. The exceptions to this trend are the elemental semiconductors, Si and Ge, both of which amorphise readily [Davies et al., 1967; Mayer et al., 1968]. The second criterion is the ionicity of the bond: materials with an ionicity < 0.47 tend to amorphise. The third criterion is whether the crystal can sustain a thermal spike. Naguib and Kelly [1975] proposed that the incident ion could produce a hot, liquid-like zone in the solid which would become an amorphous region if the ratio of the crystallisation temperature to the melting temperature were > 0.3. All of these criteria, when applied to quartz, indicate that it should amorphise.

An alternate model proposed by Swanson et al. [1971] is that amorphisation occurs when the local point defect concentration exceeds a critical level, at which point the lattice becomes unstable and relaxes into an amorphous state. From bond-stretching arguments, Swanson et al. [1971] proposed that the critical vacancy concentration should be about 4% in Ge. This effect has been studied extensively in Si [Thompson et al., 1980] and in GaAs [Stevanovic et al.,1983]. The relaxation can occur within each cascade if the local defect density is large enough, or after one or more cascade overlaps.

CHAPTER III: RUTHERFORD BACKSCATTERING/ CHANNELING ANALYSIS

3.1 Rutherford Backscattering

In Rutherford backscattering (RBS) analysis, MeV light ions such as $^4He^+$ collide with atoms in the target in a way which is described extremely well by the Rutherford model [Chu, Mayer, Nicolet, 1978]. The collisions are elastic, near–Coulombic collisions between the incident nuclei and the target nuclei. The Rutherford differential scattering cross–section is given by

$$\left(\frac{d\sigma}{d\omega}\right)_L = \left(\frac{Z_1 Z_2 e^2}{4E}\right)^2 \cdot \frac{4}{\sin^4\theta_L} \cdot \frac{\left(\left(1-\left(\frac{M_1}{M_2}\right)^2 \sin^2\theta_1\right)^{\frac{1}{2}} + \cos\theta_1\right)^2}{\left(1-\left(\frac{M_1}{M_2}\right)^2 \sin^2\theta_1\right)^{\frac{1}{2}}} \qquad 3.01$$

in lab coordinates, or

$$\left(\frac{d\sigma}{d\omega}\right)_{\rm cm} = \left(\frac{Z_1 Z_2 e^2}{4E_{\rm cm}\sin^2\left(\frac{\theta_{\rm cm}}{2}\right)}\right)^2 \qquad 3.02$$

in center–of–mass coordinates, where $\frac{d\sigma}{d\omega}$ is the scattering cross–section of the incident particles of atomic mass M_1, atomic number A_1, and energy E, scattered by a target atom of atomic mass M_2, atomic number A_2, into a unit solid angle at laboratory scattering angle θ_L. This is shown schematically in figure 3.1. Here the centre–of–mass angle is

$$\theta_{\rm cm} = \theta_L + \sin^{-1}\left(\frac{M_1 \sin\theta_1}{M_2}\right), \qquad 3.03$$

$$\text{and } E_{\rm cm} = \frac{E(M_1+M_2)}{M_2} \qquad 3.04$$

There is a small correction for electronic screening of the nuclear charge in the case of high atomic number target atoms [Ecuyer, Matsunami, Davies, 1979]: the

Coulombic cross-section should be multiplied by a factor

$$F = 1 - \frac{0.049 Z_1 Z_2^{-\frac{4}{3}}}{E} \qquad 3.05$$

where, in this case E is in keV.

When a beam of ions is incident on a target, the total number of particles scattered through an angle θ_L into a solid angle $\Delta\omega$ is given by:

$$Y = (N\Delta x) r \left(\frac{d\sigma}{d\omega}\right) \Delta\omega \qquad 3.06$$

where $N\Delta x$ is the areal density of target atoms and n is the number of incident particles.

Particles which are backscattered by the surface atoms of a solid target will have an energy E_1 dependent on their mass and that of the target atoms according to:

$$E_1 = K E_o \qquad 3.07$$

where E_o is the incident energy of the analysis beam and K, the kinematic factor, is given by

$$K = \frac{M_1 \cos\theta + \sqrt{M_2^2 - M_1^2 \sin^2\theta}}{(M_1 + M_2)^2} \qquad 3.08$$

Using equations 3.07 and 3.08 one can identify a target atom species by the energy of the particles scattered from it (through a well-defined, known angle).

Incident particles which penetrate beneath the surface will steadily lose energy through electronic excitation and ionization, before and after being backscattered. If the rate of energy loss as a function of energy, $\epsilon(E)$ is known, the energy spectrum of the backscattered particles can be converted into a depth profile of the target compostion, using $\Delta E = N \cdot \Delta t \cdot \epsilon(E)$. Here, Δt is the depth corresponding to ΔE.

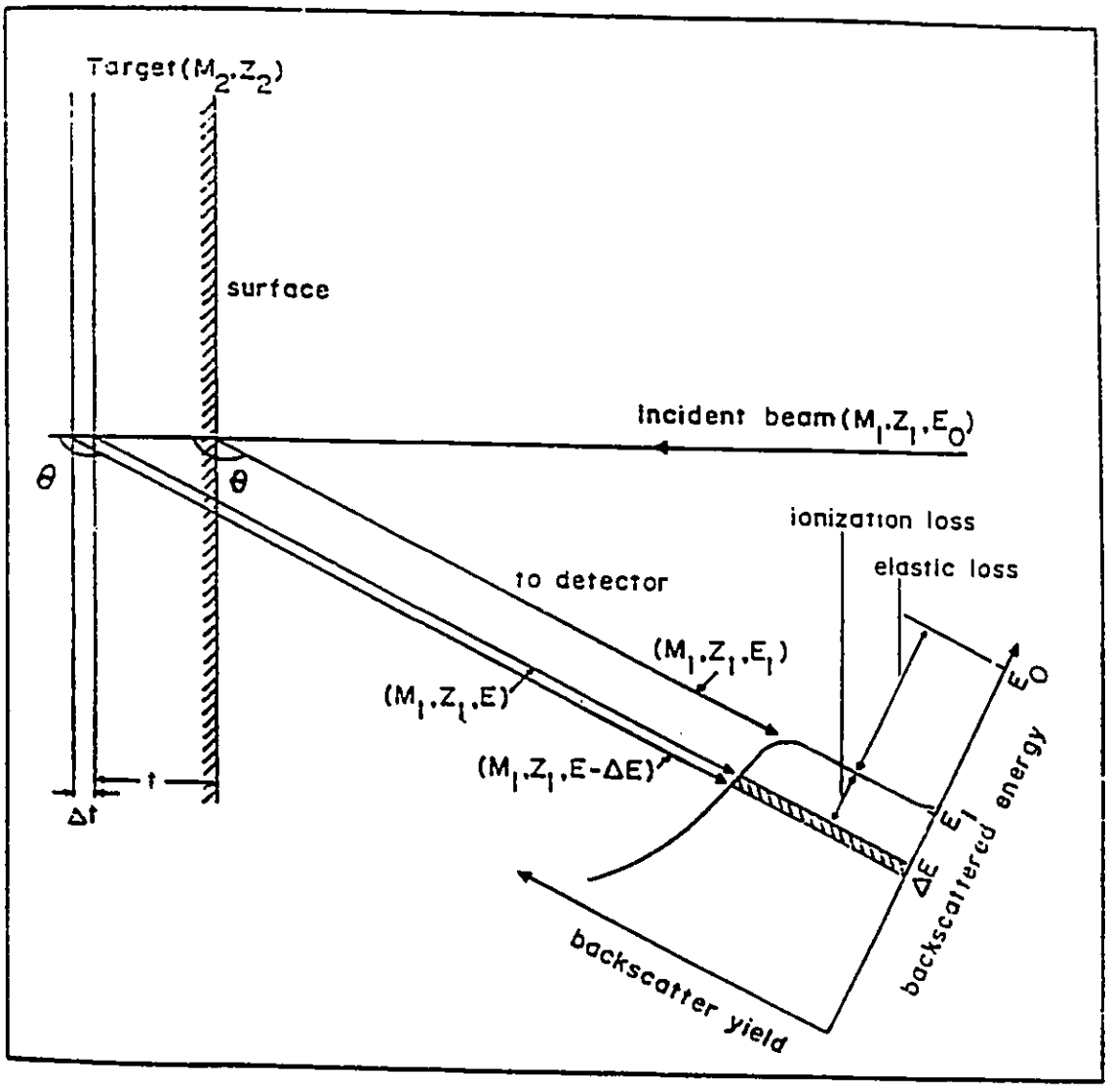

Figure 3.1: Principles of elastic scattering analysis, from Walker (1977).

3.2 Channeling

When an energetic ion beam (e.g., MeV $^4He^+$) is incident upon a crystal lattice in a direction parallel or very nearly parallel to a major axis or plane (as shown in

figure 3.2), most of the particles are gently steered by a series of glancing collisions with the lattice atoms [Chu, Mayer, Nicolet, 1978], as shown in figure 3.3. As long as the angle of incidence to the axis or plane is small enough, the electrostatic repulsion of the lattice nuclei will steer the particles down the "channel". This has the effect of drastically reducing the probability of a large angle scattering event by as much as a factor of one hundred, resulting in spectra like curve (a) in figure 3.4, as compared to the "random" spectrum, curve (b) in figure 3.4. Lindhard [1965] approximated the steering effect of the lattice atoms by a "row potential", $U(r)$, which is the average potential experienced by a particle at distance r from the lattice atom row:

$$U(r) = \frac{1}{d}\int_{-\infty}^{\infty} V\sqrt{r^2+z^2}\,dz \approx \frac{Z_1 Z_2 e^2}{d}\,ln\left(3\left(\frac{a}{r}\right)^2+1\right) \qquad 3.09$$

where: d is the distance between the atoms in the lattice row,

a is the effective Thomas–Fermi screening distance,

$$a = \frac{0.8853 a_o}{\sqrt{Z_1^{\frac{2}{3}}+Z_2^{\frac{2}{3}}}} \qquad 3.10$$

and a_o is the Bohr radius, 0.0528 nm.

The above steering potential applies only if

$$\Psi < \frac{r_{min}}{d} \qquad 3.11$$

where Ψ is the incident angle of the particles to the channel and r_{min} is the closest the particle may approach the lattice atom row without being scattered through a large angle. Lindhard chose the larger of the screening distance a or the transverse thermal vibration amplitude, $\rho_\perp$ as a first approximation to r_{min}.

For the particle to remain channeled, its transverse energy $E_\perp \approx E_o\Psi^2$ must be less than or equal to $U(r_{min})$, i.e.,

$$\Psi \le \Psi_c = \sqrt{\frac{U(r_{min})}{E}} \qquad 3.12$$

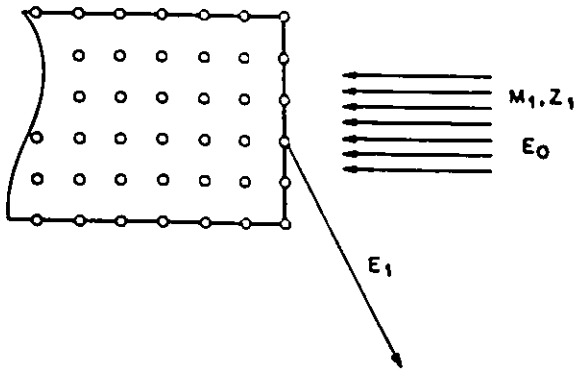

Figure 3.2: Analysis ions striking an aligned crystal, from Feldman et al. (1982).

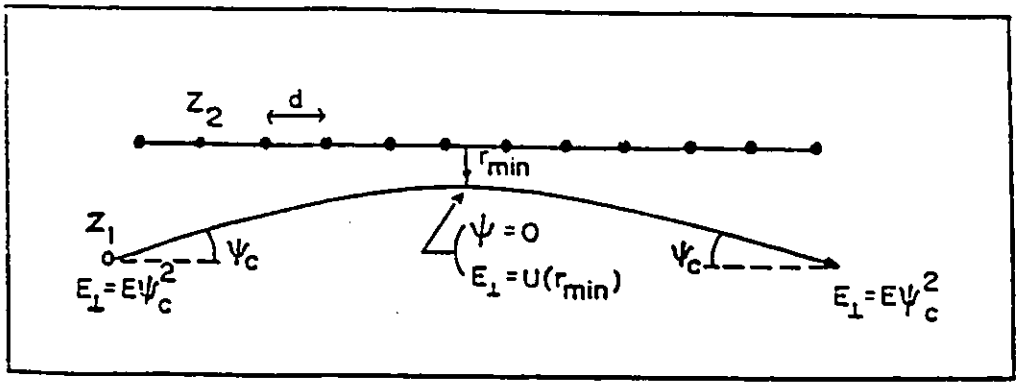

Figure 3.3: Schematic diagram of the channeling process, from Walker (1977).

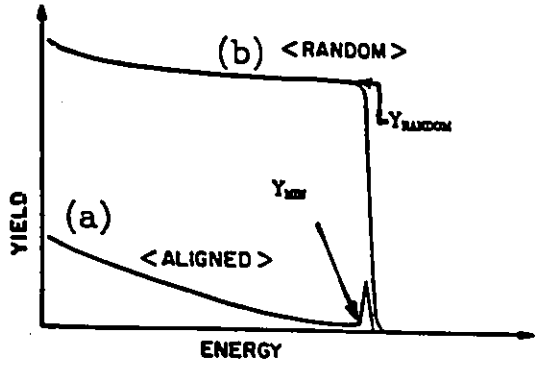

Figure 3.4: Typical RBS/channeling spectra, from Feldman et al. (1982).

where Ψ_c is called the critical angle. This is illustrated in figure 3.5. Thus,

$$\Psi_c \approx \Psi_1 \sqrt{ln\left(3\left(\frac{a}{r_{min}}\right)^2 + 1\right)}, \qquad 3.13$$

$$\text{where } \Psi_1 = \frac{Z_1 Z_2 e^2}{Ed} \qquad 3.14$$

For high energy particles such as $1-2$ MeV $^4He^+$, $a \approx 1.5 \cdot r_{min}$, hence $\Psi_c \approx \Psi_1\sqrt{2}$.

Experimentally, the quantity measured is $\Psi_{\frac{1}{2}}$, the "half- angle", or the tilt angle at which the yield is the average of the aligned yield and the random yield. This is illustrated in figure 3.5. Ψ_c is approximately the same as $\Psi_{\frac{1}{2}}$, and the two symbols are often used interchangeably.

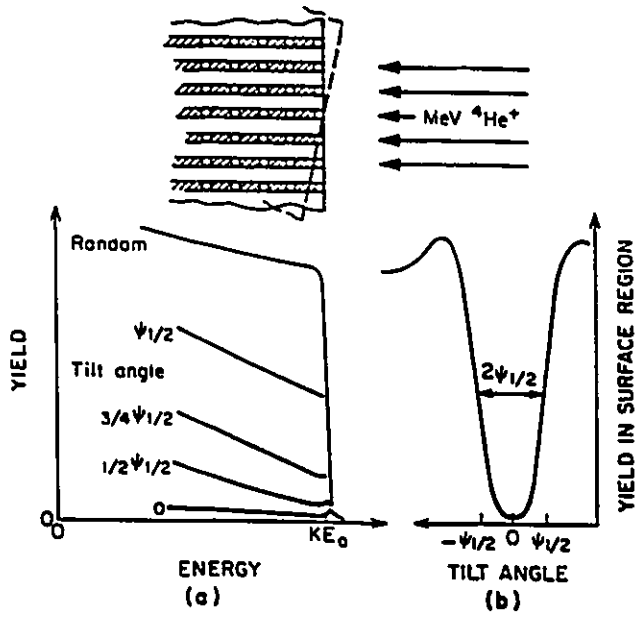

Figure 3.5: Random spectrum and aligned spectra at different tilt angles (a) and the angular yield profile (b) measured from the scattering yield in the surface region of the crystal as a function of tilt angle; from Chu et al., (1978).

Barrett [1971] determined that a value of $r_{min} = 1.2\rho$ gave the best fit in a Monte Carlo simulation determination of Ψ_c. Here, ρ is the thermal vibrational amplitude. In this model,

$$\Psi_c^B \approx 0.8 F_{RS}(\xi)\Psi_1 \tag{3.15}$$

where $\xi = \frac{r_{min}}{a}$ and F_{RS} is a function which is proportional to the square root of the Molière potential [Molière, 1947].

The relative minimum yield in a perfect crystal is

$$\chi_{min} = \frac{Y_{min}}{Y_{random}} \tag{3.16}$$

where Y_{min} and Y_{random} are the minimum (aligned) and random yields, as shown in figure 3.4. As a first approximation,

$$\chi_{min} \approx \frac{\pi r_{min}^2}{\pi r_o^2} \tag{3.17}$$

[Feldman et al., 1982], where $\pi r_o^2 = \frac{1}{Nd}$. As a rough estimate Feldman et al., [1982] chose $r_{min} \approx \rho'$, the mean thermal vibrational amplitude perpendicular to the channeling axis. Then

$$\chi_{min} \approx Nd\pi(\rho')^2 \tag{3.18}$$

In Barrett's [1971] Monte Carlo simulations, a better estimate of the minimum yield for crystals such as Si, Ge and W was found to be

$$\chi_{min} = 3N\pi d\rho^2\sqrt{1 + \left(\frac{\Psi_c^B d}{1.55\rho}\right)^2} \tag{3.19}$$

Abel et al. [1969, 1972] developed formulae more appropriate to the quartz system. This will be discussed in section 3.4.

3.3 Channeling–Damage Calculations

When a perfect crystal of α–quartz is aligned with the <0001> direction parallel to a well collimated beam, the RBS spectrum looks like curve (a) in figure 3.6. This is called a "virgin" spectrum. When the sample is aligned in a "random" direction, or if it is amorphous, the RBS spectrum will look like curve (b) in figure 3.6. A crystal aligned in the <0001> direction, with about 20% of the atoms in the surface 80 nm displaced from their lattice positions, will look like curve (c) in figure 3.6. Each of these spectra consists of two "sub–spectra" due to alpha particles scattered from either oxygen or silicon atoms in the target; because the kinematic factor (K in equations 3.07 and 3.08) for oxygen is smaller than that for silicon, the energy of the alphas scattered from the oxygen atoms is lower than that of alphas scattered from silicon atoms at the same depth. Therefore the oxygen "sub–spectrum" is superimposed on the silicon "sub–spectrum", as shown in curves (a) and (b) in figure 3.7.

Working with either "sub–spectrum", the high energy peak of the virgin spectrum represents alphas scattered from the surface or very near surface. The area under the surface peak represents initial damage (since no surface is perfect) and scattering from the surface layers of atoms in their proper lattice positions. The area under a surface peak of the damaged aligned spectrum is related to the quantity, distribution and nature of the defects present. The difference of these two areas is then used as a measure of the damage. If the damage is not too great and is dominated by randomly placed interstitial atoms and/or amorphous regions, the number of displaced atoms/mm^2 can be calculated as:

$$N_D \approx \frac{E_c \Sigma_{\text{net}}}{S_{\text{av}}} \cdot \frac{1}{Y_N - Y_A(a)/2} \qquad 3.20$$

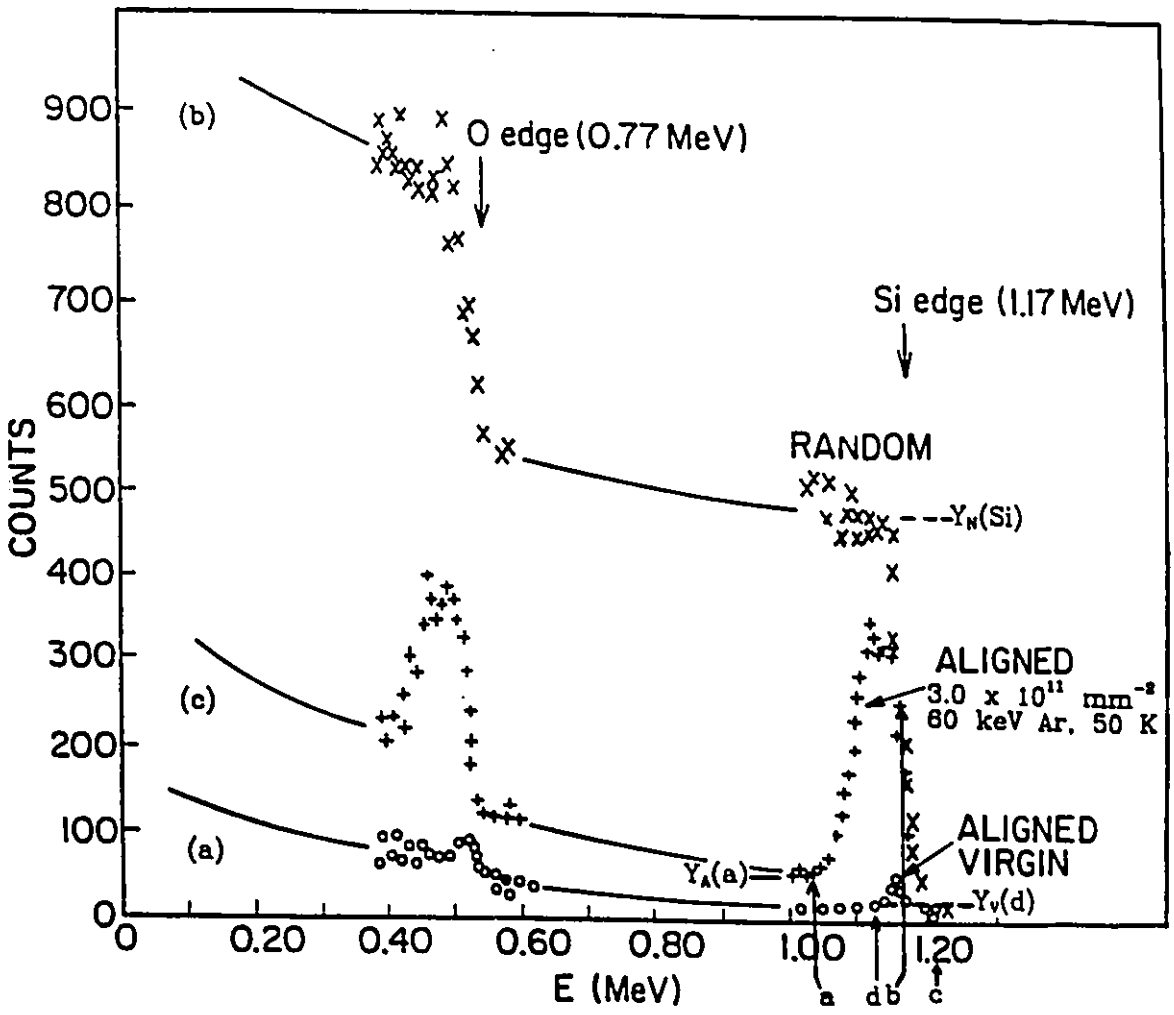

Figure 3.6: Typical RBS spectra of quartz at 50 K.

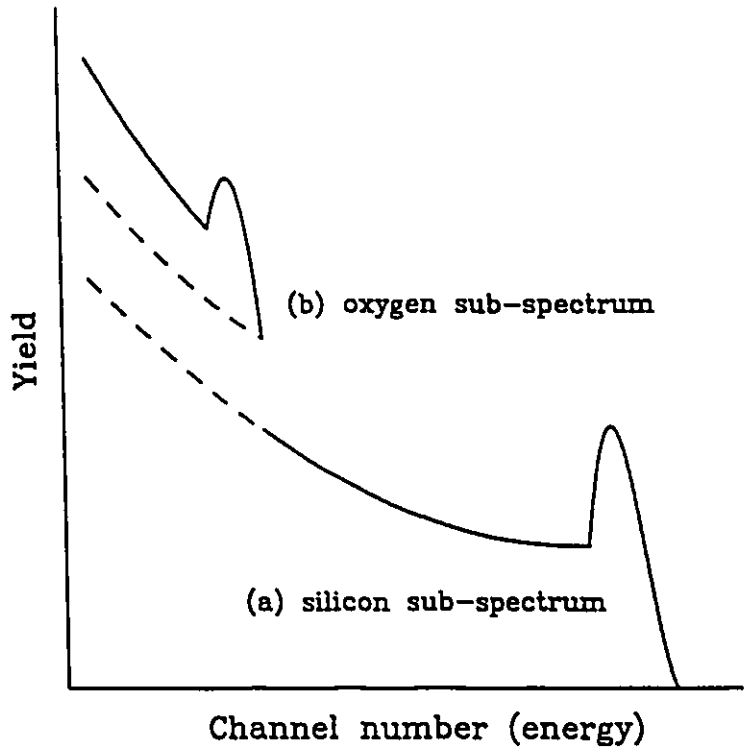

Figure 3.7: Sub–spectra of Si and O in quartz, from figure 3.6(c).

where: E_c is the energy scale (keV/channel),

S_{av} is the average electronic energy lost by the backscattered particles in entering, scattering and leaving the target, per target atom per unit area.

Y_N is the height of the random spectrum, scaled according to the relative beam fluences (n in equation 3.06),

$Y_A(a)$ is the height of the damaged aligned spectrum at channel a, which is the point where the damage peak appears to end (also scaled according to beam fluence).

Σ_{net} is the net area of the damage peak:

$$\Sigma_{net} = \sum_{a}^{c} Y_A - \left(Y_A(a)\frac{b-a+1}{2}\right) \quad - \quad \left(\sum_{d}^{c} Y_V - Y_V(d)\frac{b-d+1}{2}\right) \qquad 3.21$$

Here, Y_V is the yield in the virgin spectrum, scaled for the beam fluences. The values of channels # b, c, and d are illustrated in Figure 3.6. This calculation uses the "linear dechanneling" model, which is a good approximation for shallow damage profiles, i.e. damage which extends to depths of $\leq$ 100 nm. For damage extended to greater depths, the semi-empirical "single-scattering" model [Walker, Thompson, and Poehlman, 1977] is more appropriate. In this model, N_D is the integral of the depth profile, $N_D(x)$:

$$N_D(x) = N\frac{\frac{Y_A(x)}{Y_N(x)} - \chi'(x)}{1-\chi'(x)} \qquad 3.22$$

where: $\chi'(x) \approx \frac{Y_V(x)}{Y_N(x)}$ 3.23

x is the depth corresponding to channel i in the energy spectrum,

$Y_R(x)$ is the "dechanneling yield" at depth x.

$\chi'(x)$ is called the "dechanneling fraction", and was better approximated by Eisen [1973] as

$$\chi'(x) = \chi_V(x) + (1-\chi_V(x))\,P(x) \qquad 3.24$$

where $\chi_V(x)$ is the normalized yield from a virgin crystal. $\frac{Y_V(x)}{Y_N(x)}$ and $P(x)$ is the probability of the incident beam particles having a large-angle collision and being "dechanneled" (i.e. having a transverse energy greater than that needed to leave the channel) integrated from the surface to depth x. If the amount of disorder is small, and is dominated by randomly placed interstitials and/or amorphous regions, then $P(x)$ is directly proportional to $N_D(x)dx$.

More generally, the dechanneling per unit depth, $\frac{dP(x)}{dx}$, is given by

$$\frac{dP(x)}{dx} = \sum_i \sigma_D^i n_D^i(x) \qquad 3.25$$

[Feldman et al.. 1982], where σ_D^i is the dechanneling factor for one kind of defect, and n_D^i is the concentration of that defect at depth x. For point defects, Feldman et al. [1982] determined that

$$\sigma_D \approx \frac{\pi Z_1 Z_2 e^2 d}{2E} = 2.3 \times 10^{-18} \left(\frac{Z_1 Z_2 d}{E}\right) \text{mm}^2 \qquad 3.26$$

where d is in nm and E in MeV.

As long as the average number of atoms in amorphous regions is $< 10^{15}\text{mm}^{-2}$, these regions can be treated as if the atoms they contain were randomly placed interstitials. If $N_D > 10^{15}\text{mm}^{-2}$, then the single–scattering approximation assumed above is not accurate, and the "multiple scattering" model of Meyer [1971] and Sigmund and Winterbon [1974] is more appropriate. In this model the mean number of collisions of the channeled particles in an amorphous region with N_D atoms·mm^{-2} is

$$m = \pi a^2 N_D \qquad 3.27$$

Then $\chi_{\text{min}} = P(\tilde{\theta}_c, m)$, where $\tilde{\theta}_c$ is the reduced critical angle,

$$\tilde{\theta}_c = \frac{aE\Psi_c}{2Z_1 Z_2 e^2} \qquad 3.28$$

When $\Psi_c \approx 1°$, then $\tilde{\theta}_c \approx \frac{a}{d\Psi_1}$. Figure 3.8 shows $P(\tilde{\theta}_c, m)$, from Feldman et al. [1982].

In contrast, for a crystal in which the predominant type of damage is line dislocations, the increase in the surface peak is small or non–existent, but the dechanneling cross–section is fairly large:

$$\sigma_D \approx \frac{Kab}{\Psi_1} \qquad 3.29$$

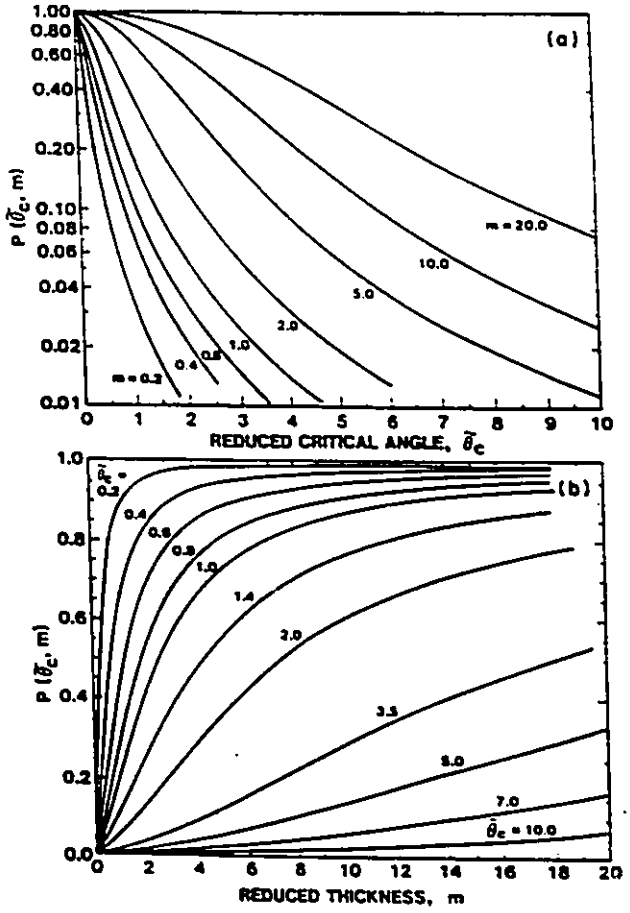

Figure 3.8: Fraction of non-channeled particles (a) as a function of reduced critical angle, and (b) as a function of reduced fillm thickness; from Feldman et al. (1982).

where: Ψ_1 is approximately Ψ_e (see equations 3.11–3.14),

K is a constant dependent on the type of dislocation and its orientation distribution,

a is the Thomas-Fermi screening distance,

and b is the Burger's vector for the dislocations.

The average value of K is about 0.4 – 0.5.

These different dechanneling factors also have different dependences on the incident energy of the analysis beam, as shown schematically by Figure 3.9, from Feldman et al. [1982].

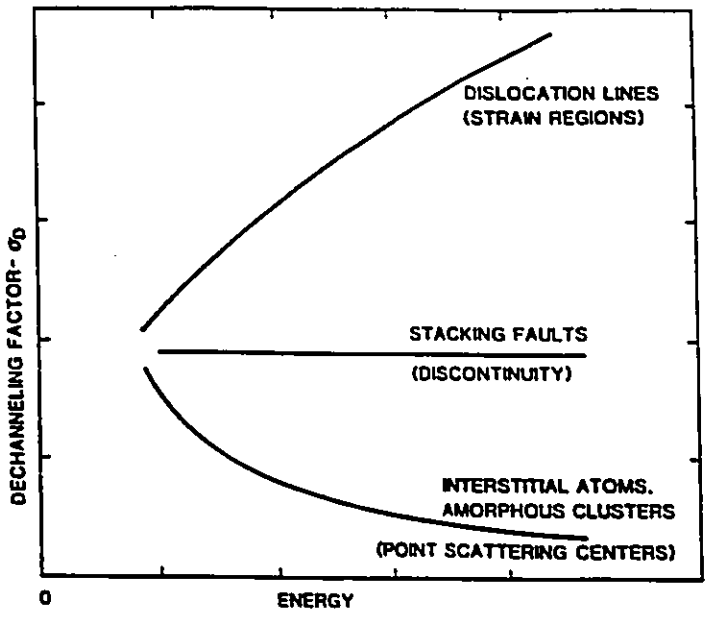

Figure 3.9: Schematic diagram of the energy dependence of the dechanneling factor for various types of defects; from Feldman et al. (1982).

3.4 Channeling in Quartz

The interpretation of channeling data from quartz is somewhat more complex than in the case of relatively simple monatomic structures such as silicon. Figure 3.10 shows the structure of quartz; figure 3.11 shows the equipotential contours for quartz at 300 K, calculated by Abel et al. [1969] using the continuum model of Lindhard [1965]. These contours indicate the transverse potential which would be experienced

by a particle travelling parallel to the <0001> axis in quartz. There are two sub-lattices: oxygen and silicon: because of their lesser atomic charge, the oxygen atom contribution can be ignored except at very small distances from the oxygen rows.

Abel et al. [1969, 1972] studied channeling in quartz extensively, at 300 K. They separated the sub-lattices by using 900 keV deteurium backscattering from the silicon sub-lattice and the $O^{16}(d,p)O^{17*}$ reaction for the oxygen sub-lattice. In their earlier work [1969] they found that the values of χ_{min} were 1.5 - 1.8 times that predicted by their adaptation of equation 3.18:

$$\chi_O = N\pi d\,(2a_O^2 + b_{Si}^2) \qquad 3.30$$

$$\chi_{Si} = N\pi d\,(a_{Si}^2 + 2b_O^2) \qquad 3.31$$

where: a_O and a_{Si} are the Thomas-Fermi screening distances for oxygen and silicon, respectively;

b_{Si} is the radius around the silicon rows where the continuum potential is approximately $E_1^c(O)$, the critical energy for dechanneling a particle relative to the oxygen rows;

b_O is the radius around the oxygen rows where the continuum potential is approximately $E_1^c(Si)$;

and $E_1^c = E_o\Psi_c^2$.

In the later work [1972] they improved the calculated values of χ_{min} by adding in quadrature the root-mean-square thermal vibrational amplitude, ρ, in the plane perpendicular to the channel axis. Thus:

$$\chi_O = N\pi d\,(2\,(a_O^2 + \rho_O^2) + (b_{Si}^2 + \rho_{Si}^2)) \qquad 3.32$$

$$\chi_{Si} = N\pi d\,(2\,(a_{Si}^2 + \rho_{Si}^2) + (b_O^2 + \rho_O^2)) \qquad 3.33$$

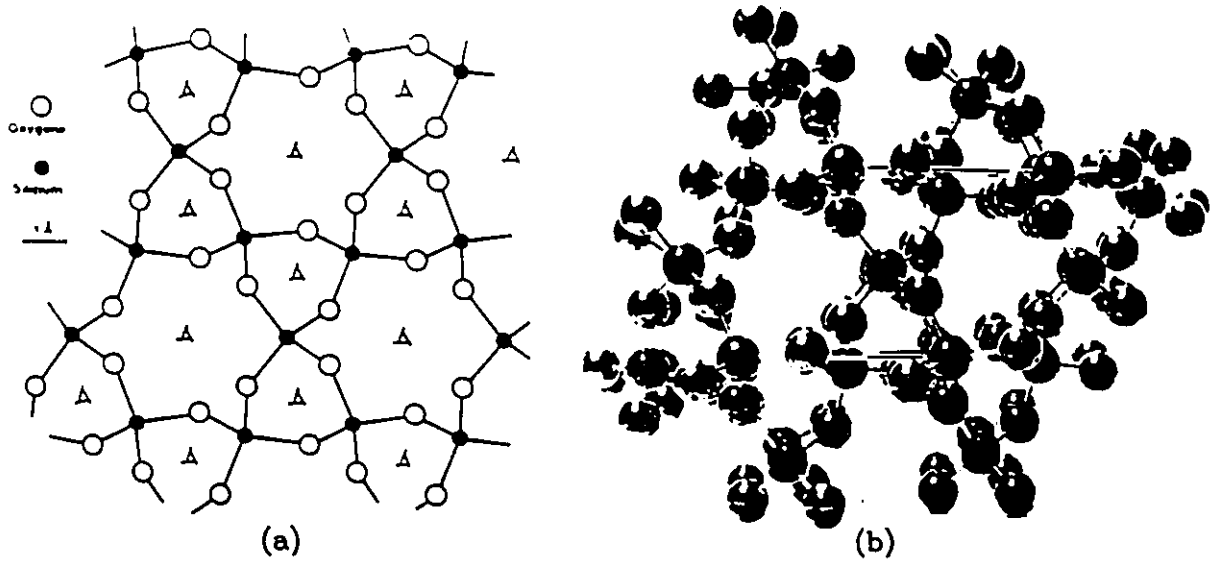

Figure 3.10: Quartz structure, looking down the c–axis; from Abel et al. (1969).

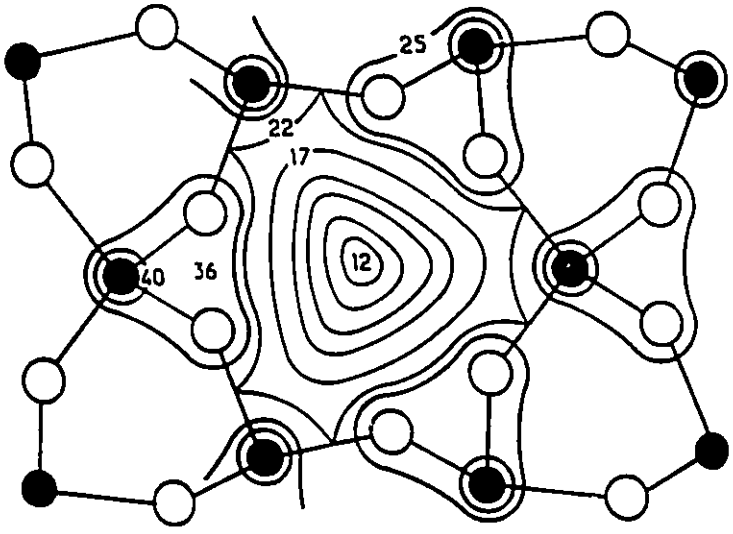

Figure 3.11: Quartz equi–potential contours in electron volts, at 300 K; from Abel et al. (1969).

where: N is the density of SiO_2 molecules. $2.66 \times 10^{19} mm^{-3}$,

$d = 0.54$ nm,

$\rho_O = 10.5$ pm,

$\rho_{Si} = 6.0$ pm,

and the a and b values are in the range of 10 – 30 pm.

They determined the values of ρ from the data of Young and Post [1962], and used them to calculate $\chi_{min}(O)$ =0.087, and $\chi_{min}(Si)$ =0.038. These are in good agreement with the Abel et al. [1969] observed values of 0.08 and 0.04 respectively. In the present work the observed values are a bit lower because they were determined at lower temperature: typical values are 0.069 and 0.031.

Chu et al. [1978] indicate how to calculate ρ given the temperature and θ_D, the Debye temperature of the crystal:

$$\rho \approx 1.21 \frac{\frac{\varphi(x)}{x} + \frac{1}{4}}{M\theta_D} \qquad 3.34$$

where $x = \frac{\theta_D}{T}$ and $\Phi(x)$ is tabulated in Mayer and Rimini [1977]. Young and Post [1962] found the behaviour of quartz between $155K$ and $300K$ to be consistent with $\theta_D \approx 487K$, $\pm 50K$. The variation in θ_D is not statistical; rather it is dependent upon the crystal direction and the mass of the vibrating atom. In the <0100> direction, $\theta_D \approx 435K$ for oxygen and $510K$ for silicon; in the <0001> direction, $\theta_D \approx 546K$ for oxygen and $540K$ for silicon. Table 3.1 shows the values of ρ calculated for $T = 50K$ and $300K$, using these values of θ_D. It also shows the Young and Post [1962] values for comparison. These calculations show that, in this respect, quartz is only a rough approximation of a Debye crystal. The derived values of ρ would seem to be reliable to about $\pm 20\%$. Using these values, the important parameters for channeling were determined and listed in Table 3.2.

Table 3.1: Thermal Vibrational Amplitudes for Quartz, in pm

	T (K)	Oxygen				Silicon			
		x	y	z	xy(RMS)	x	y	z	xy(RMS)
Young and Post values	300	7 - 13 (projections estimated)		~9	(10.5) (projection calculated by Abel et al.)	4.93	7.23	8.53	6.0
values from equation 4.44	30	12.4		10.0	12.4	8.05		7.63	8.05
	50	7.6		6.6	7.6	5.20		5.05	5.20

Table 3.2: Channeling Parameters for Mev $^4He^+$ Incident on α-Quartz

Atom	E_0 (MeV)	a (pm)	T (K)	p (pm)	ψ_1 (°)	ψ_2 (°)	E_c (eV)	r_{min} (pm)	b (pm)	χ_{min}
Si	1.0	15.7	50	5.2	0.70	0.67	137	4.3	21.1	0.021
Si	2.0	15.7	50	5.2	0.49	0.47	135	4.3	21.8	0.021
Si	2.0	15.7	300	6.0	0.49	0.43	113	5.0	28.6	0.029
O	1.0	17.9	50	7.6	0.53	0.49	73	6.3	6.3	0.055
O	2.0	17.9	50	7.6	0.37	0.34	70	6.3	6.5	0.057
O	2.0	17.9	300	10.5	0.37	0.28	48	8.7	8.5	0.077

* using $r_{min} = \ln 2$, following Abel et al. [1972]

† b= radius at which the potential from the atom string equals E_c of the other atom string, estimated using the continuum potential, equation 4.18.

Table 3.3: Theoretical Number of Atoms Displaced by MeV $^4He^+$ Ions Incident on Quartz, in the Surface 50 nm

E_0	$dN_D(O)/d\phi$ elastic	atoms/ion inelastic	$dN_D(Si)/d\phi$ elastic	atoms/ion inelastic
1.0 Mev	0.54	0.53 - 2.6	0.27	0.18 - 0.92
2.0 MeV	0.30	0.40 - 2.0	0.15	0.14 - 0.69

N.B. 50 nm of quartz corresponds to about 4×10^{15} atoms/mm^2. Also note that the elastic damage rate assumes a randomly aligned crystal. If the crystal is aligned, the elastic damage rate should be multiplied by χ.

In the above calculations it was assumed that the surface of the quartz crystal was undamaged. In fact, Abel et al. [1972] found that the surface peak corresponded to a damage depth of about 3 nm, even after an etch in dilute HF. This corresponds to about 2.4×10^{14} atoms/mm^2. According to Feldman et al. [1982], an ideal surface of quartz should contribute only about 1.4×10^{14} at/mm^2. The extra atoms contributing must be out of their lattice sites due to surface damage and relaxation. Using equation 3.26 [Feldman et al., 1982], the dechanneling contributed by this surface damage would be approximately 0.006 at 1.0 MeV and 0.012 at 2.0 MeV; these values should be added to the theoretical χ_{min} values, when comparing them to observed χ_{min} values.

Abel et al. [1969, 1972] observed that the MeV analysis ion beam created damage in the quartz crystals, and that the oxygen sublattice was more sensitive to this damage than the silicon sublattice. Calculations of the elastic energy deposition of MeV $^4He^+$ in quartz, explained in section 2.2.6, yielded a theoretical number of elastically displaced atoms per incident ion, as given in Table 3.3. This calculation is for the number of atoms displaced by the $^4He^+$ ions in the range of depth which contributes to the surface peak. Also given in Table 3.3 are the number of displacements expected to be caused by the inelastic energy deposition of each MeV $^4He^+$. These numbers are given as a range of values, since the efficiency of inelastically deposited energy in creating defects in quartz is not agreed upon in the literature [Fischer et al., 1983a: Norris and EerNisse, 1974; Howitt and DeNatale, 1983]. The range of efficiencies may be due to the damage level present when the efficiency was measured: it seems reasonable that the effective displacement energy would be reduced as the damage level increased. If photolysis is the process, then the defect creation efficiency may be as large as one–fifth that of the elastic process [i.e. E_d(photolysis) $\approx$50 eV, whereas for oxygen E_d(elastic) $\approx$10 eV]. However, the fraction of defects which self–anneal is

expected to be very dependent upon the local damage density and upon the inelastic energy deposition density.

3.5 Interpretation of RBS/Channeling Data

As discussed in section 3.3, there are two basic kinds of information provided by RBS/channeling spectra: the damage peak and the dechanneling level. In the ideal case of a crystal with low-level damage in the form of point defects or small amorphous regions at or near the surface, equations 3.20 and 3.24 – 3.26 apply fairly well. Then $N_D(x)$ is a good approximation of the damage profile of the crystal. However, in the usual situation there are complicating factors.

The first of these factors is the fact that the gentle steering of a channeled beam by the potential field of the crystal will act to focus the beam towards the center of the channels, where the potential is lowest [Chu et al., 1978]. This "flux peaking" makes the ion beam less sensitive to displaced atoms positioned near the atom rows, and more sensitive to displaced atoms positioned in the center of the channels. In a crystal with a low level of damage, at depths great enough to establish the equilibrium beam flux, this effect could reduce the sensitivity near the atom rows by as much as a factor of five or more, and increase the sensitivity near the center of the channels by as much. Thus the scattering yield would actually be proportional to the convolution of the damage distribution with the depth-dependent beam flux distribution, rather than simply proportional to the number of displaced atoms.

The effect of flux-peaking will be ignored in the calculations which follow because the wavelength, λ, is large enough that the average effect is very small: λ is approximately equal to the damage range. Furthermore, flux-peaking is drastically reduced in the presence of significant damage and lattice strain, which is the case

for most of the data which follow. The Bragg rule will be used to calculate stopping powers for this data.

Second, Quéré [1976] points out that RBS/channeling detects not only atoms which have been displaced (i.e. forcefully removed from their lattice sites with the breaking of all chemical bonds) but also atoms which have been shifted from their normal lattice sites by as little as one Thomas Fermi screening distance (a, approximately 10 – 20 pm). All damage creates strain, so that many atoms surrounding a vacancy, interstitial, or any other defect, may scatter the analysis beam as if these atoms were themselves interstitials. In some highly constrained conditions [Walker, 1977; Parikh, 1985], this can be detected by comparing the dechanneling yield to the damage peak, using the cross-sections described in section 3.3. However, if there is a larger strain contribution to the damage peak, it is more difficult to determine the damage profile accurately. At very low damage levels this effect is somewhat reduced by flux peaking; however, flux peaking is easily "washed out" by the presence of strain or other damage.

Third, calculations of the depth profile of the damage are strongly affected by the values of the inelastic stopping power, $(\frac{dE}{dx})_e$. The simplest way to calculate this stopping power in a compound such as quartz is to average the elemental stopping powers according to the stoichiometry of the compound. This is called the "Bragg rule" [Bragg and Kleemen, 1905]. For a sapphire crystal (Al_2O_3) Drigo et al. [1977] used the experimental values determined by L'Hoir et al. [1975], which were about 10% lower than those determined by using the Bragg rule and the elemental stopping powers reported by Ziegler and Chu [1974]. Drigo et al. [1977] indicate that solid oxides in general seem not to obey the Bragg rule exactly; however, it is a good first approximation. Biersack [1987] tabulates stopping powers for silica which correspond

to values 4 - 7% lower than those obtained using the Bragg rule anf the data of Ziegler and Chu [1974].

Furthermore, it has been observed [Eisen, 1966; Clark et al., 1970; Datz et al, 1970] that the stopping power of a well-channeled beam can be as much as 50% lower than that of a beam entering the same crystal in a "random" direction, although for the case of 1 – 2 MeV $^4He^+$ the stopping power reduction is closer to 20%. This is because the beam is shifted towards the center of the channels (flux peaking); since the electron density is lower there, the rate of inelastic collisions is reduced. Drigo et al. [1977] assume that this effect in particular, and flux peaking in general, are not important factors in the interpretation of RBS/channeling data in sapphire at shallow depths (< 50 nm), because the analysis beam particles have not undergone enough collisions to establish equilibrium flux peaking.

When a previously channeled particle backscatters from a target atom the detected energy loss is dominated by the inelastic losses suffered on the way out of the crystal, when the particles generally are not travelling parallel to a crystal axis. For example, if one were analysing a quartz crystal with a 2 MeV $^4He^+$ beam at a scattering angle of 160°, the stopping power on the way in would be about 40 eV/10^{13} atoms/mm^2, using the Bragg rule and the tables of Chu et al. [1978]. If about 80% of the particles are channeled and the channeled particles have a 50% lower stopping power (the worst-case estimate), the average stopping power is reduced to about 24 eV/10^{13} atoms/mm^2. The back-scattered particles are detected with an energy $E_2 = (E_o - \Delta E_{in})K - \Delta E_{out}$. The change in ΔE_{in} is reduced for silicon (K = 0.57) and reduced even more for oxygen (K = 0.37). The stopping power for the scattered particles is greater because their energy is lower: > 55 eV/10^{13} atoms/mm^2 for particles scattered from Si, and > 59 eV/10^{13} atoms/mm^2 for particles scattered

from O, if the incident beam is perpendicular to the target surface and therefore the outgoing pathlength is increased by $\frac{1}{\cos 20^\circ}$. The 50% reduction in the incident stopping power only reduces the detected energy loss, $\Delta E = k^2 E_o - E_2$, by 6%–10%. Abel et al. [1969, 1972] concluded that the actual channeling and flux–peaking effects on the stopping power are less than 50%. and so can be safely ignored, in most cases.

CHAPTER IV: EXPERIMENTAL TECHNIQUES

4.1 Rutherford Backscattering/Channeling

4.1.1 Accelerators and Vacuum System

The main part of the experimental data in this thesis was obtained using the McMaster 0.5 – 3.5 MV KN Van de Graaff accelerator and 10 – 150 kV ion-implanter, the former for analysis and the latter to create damage in the surface of the quartz crystals. Figure 4.1 is a schematic diagram of the facility. Ions are produced and electrostatically accelerated in the accelerators, travel through a vacuum of $\approx 10^{-6}$ torr in the beamline, and are "analysed" by the magnet. Only ions with the correct charge–to–mass ratio will pass through the magnet; all others will strike the magnet chamber walls. A feedback circuit is used to stabilise the beam energy to ± 3 keV for ions from the Van de Graaff, and ± 1 keV for the implanter. Note that the two accelerators are *on–line*, i.e., ions can be steered onto the target from either accelerator by simply adjusting the magnet field.

For RBS/channeling measurements, the $^4He^+$ beam was typically 1 – 2 MeV, and about 10 nA. The beam was collimated by passing it through two circular apertures 0.75 mm in diameter, about 1 m apart, so that the angular spread of the beam would be ± 0.045°. The beam was steered onto the target, positioned on a two–axis goniometer. The particles scattered through 150° were energy–analysed by a silicon surface–barrier detector, hooked up to the electronic data–acquisition system shown schematically in Figure 4.2. (The detector was repositioned part–way through this project, so that the scattering angle changed to 160°.)

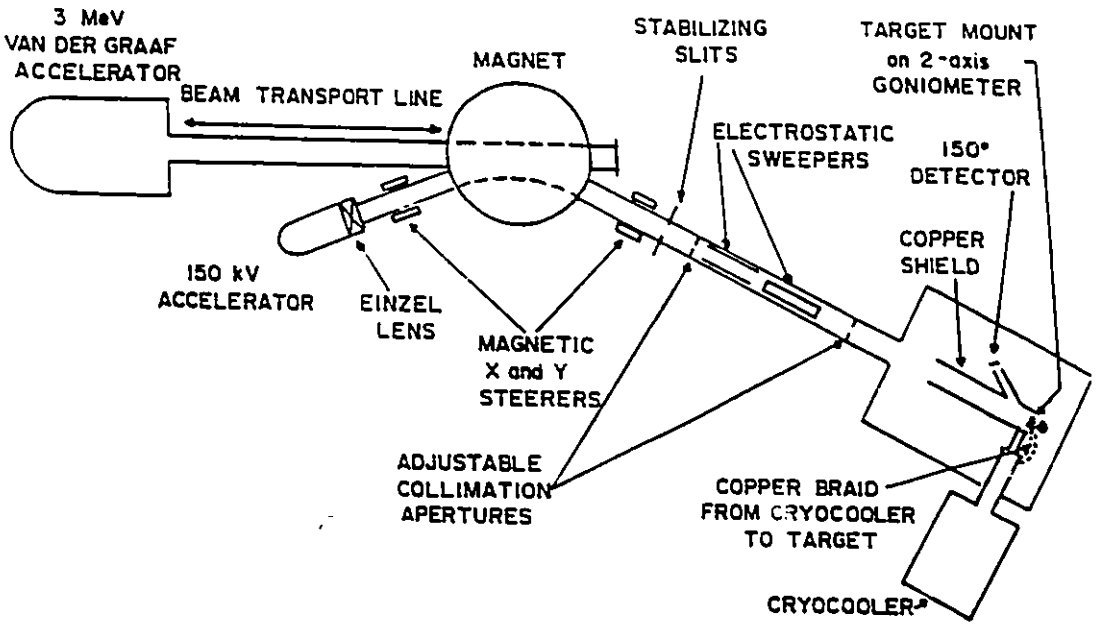

Figure 4.1: Schematic diagram of the McMaster on-line RBS and Ion-Implantation Facility.

For ion-bombardment to create damage, the ion beam from the implanter was steered through a circular off-axis aperture, 2 mm in diameter, then electrostatically swept across a circular 4 mm aperture in front of the target, in order to obtain a uniformly bombarded area of about 6-8 mm in diameter. The off-axis geometry insured that no neutral particles from the ion-source could strike the target. Since the ions are counted by measuring the accumulated charge at the target, a significant fraction of uncharged particles would result in fluence values lower than the actual fluence. This was considered not to be a problem for the much higher-energy analysis ions, since their cross-section for charge-exchange with residual gas in the beamline is much lower. Typical current densities for these bombardments were 0.1 - 10 nA mm^{-2}.

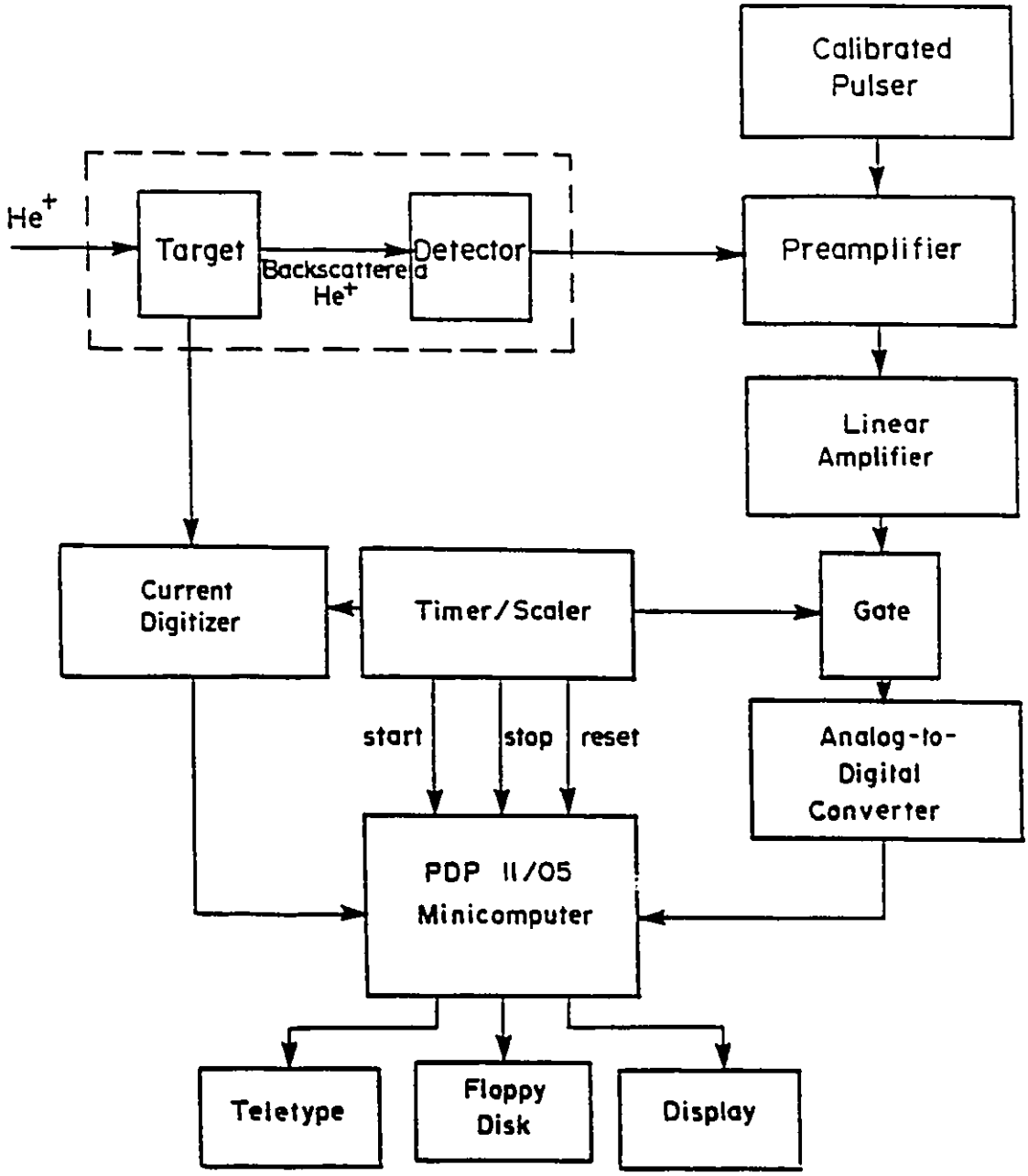

Figure 4.2: A block diagram of the data acquisition system.

4.1.2 The Target Chamber

The target chamber, shown schematically in Figure 4.3, was kept at a pressure of less than 10^{-9} torr during the experiments, in order to minimize the effects of surface–contamination on the experiments. A cryo–shield surrounding the target was cooled to < 30 K to freeze out hydro–carbons back–streaming from the vacuum pumps. The goniometer could rotate the target ± 180°, with a resolution of 0.1°, and tilt the target ± 30°, with a resolution of 0.025°. The target could be connected to the cryo–cooler by a copper braid, and cooled to < 50 K.

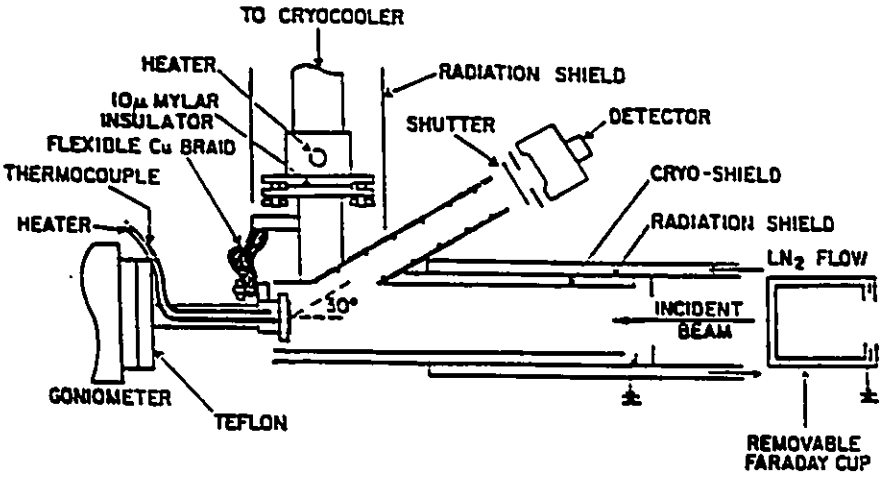

Figure 4.3: Schematic diagram of the target chamber.

Ion fluences were determined by measuring the current at the target. The copper cryo–shield was electrically isolated, and the secondary electron current on it was added to the target current, as otherwise the measured fluence values would be larger than the true fluences. Secondary electron loss was minimized by the presence of suppression wires biased to -220 V, positioned at the front and back of the cryo–shield.

4.1.3 Data Acquisition Electronics

When a backscattered analysis particle enters the surface-barrier detector it creates a surge of electron-hole pairs, which are swept out of the detector by an electric field. The resultant current pulse is proportional to the energy of the backscattered particle. This signal is amplified and shaped in a Canberra 1408 pre-amplifier, and an Ortec 572 linear amplifier, digitized by a Tracor-Northern 8192 ADC, and processed by a PDP 11/05 computer with a pulse-height analysis program. This system is described in more detail in Walker [1977].

4.1.4 Target Preparation

Single crystals of quartz were obtained from Adolph Meller Co. of New York. As purchased, the crystals were 7 mm in diameter and 1 mm thick, with one highly polished face. They were then mechanically polished (on the previously unpolished face) to a thickness of about 50 μm, cleaned briefly in a boiling solution of H_2SO_4+H_2O_2 and briefly etched in 5% HF (aqueous). The samples were mounted on the goniometer head with silver colloid solution (silver dag) to provide a conducting contact. The samples were thinned because it reduced the charge buildup on the insulating surface. When 1 mm thick samples were used, the charge buildup often resulted in sparks which produced considerable noise in the detectors. When charge buildup was not a problem (presumably because of carbon contamination on the surface allowing charge to leak off) the aligned spectra were not significantly different from those of the thinned samples.

4.1.5 Experimental Procedure

In most of the experiments the sample was cooled to < 50 K, in order to minimize the dechanneling yield, which is enhanced by thermal vibration. The quartz crystals were aligned with the <0001> axis parallel to the $^4He^+$ beam by measuring the backscattering yield as the tilt and azimuth were scanned. When the yield dropped to a minimum, the alignment was complete. The "virgin" spectrum was then collected, on a nearby spot which had not been damaged by the analysis ions. Then the sample was tilted to about 6°, to present a "random" alignment to the ion beam, and low energy (30 – 200 keV) ions would be implanted, to damage the surface of the crystal to a depth of 50 – 300 nm. The sample would be alternately aligned and analysed, and misaligned and implanted, until the backscattering yield corresponding to the damage region indicated that the damage had saturated. For comparison, a spectrum would then be taken of the sample in the "random" alignment.

In the first experiment the sample was tilted to 6° and then continuously rotated azimuthally during the implants and the collection of the "random" spectrum. Since it was found that the azimuthal rotation did not significantly affect either the random spectrum or the implant ion damage distribution, the sample was not rotated in later experiments, just tilted. This is in contrast to similar work with cubic lattice semiconductors where Thompson et al. [1977a, 1977b, 1978] found that continous azimuthal rotation was essential in order to present a random alignment.

4.2 Electron Microscopy

Attempts were made to image the effects of the ion damage by electron microscopy. Carbon replicas were made of the surface of an ion-bombarded quartz

crystal, before and after etching in 5% HF (aqueous), to try to see individual cascade dimensions, since the etch rate for the damaged regions is greater than that of the undamaged regions [Dran et al., 1980]. Unfortunately, the resolution of the replicas was of the order of the cascade dimensions, so no clear cascade images were obtained. Figure 4.4 shows an electron micrograph of a sample implanted over half of its surface to a fluence such that the implanted region was highly damaged, and then etched briefly in HF. The step is approximately 50 nm high, corresponding to the depth of the ion-damaged region.

Attempts to observe quartz crystals directly in the transmission electron microscope proved very difficult, because of the damage caused by the electron beam. Since sample preparation for the T.E.M. was also difficult, it was decided that T.E.M. observations should be left for future research.

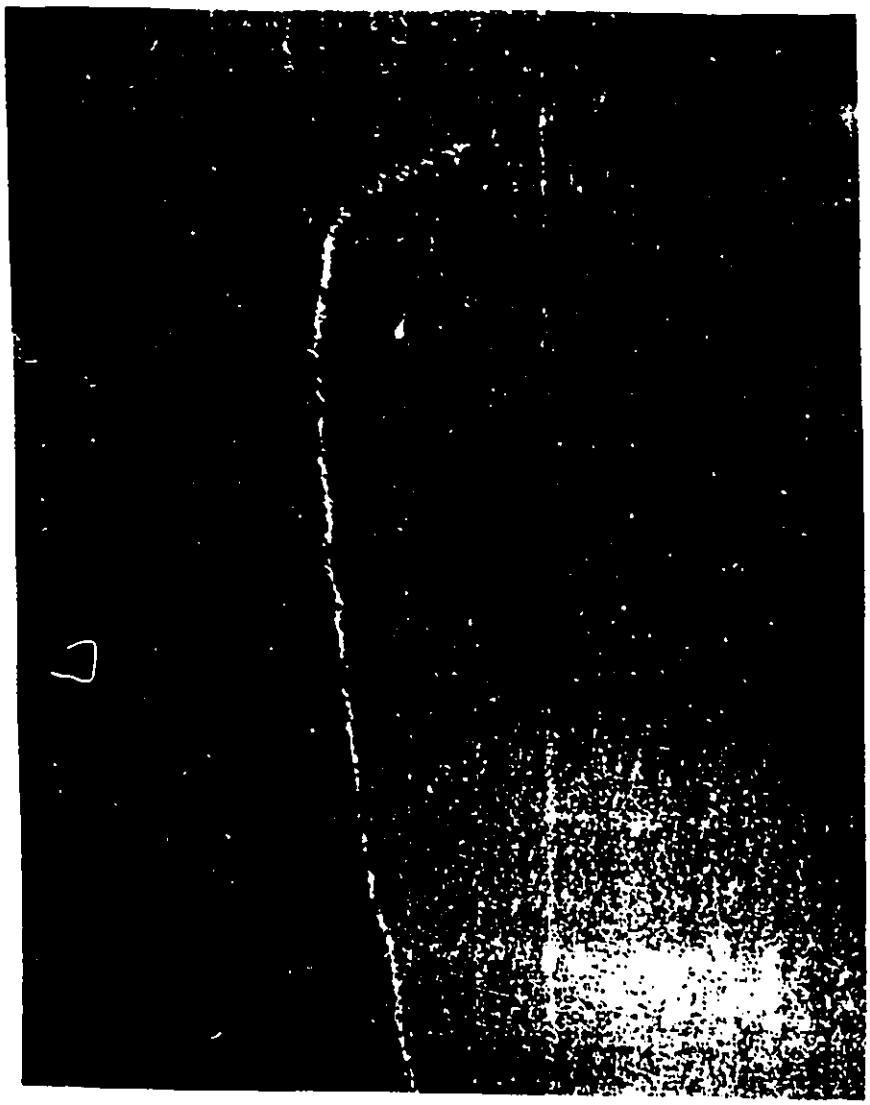

Figure 4.4: C/Au replica of an etch–step in quartz: electron micrograph, 24,000 x magnification.

CHAPTER V: RBS/CHANNELING RESULTS AND CALCULATIONS

5.1 Introduction

This chapter contains the results of Rutherford backscattering/channeling analysis of the damage produced by ion- implantation of α–quartz. The samples were analysed *in–situ* using $^4He^+$ ions with energies of 1 - 2 MeV. Ions ranging from $^4He^+$ to $^{209}Bi^{++}$ were implanted at energies of 15 – 200 keV, both at low temperature (40 - 50 K) and at room temperature (295 – 300 K).

Section 5.2 contains the data on the implantation damage to single crystals of α–quartz, related sputtering experiments, and some results published by others. Section 5.3 reports the damage caused by analysis ions and the related data of other researchers.

5.2 Implantation Damage to Alpha-Quartz Crystals

5.2.1 Low Temperature Experiments

Figure 3.6 shows typical RBS/channeling spectra for quartz: in this case the crystal was bombarded with 60 keV Ar^+ at low temperature, and analysed with 2.0 MeV $^4He^+$. Shown are the aligned spectrum for the undamaged crystal, the aligned spectrum for the crystal after an intermediate Ar^+ fluence (1.5×10^{11} mm^{-2}), and the spectrum from $^4He^+$ ions incident in a random direction. The peaks, corresponding to displaced Si and O atoms in the near- surface region, are used to determine the concentrations, $N_D(Si)$ and $N_D(O)$, of displaced Si and O atoms respectively.

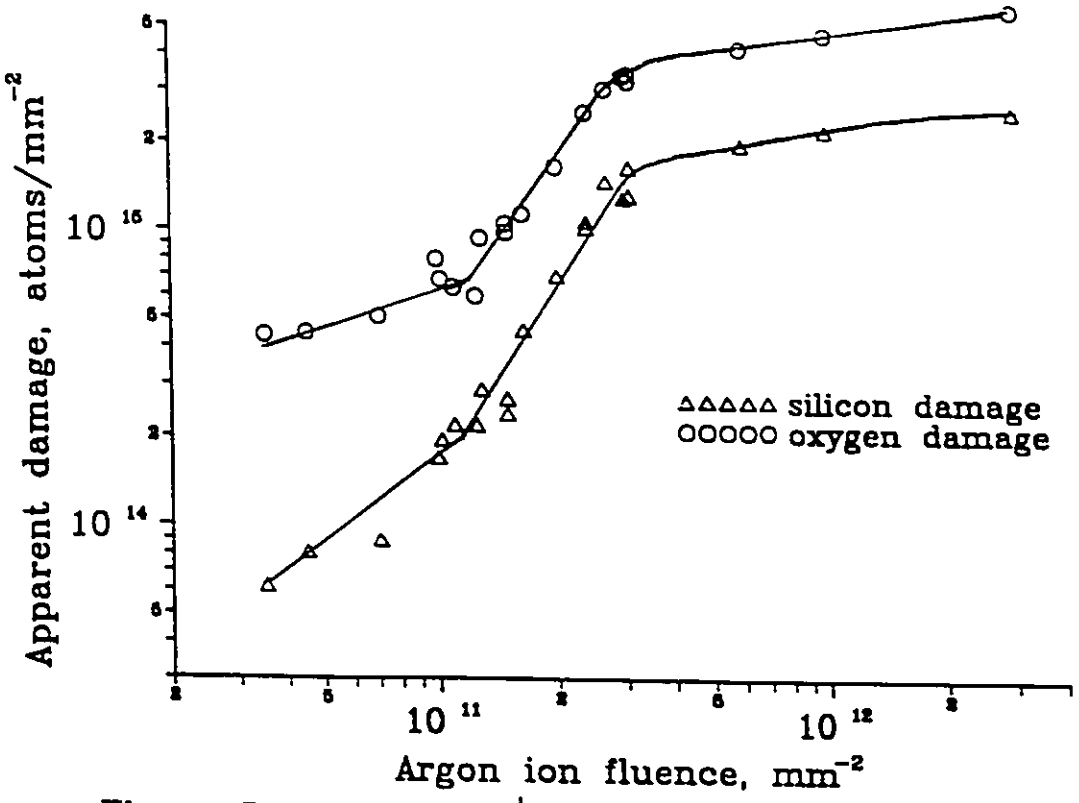

Figure 5.1: 60 keV Ar^+ Damage in Quartz at 50 K

Figure 5.1 shows the buildup of damage with 60 kev Ar^+ ion fluence derived from the spectra in figure 3.6 and from similar spectra, using equation 3.21 and assuming that the damage is in the form of isolated point defects and small amorphous regions. Figures 5.2 and 5.3 show the damage versus fluence (Φ) behaviour of quartz bombarded at low temperature by He, Ne, Ar, Kr, Sb, and Bi ions over the energy range 15 – 200 keV. The results shown in figure 5.2 demonstrate a linear buildup of damage until the onset of saturation, where saturation results from the production of an "RBS-amorphous" layer over the range of the incident ion. In figure 5.3 the damage initially increases linearly with fluence. At intermediate fluences the damage increases roughly as the fluence squared (Φ^2) before tending to saturation at the highest fluences. Note that the damage never completely saturates: it continues to

increase slowly with increasing fluence, presumeably because of the damage created by the deep tail of the ion energy distribution.

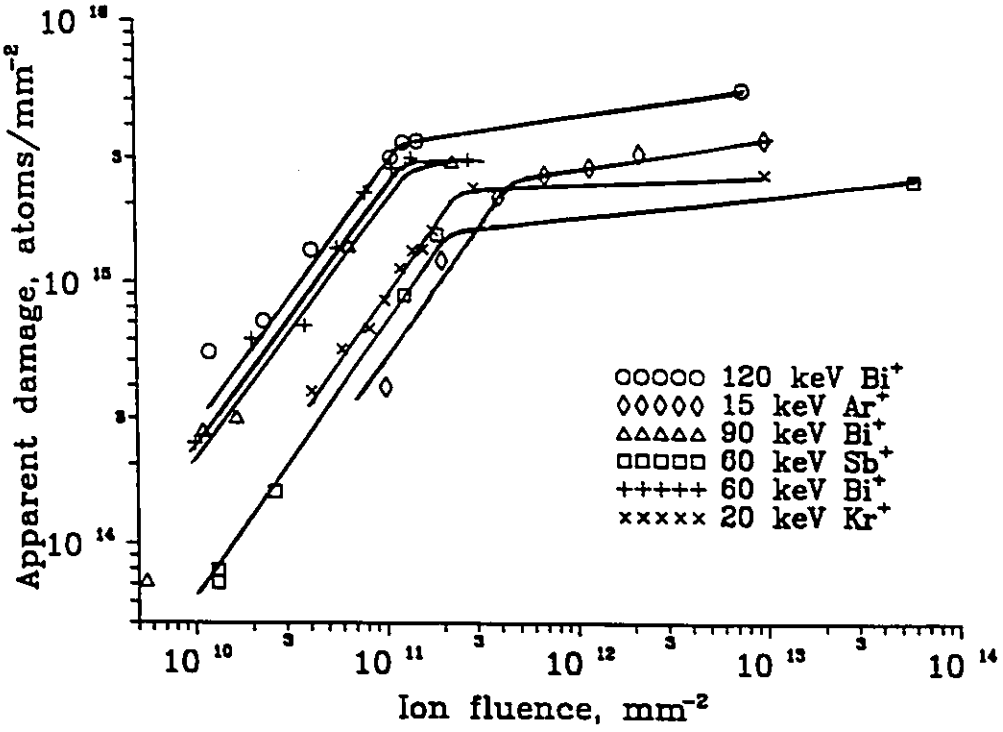

Figure 5.2: Total Damage to Quartz at 50 K by Ions Producing High–Density Cascades

In Table 5.1 the damage–fluence behaviour in the low fluence regime is correlated with the average elastically deposited energy density ($\bar{\theta}_\nu$) and the average defect density ($\bar{F}_D$) in the collision cascade. These quantities are defined as:

$$\bar{\theta}_\nu \approx \frac{0.2\nu(E)\cdot E}{N_v R_v}. \qquad 2.36$$

$$\bar{F}_D \approx \frac{0.2}{N_v R_v}\cdot\left.\frac{dN_D}{d\Phi}\right|_{\Phi\to 0} \qquad 5.01$$

where N_v is the statistical cascade volume obtained using the longitudinal and transverse straggling values derived from Winterbon [1975], $\nu(E)\cdot E$ is the energy deposited

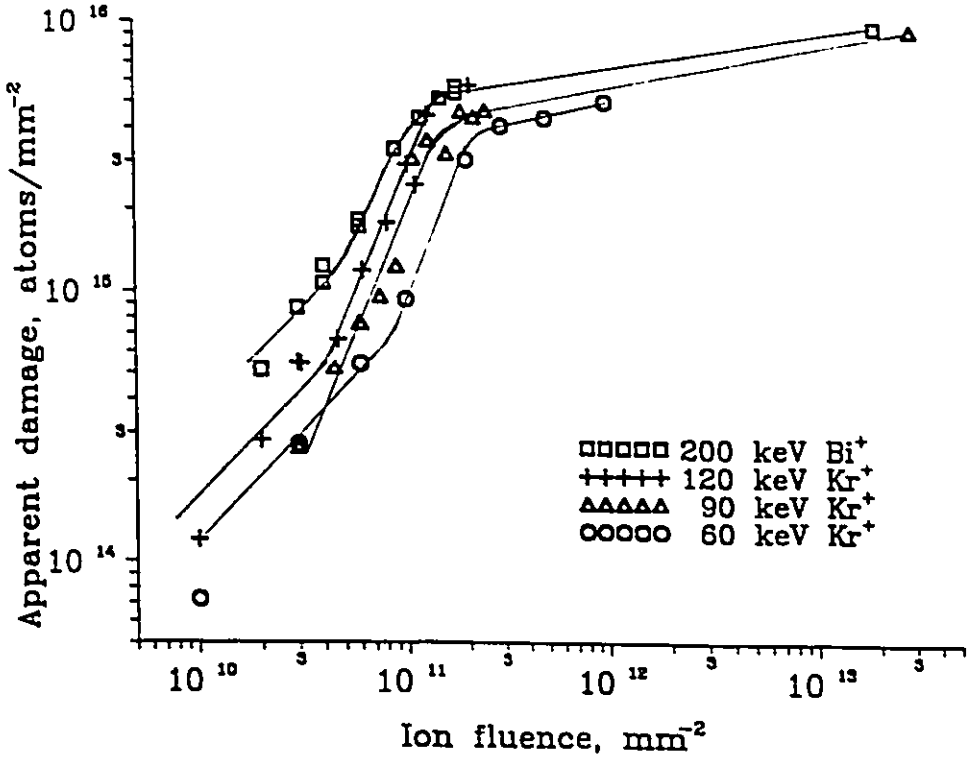

Figure 5.3a: Total Damage to Quartz at 50 K by Heavy Ions Producing Low-Density Cascades

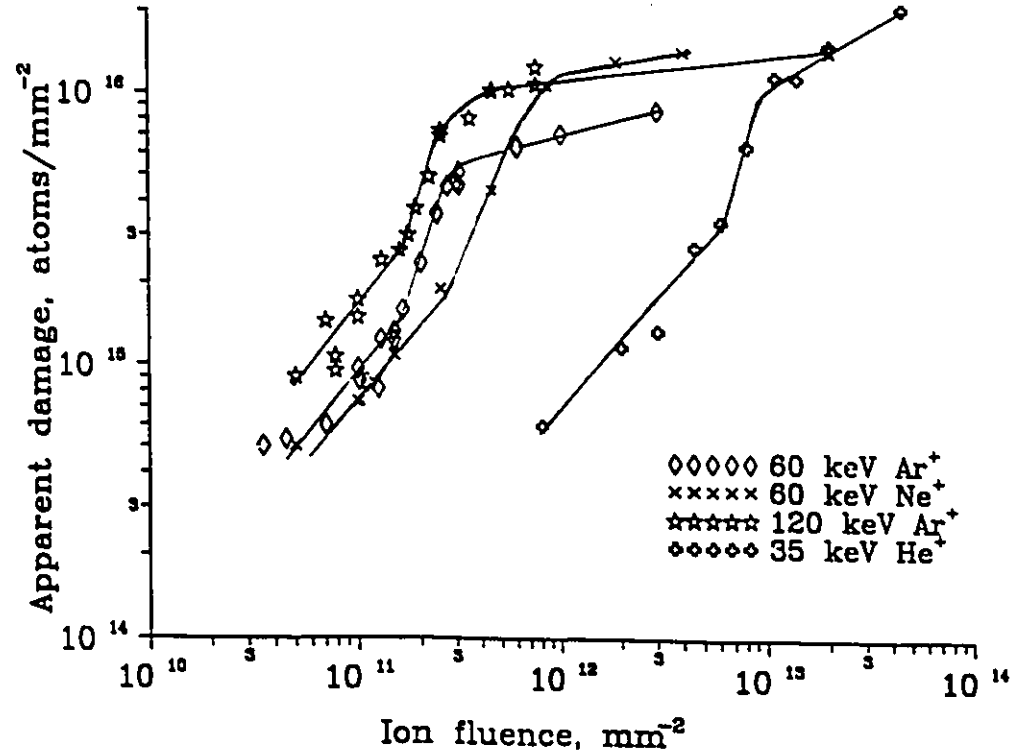

Figure 5.3b: Total Damage to Quartz at 50 K by Light Ions Producing Low-Density Cascades

into elastic collision processes. also derived from Winterbon [1975], and R_v is the approximate ratio between the average individual cascade volume and the statistical cascade volume, derived from Walker [1977], as discussed in section 2.1.

Table 5.1: Low Temperature Damage Data

Ion	*Energy* (keV)	*Reduced Energy* ϵ	$\frac{dN_d}{d\Phi}$(at/ion) Measured	Predicted	*Ratio* $\frac{measured}{predicted}$	$\bar{\theta}_v$ (eV/at)	$\bar{F}_D$ (%)
Kr^+	20	0.0663	8.4×10^3	442	19	0.31	18.8
Bi^+	60	0.0422	23.5×10^3	1307	18	0.25	14.3
Ar^+	15	0.267	4.0×10^3	322	12	0.22	8.8
Bi^+	90	0.0633	28×10^3	1904	14.7	0.13	6.3
Sb^+	60	0.126	21×10^3	1250	17	0.12	7.1
Bi^+	120	0.0844	32×10^3	2458	13	0.09	3.6
Kr^+	60	0.265	9.5×10^3	1213	7.8	0.07	1.5
Bi^{++}	200	0.141	30×10^3	3844	7.8	0.037	0.9
Kr^+	90	0.4	11.4×10^3	1722	6.6	0.035	0.7
Ar^+	60	1.07	8.9×10^3	1080	8.2	0.03	0.7
Kr^+	120	0.53	14.5×10^3	2198	6.6	0.02	0.5
Ne^+	60	3.2	6.9×10^3	872	7.9	0.01	0.3
Ar^+	120	2.14	$\leq 17 \times 10^3$	1853	$\leq$9.2	0.007	0.2
He^+	35	19.0	0.56×10^3	157	3.5	(0.002?)	(0.02)

The data in the lower half of Table 5.1 exhibit a Φ^2–dependent region (see figure 5.3) while those in the upper half show no Φ^2–dependent region (see figure 5.2). It appears then that there is a correlation of $\bar{\theta}_v$ and $\bar{F}_D$ with the presence of a Φ^2 region. The region of Φ^2 behaviour only occurs for the relatively dilute collision cascades, where $\bar{\theta}_v < 0.08$ eV/atom and $\bar{F}_D < 2\%$. Because the number of displaced atoms continues to increase with fluence in the saturation region only a rough estimate of the "saturation level" can be obtained.

Also given in Table 5.1 are the measured and predicted defect production rates, $\frac{dN_D}{d\Phi}$, for each bombardment species. The calculations are for the total damage,

$N_D(Si) + N_D(O)$, expected to be produced, assuming that displacements would occur primarily through elastic collisions, according to equation 2.41. The measured defect production rates are derived from the linear region of damage accumulation, using equations 3.20 and 3.21, assuming that the damage consists solely of isolated point defects and small amorphous regions. Note that the measured damage rates are about 3 – 19 times greater than the predicted damage rates. The displacement energy (E_d) used was a weighted average of 13.3 eV. The results of doing two separate calculations using E_d(Si) = 20 eV and E_d(O) = 10 eV are nearly identical. These values were chosen in section 2.2.6.

Additional information about the damage in quartz can be obtained by comparing the number of displaced oxygen atoms, N_D(O) to that of the silicon atoms, N_D(Si). Figure 5.4 shows the ratio $\frac{N_D(O)}{N_D(Si)}$ plotted against the fluence, Φ, for a sample bombarded with 60 keV Bi^+ at low temperature. This figure was obtained from the ratios of the integrated total numbers of displaced oxygen to displaced silicon atoms It can be seen that the ratio is approximately 5 ± 2 at low fluence but reduces to the stoichiometric damage ratio of 2 at large fluence, as the surface becomes "RBS-amorphous," i.e., as the damage level saturates. Similar results were observed for all the heavy–ion bombardments reported, irrespective of the value of $\bar{F}_D$ or $\bar{\theta}_v$.

In figures 5.5 a,b,c some depth profiles of ion bombardment damage are shown, calculated from the silicon peaks of the RBS spectra. The profiles derived from the oxygen peaks have not been shown, since they exhibit much greater statistical fluctuations. However, by smoothing the oxygen data, profiles were obtained which generally match the silicon profiles. In the cases of figure 5.5a it is seen that the measured damage distribution is somewhat shallower than the calculated deposited energy distribution. This is probably related to the fact that Winterbon [1975] uses

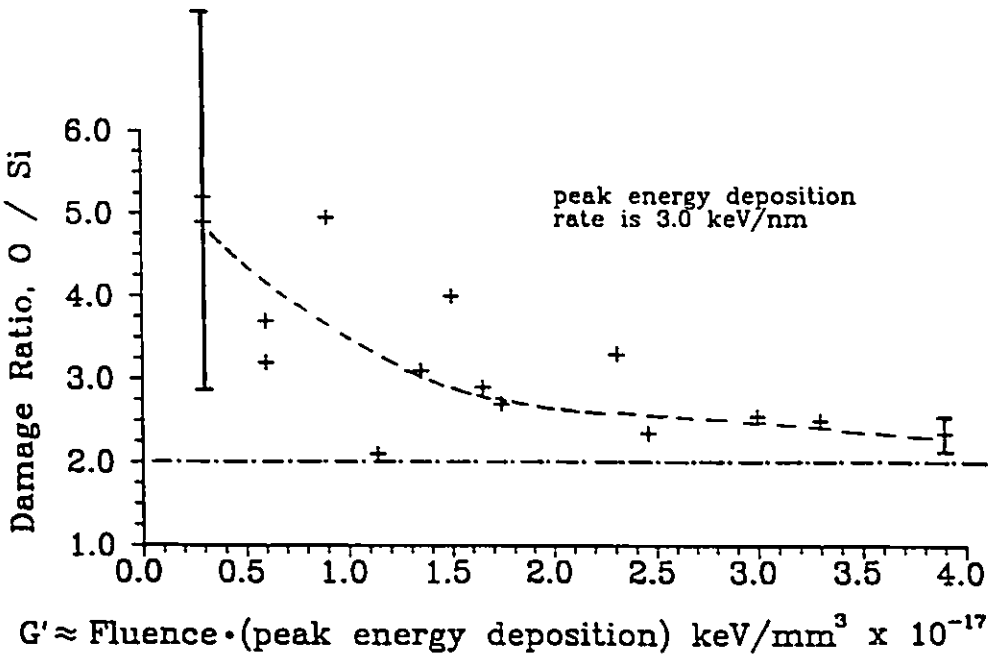

Figure 5.4: Ratio of oxygen to silicon apparent damage as a function of 60 keV Bi^+ fluence at 50 K.

the Lindhard et al. [1963a] values for the electronic stopping power, which have been shown to be underestimates by Thompson et al. [1977a], for low energy $^4He^+$ ions. In figure 5.5(b) the damage profile matches the elastic energy deposition profile very closely, until the damage reaches saturation at the maximum of the profile. Beyond this fluence the damage profile deepens, as the small amounts of damage caused by the tail of the ion energy distribution accumulate. This is also observed in figures 5.5(a), where this process causes the damage to build up between the surface and the peak of the energy deposition profile, as well as beyond the peak. In addition, the analysis beam may have contributed to the formation of the surface damaged region.

It is not clear why the damage profile in figure 5.5(c) is so much deeper than the predicted elastic energy deposition profile. This may be due to a combination of several factors: the intrinsic depth resolution (about 25 nm, or 4 – 6 channels; and

(a) 35 keV He^+

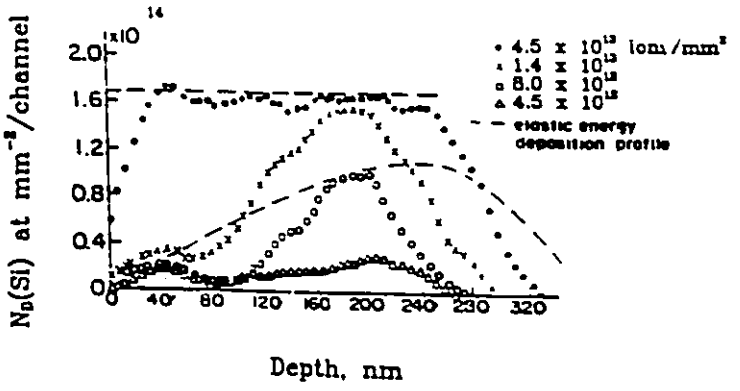

(b) 200 keV Bi^{++}

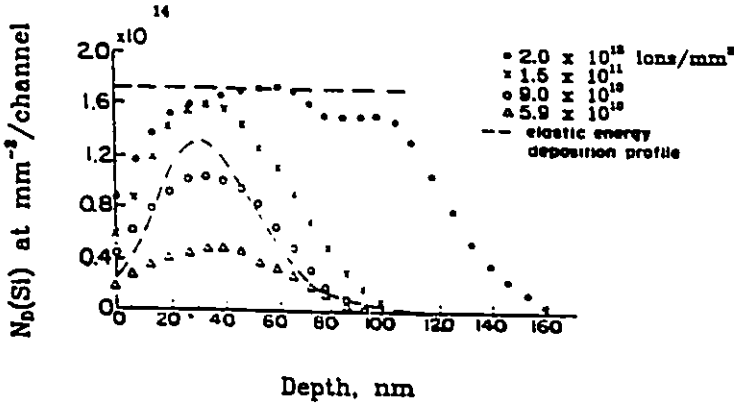

(c) 90 keV Kr^+

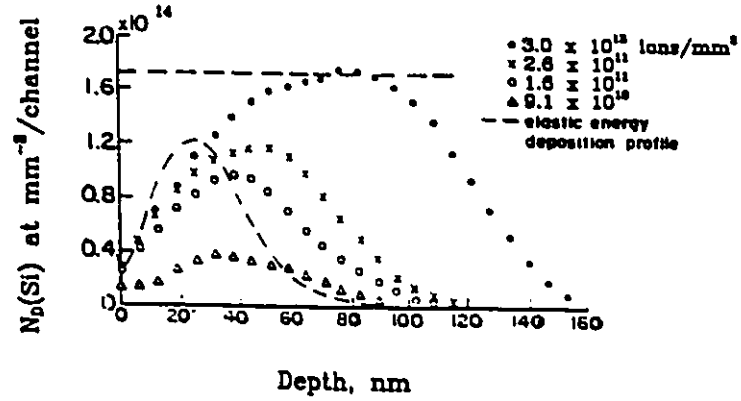

Figure 5.5: Damage/depth profiles in quartz at 50 K

possible surface charging and/or surface roughness, both of which would broaden the damage peak in the RBS/channeling spectra, leading to an apparently deeper damage distribution. Again, as in figures 5.5 (a) and (b), once the damage level at the peak of the distribution nears saturation. the damage profile deepens.

Figures 5.6a and 5.6b show the ratio of oxygen damage to silicon damage

(damage stoichiometry) determined at the peaks of the damage profiles, as a function of G', an accumulated energy density: $G' = \Phi \cdot f_D^{max}$, where f_D^{max} is the predicted peak elastic energy deposition rate, derived from Winterbon [1975], as discussed in section 2.2.5 and shown in figure 2.6. These curves are similar to figure 5.4, but not identical, since figure 5.4 contains data from the entire RBS peaks, plotted against ion fluence, whereas figures 5.6a and 5.6b contain the stoichiometry at the maximum of the damage profiles, plotted against the normalised fluence.

In figure 5.6b it can be seen that an abrupt change in the damage stoichiometry appears at about 1.2 – 1.3×10^{17} keV/mm^3. The transition point corresponds to the ion fluence at which the damage begins to accumulate at a "superlinear" rate (i.e. varies as approximately Φ^2). In contrast, the 200 keV Bi^+ and 90 keV Kr^+ data in figure 5.6a would appear to fit better to a smooth decrease in the damage ratio, more like figure 5.4. f_D^{max} is given in the figures; for comparison, $f_D^{max} \approx 3.0$ keV/nm for 60 keV Bi^+ on quartz. Note that the energy density 1.2 – 1.3×10^{17} keV/mm^3 corresponds to about 1.6 eV/atom, approximately twenty times the transition energy density shown in Table 5.1. This would seem to indicate that the cascade overlap process is very inefficient for reaching the critical damage density for the second stage of damage buildup. In other words, in a single cascade the higher damage rate process appears to be triggered by an elastically deposited energy density of $\geq$ about 0.08 eV/atom, but in damaged regions where the energy density is less than this, the damage cascades must overlap about twenty times before the higher rate process is triggered. Presumeably this is because of the quick annihilation of the majority of the point defects created in such a dilute cascade, similar to the effect seen by Tanimura et al. [1983, 1984] as discussed in section 2.2.7 (isolated, close vacancy/interstitial pairs created by ionization appeared to recombine with a time constant of about 1 ms

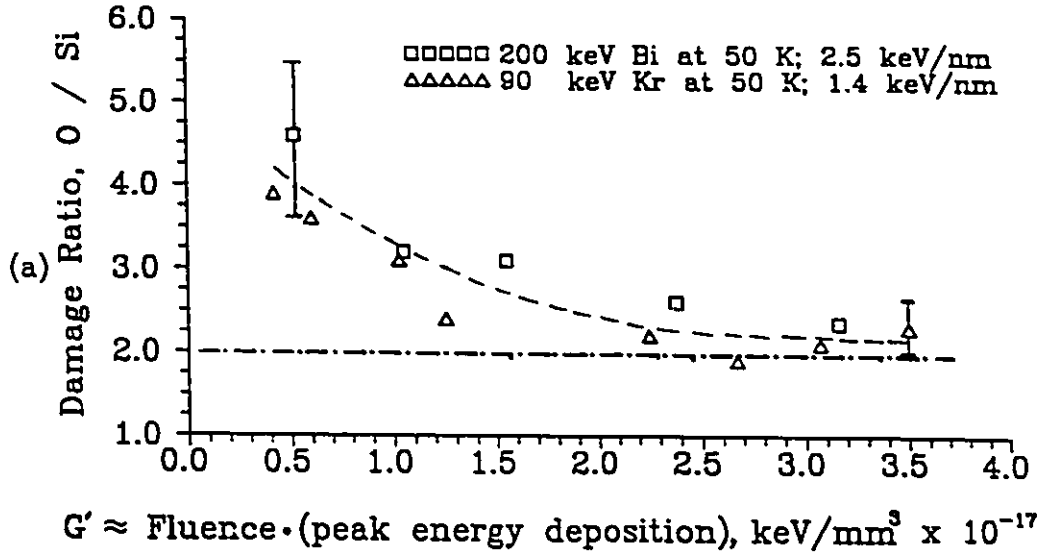

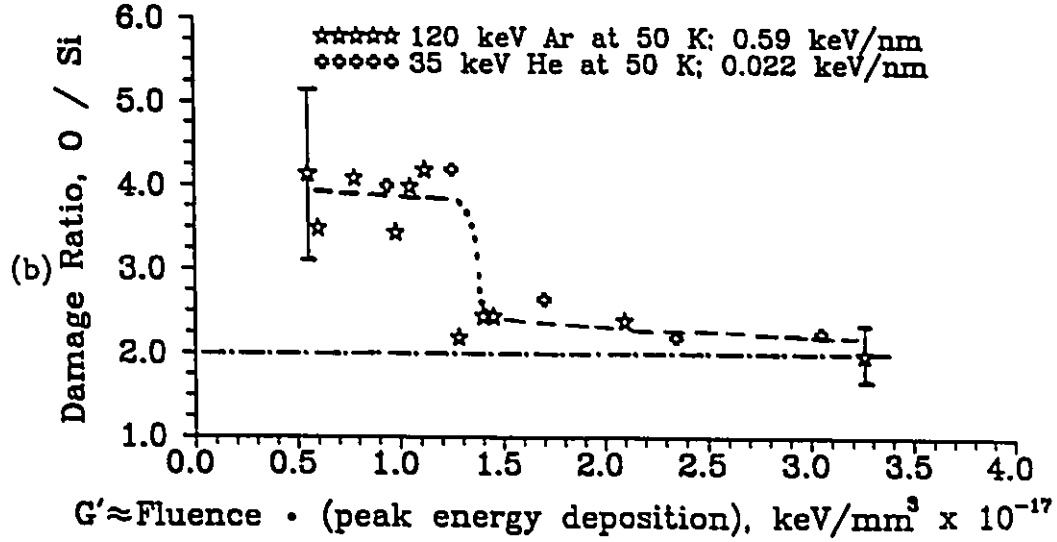

Figure 5.6: Damage stoichiometry at the peak of the damage profile, as a function of the accumulated elastically deposited energy; quartz at 50 K.

at temperatures less than 150 K). An important point here is that the absolute values of these numbers (0.08 eV/atom. and the factor of 20) are fairly arbitrary, depending strongly upon the definition of the size of the cascade. Another way of looking at the above discussion is to take the 1.6 eV/atom energy density as an indicator of the size of the region within which the higher damage rate process occurs. This process might be a thermal spike or lattice relaxation, resulting in an amorphous micro–region, and would dominate the damage buildup in the high–density cascades. The amorphising process might not be as significant in the low density cascades because the volume contained within the 1.6 eV/atom surface is very small, and therefore receives a small fraction of the ion's energy. Table 5.1 shows that the ratio of measured to predicted damage rates decreases as the energy density of the cascade decreases, in agreement with the above discussion. The volume of atoms which receive the critical energy density would increase as the cascades overlapped, resulting in an increasing rate of damage, as actually observed.

The above results were obtained from the peaks of the RBS/channeling spectra. According to Chu et al. [1984], the dechanneling behaviour behind the peaks will also contain some information on the kinds and amounts of damage present. If the damage is composed entirely of point defects and amorphous regions the dechanneling should accumulate linearly with the damage peak area. Figure 5.7 shows a plot of $\Delta\chi$ as a function of fractional damage for the silicon peak, and figure 5.8 shows the same for the oxygen peak; both sets of data are from an experiment in which the quartz was damaged by 90 keV Kr^+ ions at $T < 50$ K. Superimposed are the $\Delta\chi$ values calculated using equations 3.24 – 3.26, assuming that the apparent peak damage is due to point defects and amorphous regions. The reliability of the theoretical values is uncertain, however, since the observed values of $\Delta\chi$ are greater by factors of 1.5 to

3, the presence of strain and/or extended defects may be indicated. The fractional damage is averaged over a depth, X_T, where $X_T = \langle x_D \rangle + 3\langle \Delta x^2 \rangle^{\frac{1}{2}}$.

An experiment to measure the dechannelling induced by ion bombardment at analysing energies of 1.0, 1.4, 1.8 and 2.2 MeV showed no significant energy dependence; looking at figure 3.9, one might conclude that this indicates a mix of strain effects and dechanneling due to point defects and small amorphous regions, with the opposing energy dependencies more or less cancelling each other out.

5.2.2 Comparison of Low Temperature (< 50 K) and Room Temperature Results

Figure 5.9 shows the RBS/channeling spectra for 2 MeV $^4He^+$ analyses of 60 keV Bi^+ incident on quartz at both low and room temperatures. The surface peaks have roughly the same area, but the dechanneling is higher for the room temperature work, as predicted by equations 3.32 – 3.34 and Table 3.2.

Figure 5.10 shows the damage caused by 60 keV Bi^+ at both low and room temperatures. Although the results are not in exact agreement, they are within experimental uncertainty of each other. The uncertainties are largely due to statistical deviations and analysing beam damage, with some contribution from current measurement problems, and from sample preparation. Other experiments were conducted at room temperature (60 keV Kr^+, 60 keV Sb^+), all yielding the same results as at 50 K, within experimental uncertainty. As discussed in section 5.2.4 below, the data of Fischer et al. [1983a] for 35 keV $^4He^+$ damage at room temperature were also in excellent agreement with the results reported here at $T < 50$ K. For this reason it seemed appropriate to concentrate on doing low–temperature experiments, since the

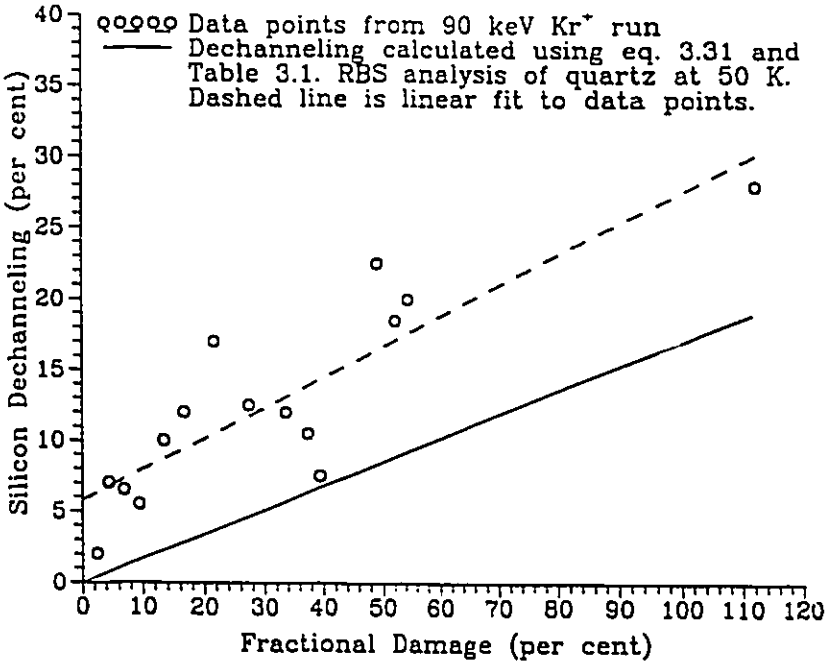

Figure 5.7: Silicon dechanneling as a function of total fractional damage. Fractional damage is the measured damage divided by the number of atoms in one theoretical damage range plus three standard deviatons.

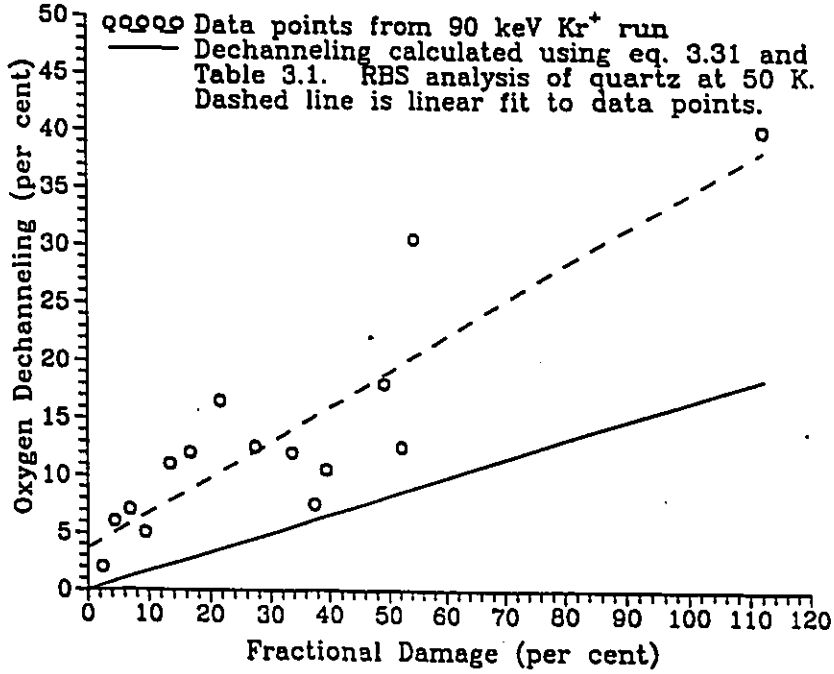

Figure 5.8: Oxygen dechanneling as a function of total fractional damage. Fractional damage is the measured damage divided by the number of atoms in one theoretical damage range plus three standard deviations.

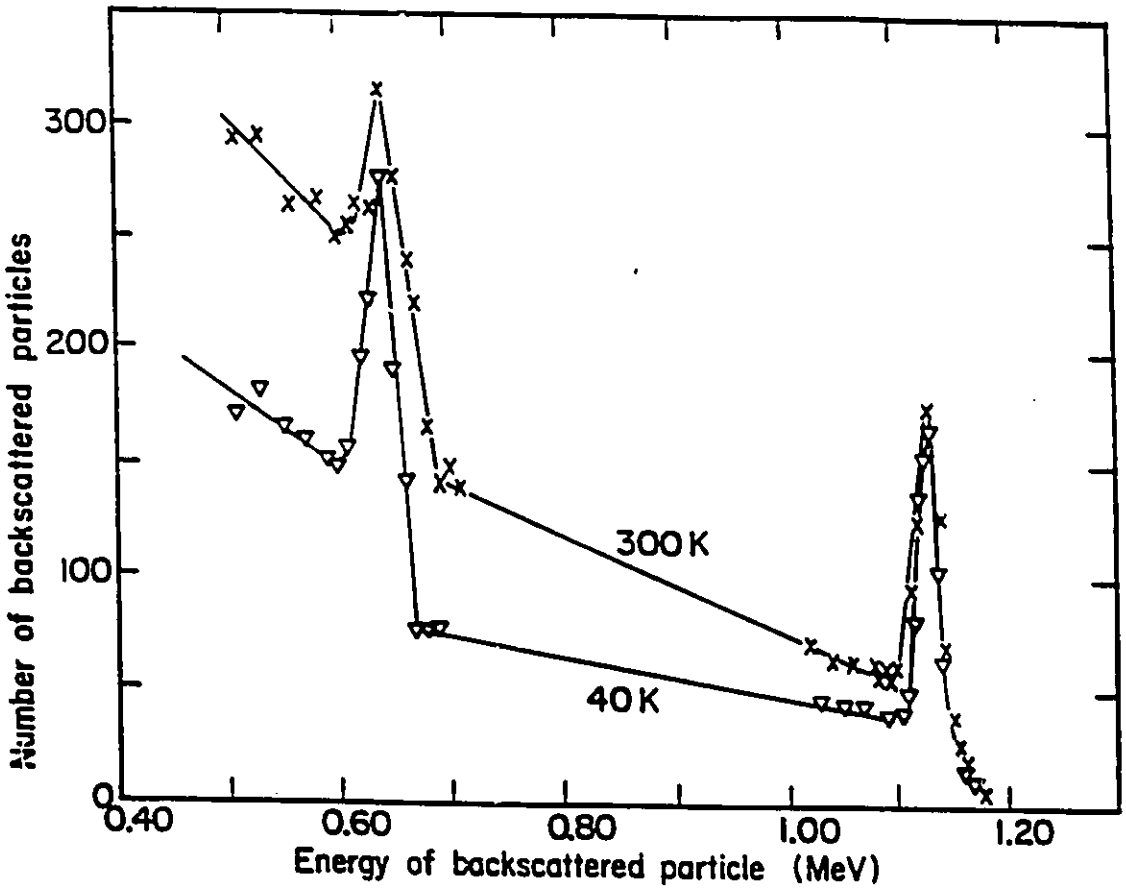

Figure 5.9: Comparison of RBS/channeling spectra for quartz bombarded with 60 keV Bi^+ and analysed with 2 MeV He^+: one sample was bombarded and analysed at 50 K, and the other was bombarded and analysed at 300 K.

lower dechanneling background lowered experimental uncertainties, particularly for the oxygen data.

5.2.3 Effects of Sputtering by Incident Ions

One of the possible influences on the observed stoichiometry is sputtering. In the sputtering process the surface atoms of a solid may be removed by ion bombardment in a number of ways, as discussed in the reviews by Kelly [1978] and Thompson

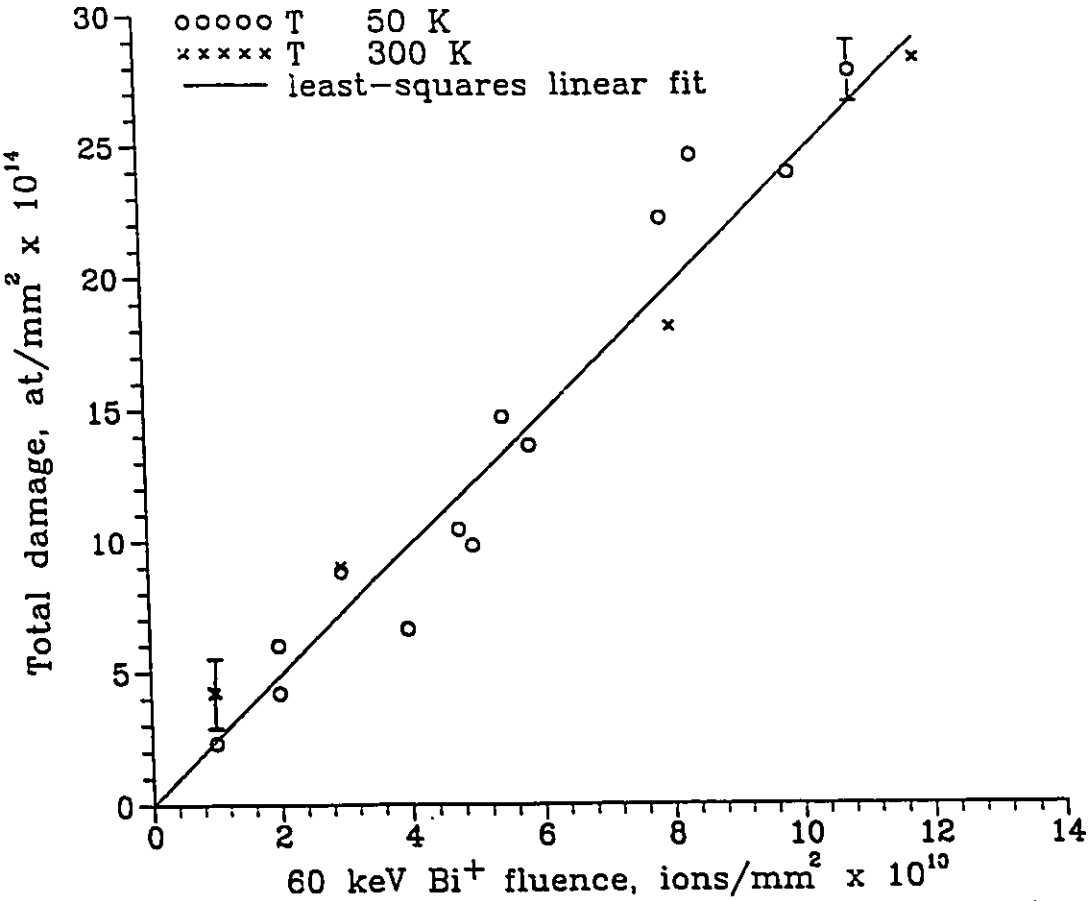

Figure 5.10: Total damage to quartz by 60 keV Bi^+ ions at 50 K (L.T.) and 300 K (R.T.).

[1981]. In a compound material one often finds preferential sputtering, in which one component is sputtered faster than another, resulting in a changed surface stoichiometry. If there is sufficient diffusion of the depleted component from the bulk of the target, the depleted region may extend as deep as hundreds of nanometers into the sample. Preferential sputtering of oxygen has been observed in quartz by Thomas [1974], Carrière and Lang [1974] and Chang [1971], caused by keV electron bombardment. In the measurements displayed in figures 5.1 – 5.6, any significant preferential loss of oxygen would have resulted in a silicon-rich surface, showing up as a reduction

in $N_D(O)$, as a decrease in the surface oxygen–to–silicon damage ratio, and as a slight increase in the silicon random yield near the surface.

To ensure that preferential sputtering was not influencing the data, the sputtering yields of thermally grown SiO_2 thin films were determined under 60 keV Bi^+ ion bombardment. In order to observe the ratio of silicon to oxygen, the films were grown on single–crystal silicon, to a thickness of about 150 nm. (The films were grown in dry air at 1100°C.). Targets were placed in the analysis chamber and carefully aligned so that the <111> axis of the underlying Si crystal was parallel to the analysing beam. Since the amorphous SiO_2 layer scattered the incoming analysis ions, the dechanneling level was increased from about 2% to about 15%. A typical RBS spectrum is shown in figure 5.11a, with the peaks representing the O and Si atoms in the amorphous silica layer. For comparison, the aligned spectrum of a clean single crystal of silicon is shown in figure 5.11b.

The samples were aligned and a spectrum taken, then the samples were bombarded with up to 3×10^{13} ions/mm^2 of 60 keV Bi^+ ions, and the analysis/bombardment process repeated several times, ending with an analysis. It was important that the silica layer be thick enough that the 60 keV Bi^+ ions did not penetrate into the silicon substrate, because they would damage any silicon they reached, adding to the silicon peak. The sputtering yields were determined by calculating the amount of silicon and oxygen indicated by the surface peaks before and after Bi^+ bombardment; the sputtering yield is the change in the number of atoms divided by the ion fluence. Hence, if the silicon peak were increased due to substrate damage, the sputtering yield of the silicon should appear smaller. This was observed in experiments where the SiO_2 film was thin enough for a significant fraction of the bombarding ions to penetrate into the single crystal Si below.

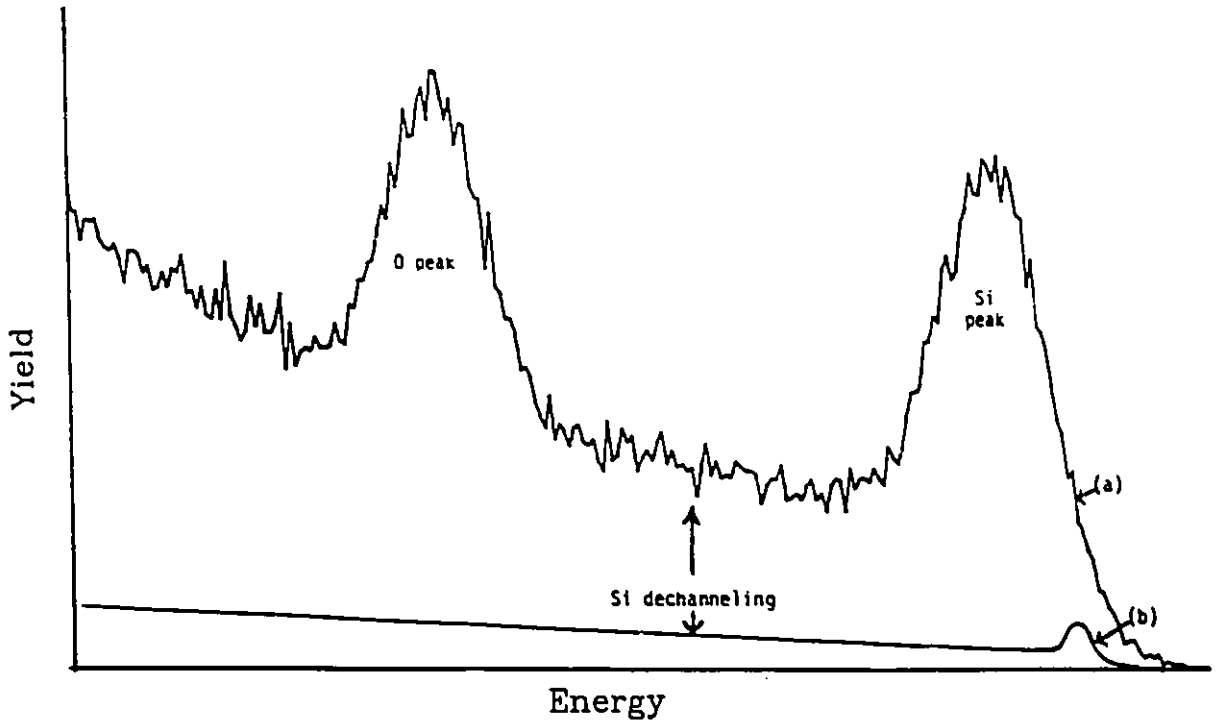

Figure 5.11: Aligned RBS/channeling spectra of: (a) SiO_2 on single crystal Si; and (b) single crystal Si.

Because of the low scattering cross-section of oxygen, the O peak was small, with an integrated peak area of less than nine thousand counts representing 1.15×10^{15} atoms/mm^2. Using a higher fluence of the analysing ions improved this statistic, but caused substrate damage, adding to the error in the Si peak value. The oxygen peak was also superimposed upon a silicon dechanneling background of about 15000 counts. The resulting statistical uncertainty in the oxygen peak was about $\pm$ 250 counts, which corresponded to 3.2×10^{14} atoms/mm^2 of oxygen. For the maximum Bi^+ fluence obtained, 3×10^{13} ions/mm^2, the amount of oxygen removed was only 8.1×10^{14} atoms/mm^2, so the uncertainty in the difference amounted to 40%.

Although the experimental uncertainties were large, it was possible to determine that the sputtering yields were $S(O) \approx 27 \pm 13$ O-atoms/ion, and $S(Si) \approx 7 \pm 3$ Si-atoms/ion. Hence, the oxygen is probably preferentially sputtered, but the yields are so small that this would not significantly influence the RBS/channeling data; e.g. a 60 keV Bi^+ fluence of 10^{11} mm^{-2} is sufficient to totally amorphise quartz to a depth of about 37 nm or $N_D \approx 3\times10^{15}$ atoms/mm^2, whereas only about 3×10^{12} atoms/mm^2 would be removed.

Comparing the observed yields to those calculated in section 2.2.7, it can be seen the sputtering yields are about an order of magnitude greater than predicted by Sigmund [1969]. However, notwithstanding the large experimental uncertainty, they are in the predicted stoichiometry of $\frac{S(O)}{S(Si)} \approx 4$.

5.2.4 Comparison With Other Researchers' Results

Fischer et al. [1983a] bombarded α-quartz crystals with 150 keV Ar^+, 70 keV B^+, and 35 keV He^+ at room temperature, and analysed with 1.4 MeV $^4He^+$ RBS/channeling. Their results are similar to those in figure 5.3, with $\bar{F}_D$ values of less than 2%. They calculated the depth distributions of the silicon damage, and plotted the fractional damage at the peak as a function of ion fluence and accumulated elastically deposited energy (referred to as G' above). Figure 5.12 shows their data for 35 keV He^+ damage at room temperature, superimposed on a similar curve derived from figure 5.5a. The agreement is excellent. Unfortunately, Fischer et al. [1983a] did not report the oxygen damage, or the damage stoichiometry. This is probably because they considered the statistical uncertainties to be so great as to render this data unuseable, due to the large silicon dechanneling background which is present at room temperature.

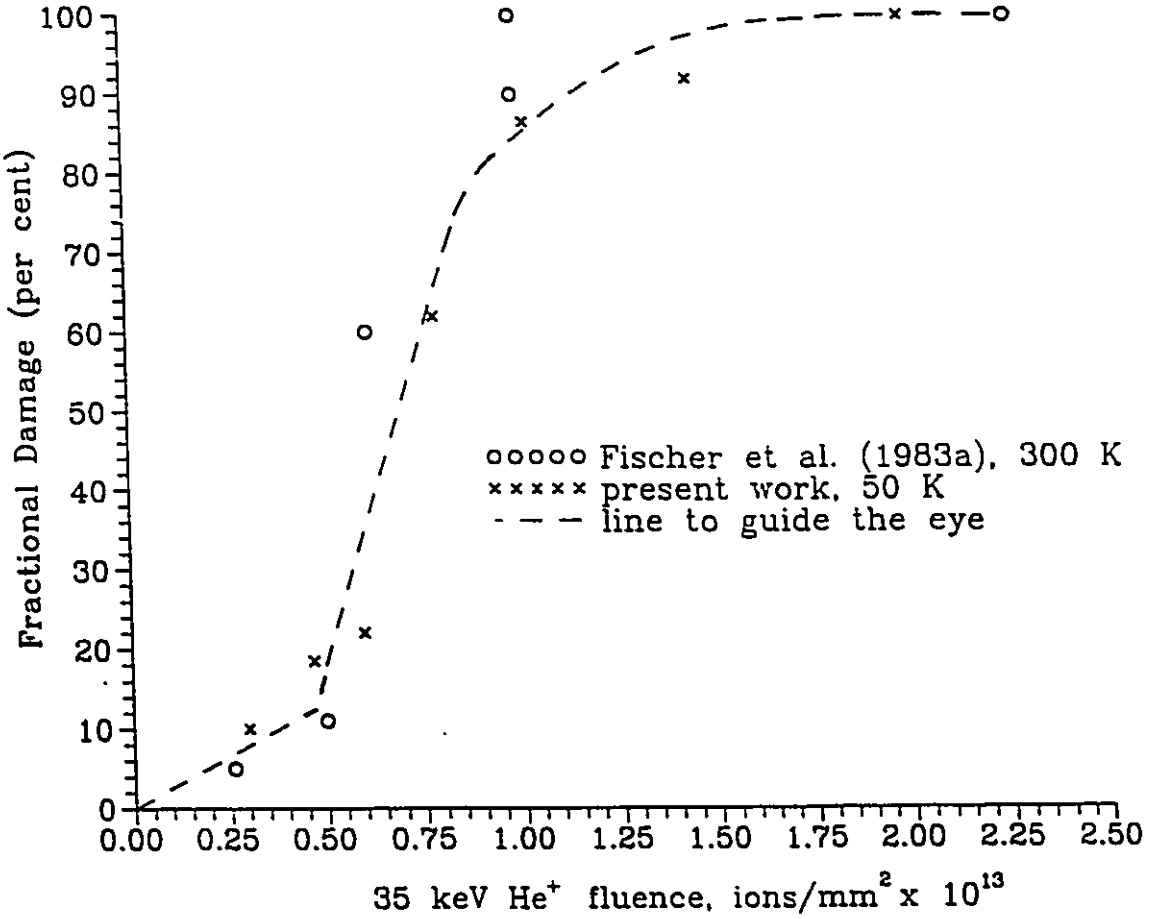

Figure 5.12: Fractional silicon damage at the peak of the damage distribution, from 35 keV He^+ ions on quartz.

Fischer et al. [1983b] continued with annealing studies of the damage created in α–quartz. They observed the change in the RBS/channeling peaks after isochronal anneals: twenty minutes in a dry nitrogen atmosphere. They found that, for low fluences of the light ions which they used, the damage began to anneal at 400 – 700 K, and was completely annealed after an anneal at 770 K. This seemed to be consistent with the idea that this annealing was due to oxygen vacancy migration, since Katenkamp et al. [1980], Nishimura et al. [1974] and Izumi et al. [1977] suggest

that oxygen vacancies become mobile in that temperature range. They interpreted this to imply that the damage consisted mainly of point defects and simple defect structures.

At higher doses, where the accumulated elastically deposited energy density G' (their G_n) was 1×10^{17} to 2.5×10^{17} keV/mm^3, Fischer et al. [1983b] found that annealing was not significant until the temperature was above 800 K, and the damage was not completely annealed until 1170 – 1270 K. They interpreted this to indicate that "amorphous microregions" had formed. Above 2.5×10^{17} keV/mm^3 they found that the damage did not completely anneal even at 1370 K. They believed that this indicated that "quasi–amorphous" layers were formed. Later data [Beez et al., 1983] indicated that this is not the same as "metamict" SiO_2. The most recent work on quartz by a member of this group is that by Götz [1989], in which the damage as measured by RBS/channeling accumulates at rates about 10 times greater than predicted by the modified KP equation. Götz attributes the difference largely to strain about the defects, which resulted in the RBS/channeling measurements exaggerating the damage. Götz also saw increased damage rates at $G' > 10^{17}$ keV/mm^3 and attributed this to the formation of amorphous micro–regions.

Hj. Matzke [1966] irradiated α–quartz and fused silica with 40 keV Xe^+ ions at room temperature, to fluences of 8×10^8 ions/mm^2, 4×10^{11} ions/mm^2 and 2×10^{14} ions/mm^2. He studied the results by the RHEED (Reflection High Energy Electron Diffraction) technique, and by observing the outgassing of the bombarded samples as they were annealed, the latter made possible by implanting radioactive Xe^+ ions. Interestingly enough, he found that the outgassing behaviour of fused silica was the same as that of α–quartz, when bombarded to the intermediate or high dose. The low dose caused no observable damage to the quartz crystal. The intermediate dose was

sufficient to cause the quartz to appear amorphous to RHEED analysis, as would be expected from a comparison with the results in figure 5.2 (e.g. the dose to amorphise quartz using 60 keV Sb^+ would be expected to be similar to the 40 keV Xe^+ dose, since Xe has a similar mass; therefore the surface should be amorphous at $\Phi > 10^{11}$ ions/mm^2).

Primak [1958, 1960, 1964, 1972a, 1972b,1976] has done a considerable amount of work on irradiation effects upon quartz and silica, largely using low energy (but not thermal) neutron irradiation, i.e., neutron energies in the range of 10 eV to 1 MeV. He has shown that the collision cascades which occur about each neutron collision event are similar in their characteristics to those caused by heavy ion irradiation. The results of heavy ion and neutron irradiations showed that the processes of irradiation damage to quartz and silica are complex and highly temperature dependent. It is believed that thermal spikes may play a significant role, especially in the case of medium energy heavy ions and α–recoils.

Primak [1958, 1960, 1964, 1976], Hines et al., [1960], Wittels and Sherrill [1954], EerNisse [1974] and Krefft et al. [1975] measured the damage done to quartz by ions or neutrons using the density changes induced by the damage, or effects dependent upon the density, such as the index of refraction. Beez et al. [1983] indicated that quartz becomes "RBS–amorphous" (i.e., no longer exhibits any channeling behaviour) at ion doses of about $\frac{1}{20}$ of those required to complete "metamictization", as determined by the saturation of changes in the refractive index. Comparing our results with those of Hines et al. [1960], we find the same general trend, although the dose ratios vary from $\frac{1}{4}$ to $\frac{1}{40}$, possibly due to large experimental uncertainties in the work of Hines et al. [1960], as noted by Primak [1964].

EerNisse [1974] proposed a quantitative model for the density changes and strain caused by irradiation damage, using three fitted parameters. The model is based on two kinds of damage: that induced by energy deposited elastically and that induced by energy deposited inelastically. He noted that other researchers, e.g., Revesz [1973], do not distinguish between the two kinds of damage. EerNisse observed a dose rate dependence for ionization (inelastic) induced damage, but not for elastic collision induced damage.

Krefft et al. [1975] compared sapphire crystals (Al_2O_3) with quartz. They observed that quartz damages faster than sapphire. Furthermore, sapphire and quartz both expand due to the effects of elastically deposited energy, but sapphire contracts when subjected to inelastically deposited energy, whereas quartz expands. Krefft et al. [1975] believe that this contraction is due to ionization-induced annealing of radiation damage. They conclude that the sapphire anneals because its bonds are more than 50% ionic. This agrees with Naguib and Kelly's [1975] results.

5.3 MeV $^4He^+$ Ion Damage – Observations and Calculations

5.3.1 MeV $^4He^+$ Damage on Previously Undamaged Crystals

Figure 5.13 shows typical RBS/channeling spectra of quartz damaged by 2 MeV $^4He^+$ ions. The rate of damage by MeV $^4He^+$ was the same at low temperature and at room temperature, within experimental uncertainty.

Figure 5.14 shows the buildup of damage in the near-surface region of quartz as it was analysed repeatedly on the same spot, at low temperature. The quartz crystal was aligned for the entire fluence. The number of displaced silicon atoms

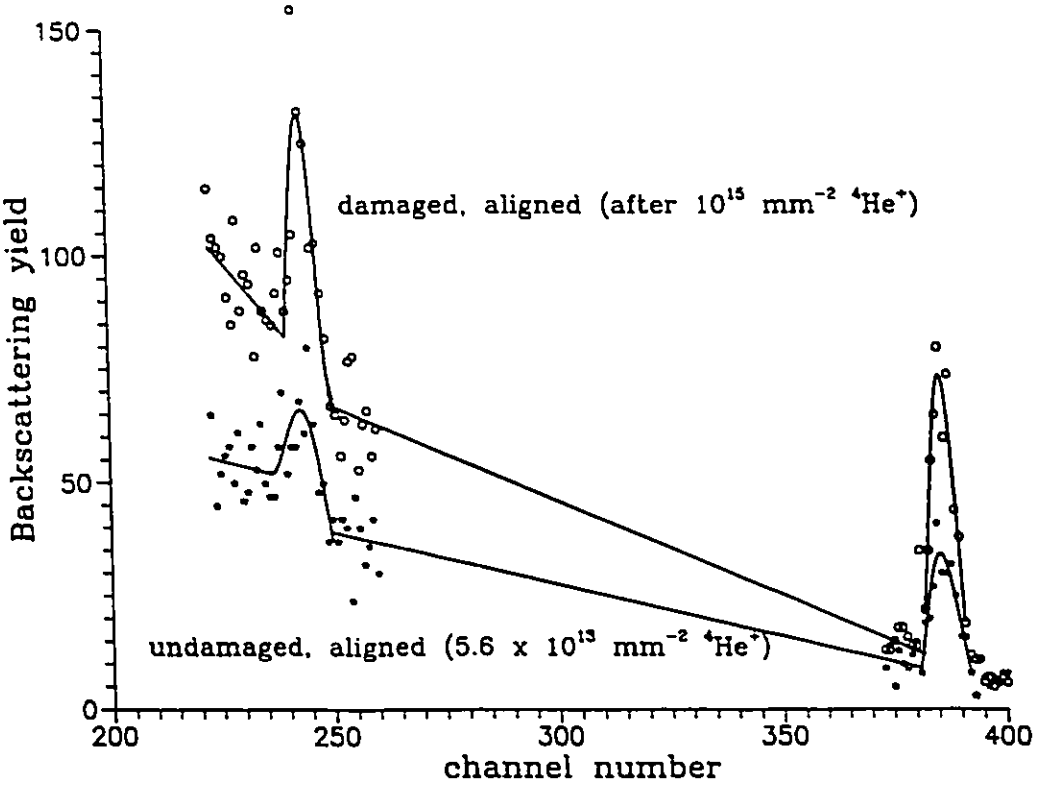

Figure 5.13: Typical RBS/channeling spectra for 2 MeV ^{4}He$^+$ damage analysis in quartz at 50 K. Lines are drawn to guide the eye.

accumulated linearly with the fluence, at a rate of 1.2 atoms/ion ± 0.3, until approximately 8×10^{14} ions/mm^2, after which the slope of the curve decreased. The initial slope of figure 5.14 yields a damage cross-section of $\approx 10^{-14}$ mm^2, nearly two hundred times the theoretical value of 6×10^{-17} mm^2, calculated using the modified Kinchin-Pease formula, equation 2.41, and assuming that the majority of the damage is created by elastic collisions (see section 2.2.6).

5.3.2 MeV ^{4}He$^+$ Damage in Previously Damaged Crystals

Since figure 5.14 indicated that the MeV ^{4}He$^+$ analysis ions did not create a great deal of damage on a previously undamaged crystal, it was thought to be

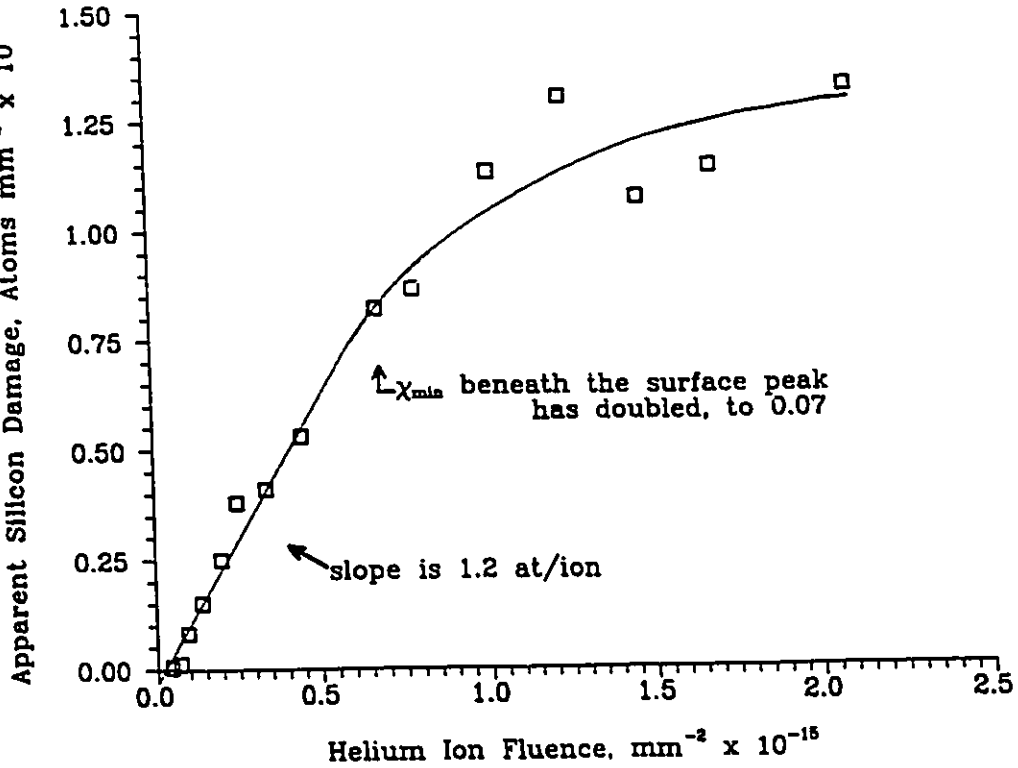

Figure 5.14: 2 MeV $^4He^+$ damage to quartz at 50 K, calculated using the change in the surface peak area, as in eq. 3.20, 3.21.

safe to improve the counting statistics by increasing the $^1He^+$ ion fluences up to about 1.5×10^{14} ions/mm^2 per analysis, on damaged crystals. However, when the $^4He^+$ beam fluence was reduced to about 0.3×10^{14}/mm^2, the total damage was considerably lower than that observed using higher fluence analyses. In figure 5.15 the buildup of total damage [i.e. $N_D(O) + N_D(Si)$] in quartz bombarded with 60 keV Sb^+ at low temperature is seen to be non–linear when high fluence analyses were used. When the lower fluence analyses were used, the damage was linear with Sb^+ fluence. This

clearly demonstrates how strongly the channeling measurement itself may influence the results. Hence, all subsequent measurements of heavy–ion–induced damage were obtained using the minimum $^4He^+$ fluence possible while still achieving reasonable statistics. This generally leads to increased uncertainties for the $N_D(O)$ data.

Using the data shown in figure 5.15, and other data from the same experiment, it was possible to determine the Si and O damage due to $^4He^+$ bombardment (channeled) as a function of the damage present due to the Sb^+ bombardment plus the previous $^4He^+$ analyses. In these calculations the linear damage accumulation at low $^4He^+$ ion fluences was assumed to be indicative of $(\frac{dN_D}{d\Phi})_{Sb}$; then the $^4He^+$ damage rate at measurement point i would be

$$\left(\frac{dN_D}{d\Phi}\right)_{He} \approx \frac{N_D(i) - N_D(i-1) - \left(\frac{dN_D}{d\Phi}_{Sb}\right)\left(\Phi_{Sb}(i) - \Phi_{Sb}(i-1)\right)}{\Phi_{He}(i) - \Phi_{He}(i-1)} \qquad 5.02$$

Here, $N_D(i)$ and $N_D(i-1)$ are taken from the data with the greater $^4He^+$ fluences, i.e. the upper curve in figure 5.15. The results are shown in figure 5.16, with the damage rate $(\frac{dN_D}{d\Phi})_{He}$ assigned to the damage level $\frac{N_D(i)+N_D(i-1)}{2}$. It can be seen that the rate of damage production initially increases with the amount of damage present. Then as the surface layer approaches complete "RBS–amorphousness", the incremental $^4He^+$ damage decreases, as would be expected.

In other experiments quartz samples were pre–damaged to various levels by heavy–ion bombardment at low temperature (50 K). These were then subjected to MeV $^4He^+$ bombardment in both the aligned and random directions, and the increase in the Si and O peaks in the channeled backscattering spectra determined. The results,shown in figure 5.17, indicated that the rate of increase in damage, $(\frac{dN_D}{d\Phi})_{He}$, is unchanged by the alignment of the crystal. This suggests that the dominant damage production process for MeV $^4He^+$ is via electronic energy deposition.

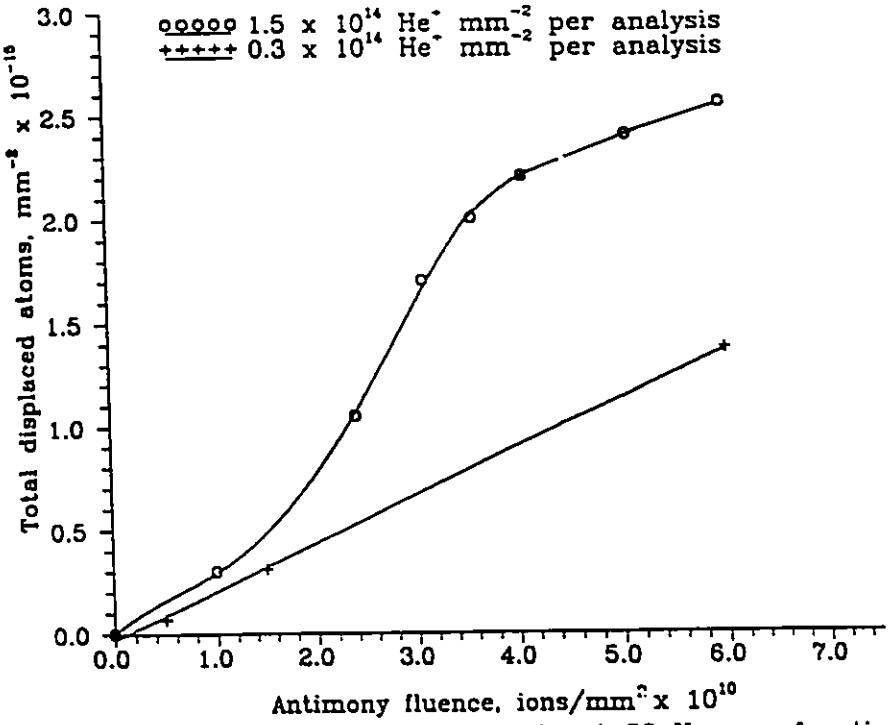

Figure 5.15: Damage levels in quartz at 50 K, as a function of 60 keV Sb^+ fluence and 2 MeV He^+ analysis fluence.

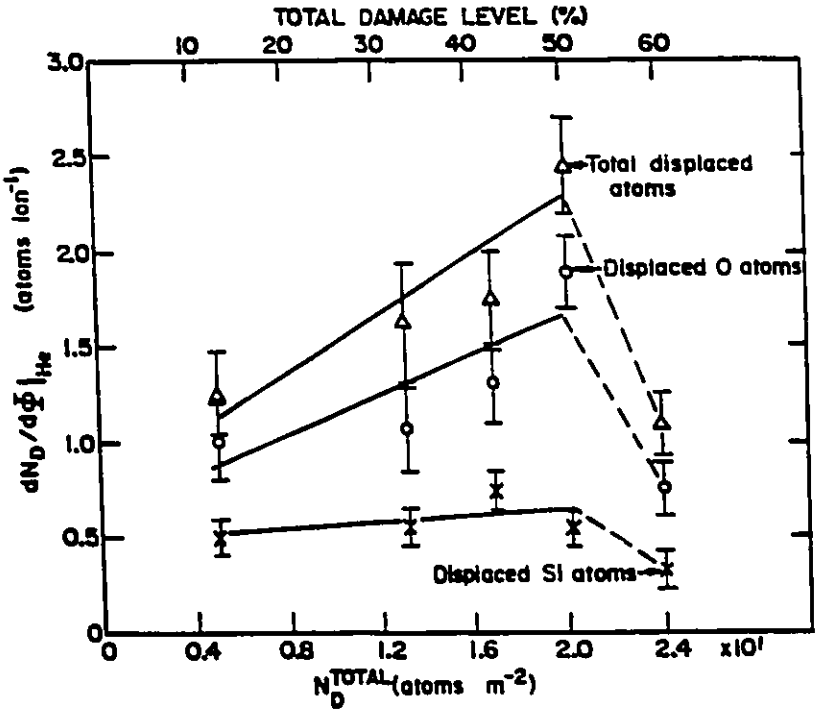

Figure 5.16: Rate of damage to quartz at 50 K by 2 MeV He^+ ions, as a function of the total damage produced by 60 keV Sb^+ ions and previous He^+ analyses.

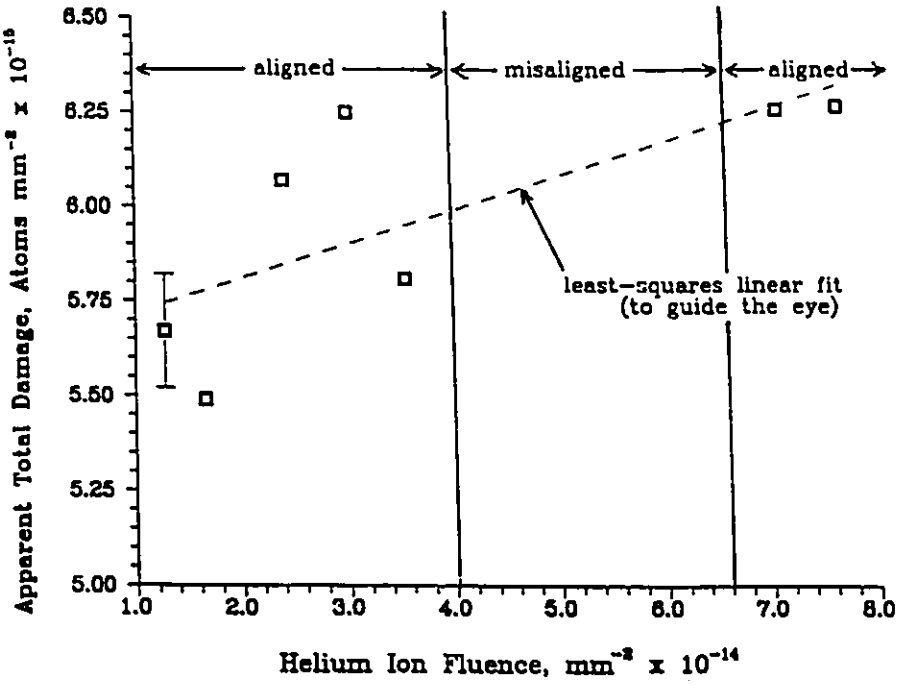

Figure 5.17: Total damage to quartz at 50 K by 2 MeV $^4He^+$ ions, with crystal aligned and misaligned; pre-damage by 2.5 x 10^{14} mm^{-2} 60 keV Ar^+ ions. Sample error bar represents statistical uncertainty.

Within experimental uncertainties, the MeV $^4He^+$ ions produced greater than stoichiometric damage, i.e. the $^4He^+$ ions displaced 2 - 4 oxygen atoms for every silicon atom displaced. However, the experimental uncertainties were quite large, because the $^4He^+$ damage, while significant, was usually mixed with as much or more damage due to heavier ions.

In an experiment to determine whether there was annealing at temperatures between 40 K and 300 K, quartz samples were bombarded with 60 keV Ar^+ and Bi^+ ions to fluences such that approximately 20% of the atoms in the surface 50 nm were displaced from their lattice positions. Under these conditions, the effects of cascade

overlap were considered to be insignificant. Fifteen minute anneals were carried out at approximately 80 K, 110 K, 180 K and 300 K with subsequent re–analysis always at approximately 40 K.

The results indicated a steady increase in the damage level for both ion species. Because of this unexpected result, a sample was bombarded at approximately 40 K with Bi^+ to nearly the same fluence as used in the "anneal" experiment and was subsequently subjected to an identical series of $^4He^+$ particle analysis steps without carrying out the thermal steps. The results of this experiment along with the data obtained in the "anneal" experiments are given in Table 5.2 and figure 5.18. There is no significant annealing of the ion–beam damage between 50 K and 300 K indicated by RBS/channeling analysis.

Table 5.2: Rates of Damage by 2 MeV $^4He^+$ After 60 keV Bi^+ Damage

Φ_{Bi} ions/mm^2	Damage Present %	Damage Rate atoms/ion
2.0 x 10^{10}	20%	3.4 ± 0.2
4.5 x 10^{10}	24%	7.1 ± 0.2
5.0 x 10^{10}	29%	4.8 ± 0.6
5.5 x 10^{10}	47%	4.4 ± 1.2
8.5 x 10^{10}	75%	1.5 ± 0.4

The data in figure 5.18, $\frac{dN_D}{d\Phi}$ follows the same general trend seen in figure 5.16, i.e., the initial and final rates of damage by the analysis beam are lower than at intermediate damage levels. Note that the peak of the $^4He^+$ damage rate occurs at about 24% of the saturation level for the 60 keV Bi^+ experiments and at about 50% in the 60 keV Sb^+ experiments; this difference may be due to the higher density of damage in the Bi^+ cascades, the "anneal" steps in the Bi^+ experiments, or some combination of both.

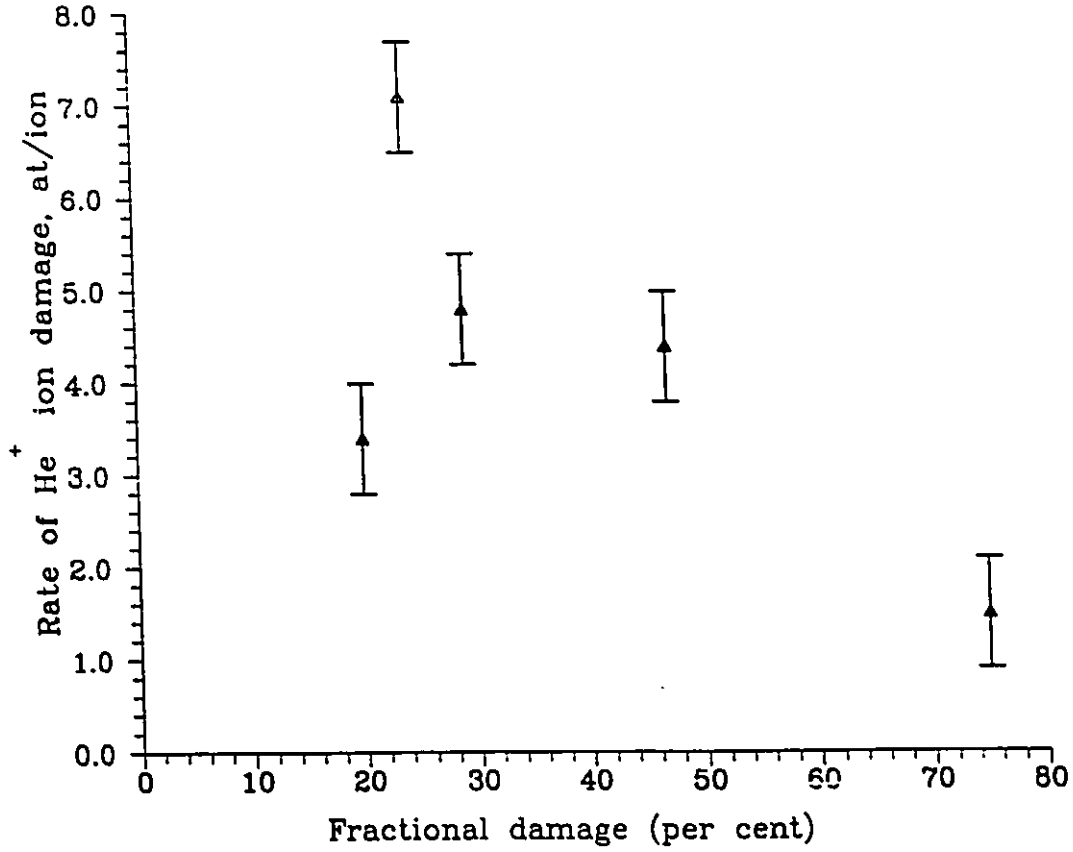

Figure 5.18: Rate of damage to quartz at 50 K by 2 MeV He^+ ions, as a function of the total damage produced by 60 keV Bi^+ ions and previous He^+ analyses. Error bars represent statistical uncertainties only.

The damage caused by the analysis beam introduced considerable uncertainty into the calculations of damage produced by the heavy ions. The sensitivity of the MeV $^4He^+$ damage to surface conditions was such that it was not possible to clearly separate the effects of the analysis beam from that of the heavy ions. Hence, it was decided to minimize the analysis beam fluence per analysis, at the cost of increasing statistical errors.

5.3.3 Comparison with Other Researchers' Results

Fischer et al. [1983a] reported that no measureable damage was produced by 1.4 MeV $^4He^+$ bombardment of previously undamaged quartz at room temperature, in contrast to the results reported in section 5.3.1 (1 – 2 atoms/ion). This is probably due to the difference in interpretative techniques; Fischer et al. [1983a] calculated depth profiles of the damage, assuming no damage beneath the surface peak, whereas the results reported in section 5.3.1 were based on the total area of the surface peak and on the dechanneling level behind it. Fischer et al.'s [1983a] technique would be insensitive to low–level damage. They did observe that the rate of damage by MeV $^4He^+$ ions increases when the quartz crystal is pre–damaged (see figure 5.19).

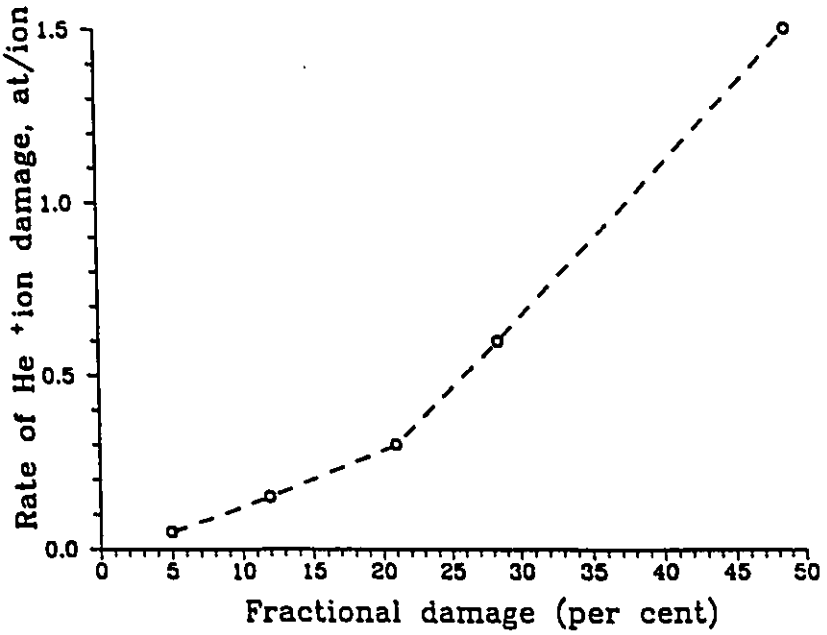

Figure 5.19: Rate of damage by 1.4 MeV $^4He^+$ as a function of the local fractional damage level, in quartz at 300 K. From Fischer et al. (1983a).

Both Hobbs and Pascucci [1980] and Das and Mitchell [1974] created and observed elctron–beam damage in quartz using the electron microscope. Hobbs and Pascucci's [1980] experiments led them to postulate a two–step radiolysis model. i.e., model for ionization damage. The first step is the "heterogeneous nucleation and growth of disordered strain centers involving migration of point defects. The second is a gradual homogeneous crystalline — amorphous transformation of the remaining matrix" [Hobbs and Pascucci 1980]. Figure 5.20 shows that the two groups had very different ideas as to what constituted amorphous quartz: the electron doses required to reach the amorphous state differ by about a factor of five.

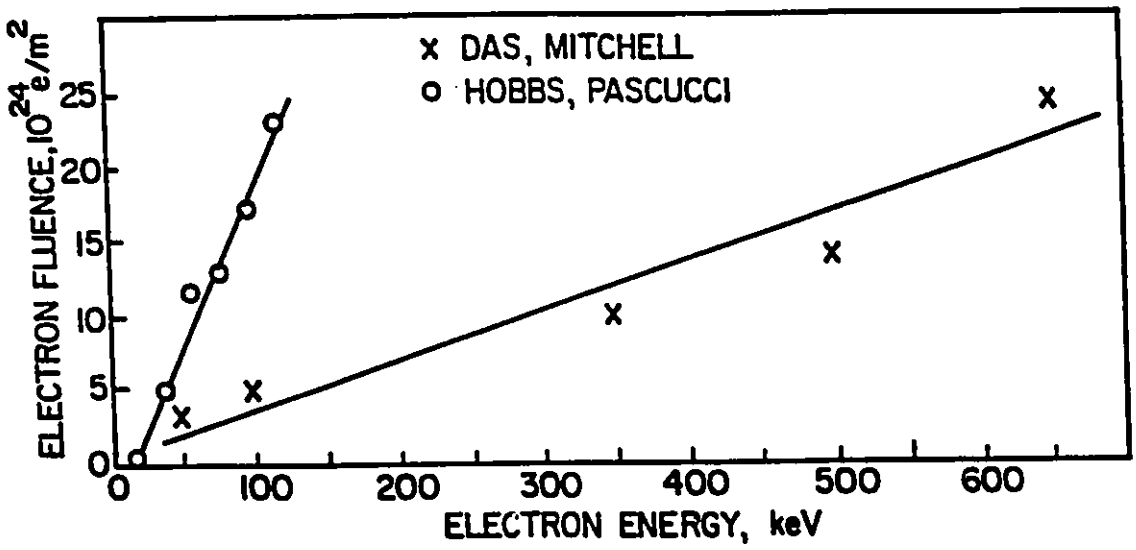

Figure 5.20: Electron fluences required to amorphise quartz at 300 K. For more data, see Table 6.1.

Fischer et al. [1983b] did RBS/channeling and annealing studies showing that

the damage created by MeV $^4He^+$ beams does not anneal even at 1170 K. They postulated that the $^4He^+$ ions create mostly broken Si–O bonds, most of which, in an undamaged crystal, would re–form. However, in a crystal with a high level of damage, and therefore a distorted structure, new bonds may form (i.e., Si–Si, or Si–O–O–Si bonds), making the local disorder permanent.

CHAPTER VI: INTERPRETATION AND DISCUSSION

6.1 Introduction

In this chapter an attempt is made to interpret the observations reported in chapter V, in the context of the previous chapters. Section 6.2 summarizes the results from chapter V; section 6.3 relates these results to various models of radiation damage which were summarized in chapter II; section 6.4 discusses the perturbations of the data due to the main analysis technique, RBS/channeling; section 6.5 describes some possible "synergistic" effects; and section 6.6 introduces a semi-empirical model which produces an approximate fit to the observations.

6.2 Summary of Results

A) Heavy ion damage appears to build up linearly with fluence at low damage levels, at rates 3 to 19 times greater than predicted by simple elastic collision theory (equation 2.41). The damage rate is higher for higher energy density ion cascades.

B) If the average density of elastically deposited energy, $\bar{\theta}_\nu$, is greater than approximately 0.08 eV/atom in a collision cascade, then the damage continues to build up at a constant rate until the damage level reaches approximately 70% of the saturation level, X_T. X_T was found to be the number of atoms in the depth of quartz corresponding to one damage range, $\langle x \rangle_D$, plus 3 standard deviations, $\langle \Delta x^2 \rangle_D^{\frac{1}{2}}$, as calculated using Winterbon [1975]. RBS/channeling results indicated that the ions with $\bar{\theta}_\nu \approx 0.08$ eV produced an average damage level of approximately 2% to 3% within a collision cascade.

C) If the density of elastically deposited energy is less than approximately 0.08 eV/atom in a collision cascade. then at the point when the deposited energy density

has accumulated to approximately 1.6 eV/atom, the rate of damage increases, such that the damage appears to increase as the square of the dose, until it begins to saturate, at roughly 70% damage. For want of a better name, this is called the "superlinear," or "Φ^2" region.

D) Damage continues to build up deeper than the range of the incident ions, after the quartz has apparently been amorphized to a depth corresponding to the ion range.

E) The damage is initially non-stoichiometric, i.e., the apparent number of displaced oxygen atoms is much more than twice that of displaced silicon atoms, until the damage approaches saturation. This applies equally to both high energy-density and low energy-density cascades.

F) The dechanneling levels are greater than predicted, and greater than those observed by Abel et al. [1969, 1972].

G) Sputtering is an insignificant effect in these experiments.

H) The MeV $^4He^+$ analysis ions create damage at a rate which is sensitive to the amount of damage already present, and is not sensitive to the alignment of the quartz crystal. This analysis damage cannot be subtracted from the total damage in any simple fashion.

6.3 Models of Radiation Damage Related to Observations In Quartz Crystals

6.3.1 Modified Kinchin–Pease Equation: Simple Elastic Displacement Theory

In section 2.2.6 the simple elastic displacement theory was discussed. The theory predicts that the number of displacements created by an ion will be proportional to the elastically deposited energy, and inversely proportional to the displacement energy, as in equation 2.41:

$$N_{KP}(E) \approx \frac{0.42\nu(E)}{E_d} \qquad 2.41$$

where $N_{KP}(E) = (\frac{dN_D}{d\Phi})_{KP}$. This equation applies in the simplest case, a low–density cascade where only individual point defects are created and other effects are negligible. For the example of 35 keV $^4He^+$ ions on quartz, ν(E) is found to be 4.97 keV from interpolations of Winterbon's [1975] data. There are many estimates of E_d in the literature ranging from 5 eV to 100 eV. There does seem to be general agreement that the Si–O bond energy is about 5 eV [Hobbs and Pascucci, 1980] in quartz, so for minimum values, one could use: $E_d(O) \approx 2 \times 5\text{eV} = 10\text{eV}$, and $E_d(Si) \approx 4 \times 5\text{eV} = 20\text{eV}$.

This is because there are two Si–O bonds on each oxygen atom, and four on each silicon atom. These values assume that the only energy required to create the displacements is that required to break the bonds, and therefore are clearly underestimates. Due to the open structure of quartz, this may not be a large error, especially for oxygen atoms, which are located around the large c–axis channels.

The predicted result, for 35 keV $^4He^+$, is that $\frac{dN_D}{d\Phi}(O) \approx 139$ atoms/ion, and $\frac{dN_D}{d\Phi}(Si) \approx 35$ atoms/ion, assuming an equipartition of the elastic energy, i.e., two–thirds of the energy displaces oxygen atoms, and one–third displaces silicon atoms.

Then the total is $\frac{dN_D}{d\Phi} \approx 174$ atoms/ion. A similar way of calculating $\frac{dN_D}{d\Phi}$ is to assume an average displacement energy:

$$E_d(average) = \frac{E_d(Si) + 2 \cdot E_d(O)}{3} = 13.3eV$$

This yields $\frac{dN_D}{d\Phi} \approx 157$ atoms/ion, 10% smaller than the previous estimate. By comparison, the displacement rate observed by RBS/channeling is $\frac{dN_D}{d\Phi} \approx 555$ atoms/ion, over three times the calculated rate.

6.3.2 Simple Cascade–Overlap Effects

In order for cascade–overlap to have an effect, some defects from the first cascade must persist until the second cascade arrives. At typical current densities of 10^9 ions/mm^{2}s, with an ion cascade cross–section of $\approx$ (10 nm)^2 = 10^{-10} mm^2, the time between overlaps is $\frac{1s}{10^9 \cdot 10^{-10}} = 10s$. Of course, this varies by several orders of magnitude, depending on the ion, its energy and the current density. However, compared to the cascade duration itself, $\approx 10^{-12}$s, this is a very long time. In a dilute cascade in an undamaged crystal, most of the close vacancy/interstitial pairs created will recombine by the time the next cascade arrives.

There are two simple effects of cascade–overlap: in factor (a), atoms which have previously been displaced are moved again, thereby lowering the observed damage rate: if the crystal is 2% damaged, as a first approximation the damage rate, $\frac{dN_D}{d\Phi}$, is reduced by 2%; in factor (b), atoms neighbouring vacancies have a reduced E_d, because there are fewer bonds holding them in place, thereby increasing $\frac{dN_D}{d\Phi}$. Lattice relaxation (strain) around vacancies, interstitials and other defects will generally act to reduce the displacement energy still further.

In a diatomic crystal such as quartz, these two effects have a complex interaction. As shown in Appendix II, factors (a) and (b) cancel each other out at

low damage levels, so that there would be no effect on $\frac{dN_D}{d\Phi}$ or on $\frac{N_D(O)}{N_D(Si)}$ until $N_D(O)$ reached a value such that there would be a significant chance of an atom being displaced when nearby damage has created enough strain to reduce the effective bonding energy significantly, causing the damage rate to increase. This might occur at an average damage level as low as approximately 2 – 10% in a dilute cascade, and probably would always occur within dense cascades.

The above discussion shows that a simplistic interpretation of cascade–overlap effects might explain the shape of the N_D vs Φ curves for the low density cascade experiments, where $\bar{\theta}_\nu < 0.08$ eV/atom. In the case of the higher density cascades, it might be that the third stage, "RBS–amorphousness" occurs locally, in the densest part of the individual collision cascades.

6.3.3 Models of Amorphisation by Relaxation of a Heavily Damaged Lattice

The damage vs dose curves for quartz shown in figure 5.3 (the low–density cascades) were very similar to those for Si [Thompson et al., 1980] and GaAs [Stevanovic et al., 1983]. The increase in the rate of damage build–up appears to be attributable to the lattice relaxation model discussed in section 2.4. Figure 5.6b, showing the damage stoichiometry as a function of accumulated energy density, also lends support to this model. It can be interpretated as showing a transition point at $G' \approx 1.2 - 1.3 \times 10^{17}$ keV/mm^3, or about 1.6 eV/atom; this corresponds to the ion dose at which the damage begins to accumulate at a "superlinear" rate, i.e., $N_D \propto \Phi^2$. At higher doses the lattice might relax into an amorphous state, causing the damage rate to increase sharply while reducing the damage stoichiometry, as was observed. The transition is not as clear for the heavier ion damage (stoichiometry plotted in

figure 5.6a), because these ions have sufficiently high elastic energy deposition rates at the low energy ends of the cascades that local amorphisation might occur without need of cascade overlap. The amorphous region would only comprise a fraction of the total apparent damage, but would result in an enhanced damage rate and a closer–to–stoichiometric damage ratio.

There are some difficulties with the comparison to Si, however. First, the ratio of observed–to–calculated damage rates is much larger for quartz than for Si. In the high density cascades ($\bar{F}_D > 3\%$) the ratio is 12 – 19 for quartz but only about 8 for Si; in the low density cascades the ratio is 3 – 8 for quartz but only 1 – 3 for Si. Hence, even for low density collision cascades the quartz results indicate a damage level much larger than predicted by equation 2.41, whereas the agreement with theory is quite good for some light ions incident on Si.

Second, as seen in figure 5.4, the high non–stoichiometry is evident even when the energy density criterion would indicate that local amorphisation occurs within every cascade region. The damage versus dose curve for 60 keV Bi^+ (figure 5.2) shows no clear "superlinear" region, nor does figure 5.4 show a sharp transition in the damage stoichiometry. If lattice relaxation is responsible for the greatly enhanced rates of damage, then the vast majority of the damage should be stoichiometric, from the first ion impact up to damage saturation.

Third, since quartz is an insulator, the effect of ionization could be quite significant; in the semiconductor studies, the samples were usually doped enough to make them fairly good conductors, with the result that ionization damage was not observed.

6.4 Perturbations Due to RBS/Channelling Analysis

6.4.1 Damage by MeV $^4He^+$ Ions

As related in section 5.3, the MeV $^4He^+$ analysis ions created significant damage in both the very near-surface region and the deeper regions where the heavier ions created damage, more so in samples which were previously damaged. The apparent rate of damage by the analysis ions is about two orders of magnitude greater than could be expected from simple elastic collision displacements.

In the range of energies which were available for RBS/channeling analysis, the elastic and inelastic stopping powers of $^4He^+$ in quartz both decrease with increasing energy. Therefore it was not possible to clearly determine whether the analysis ions were producing damage predominantly by elastic or by inelastic energy deposition by simply varying the analysis beam energy. However, the experiment in which it was shown that the damage rate was approximately the same whether or not the ions were channeled (see section 5.3.2, and figure 5.18) can be taken as a good indicator that the damage is predominantly due to inelastic energy deposition. The elastic collision probability for MeV $^4He^+$ ions is very sensitive to the crystal alignment, and therefore so is the elastic energy deposition rate. In the experiment, since $\chi_{min} < 10\%$, there should be a reduction in the elastic energy deposition rate of a factor of ten. In contrast, Abel et al. [1969,1972] concluded that the reduction in the inelastic stopping power is less than 20%. Note that Townsend [1990] and Toulemonde et al. [1990] believe that ionization damage by MeV $^4He^+$ ions is insignificant. Townsend measured the changes in refractive index which are not noticeable until there is significantly more damage than would be required to be measureable by RBS/channeling [Beez et al., 1983]. Toulemonde et al. concluded that ionization damage dominated for

heavier ions but not for $^4He^+$, although the reasons for this exception are not clear from their paper. They report aligned versus non-aligned damage measurements for the heavier ions as proof that ionization damage dominates, but did not report such measurements for $^4He^+$ ions. It should be emphasized that the present work does not indicate that MeV $^4He^+$ ionization damage is more efficient than elastic collision damage, but indicates quite the opposite. However, because the ionization energy deposition rate is so much greater than the elastic energy deposition rate, ionization damage does dominate, at least in the surface 200 nm measured in these experiments.

Hobbs et al. [1980] have reported that the rate of damage by keV electrons increases with increasing electronic stopping power, confirming the idea that damage can be produced by inelastic energy deposition. The efficiency for damage production in quartz by inelastic energy deposition, in terms of atoms displaced/keV, has been quoted as between 10^{-3} and 5×10^{-3} times that due to elastic energy deposition [Fischer et al., 1983; Norris et al., 1974; and Howitt et al., 1983]. For 2 MeV $^4He^+$ in quartz the electronic stopping power is a factor of about 2000 times larger than the elastic stopping power. Hence it would be expected that the inelastic energy deposition would still be the dominant damage production mechanism from MeV $^4He^+$ bombardment.

From the data of Pages et al. [1972] it was possible to estimate the stopping power of 100 keV electrons in quartz as approximately 0.12 eV/10^{13} atoms·mm^{-2} as compared to about 40 eV/10^{13} atoms·mm^{-2} for 2 MeV $^4He^+$ in quartz, derived from the data of Chu et al. [1978]. The fluence of 100 keV electrons needed to amorphise quartz was reported by Hobbs et al. [1980] and by Das et al. [1974], and is shown in figure 5.20; the dose of 2 MeV $^4He^+$ required to reach "RBS-amorphousness" is approximately 2×10^{15} ions·mm^{-2}. These doses can be compared by calculating the

deposited inelastic energy density, $G_I' = \left(\frac{dE}{dx}\right)_e \cdot \Phi$. The values are given in Table 6.1, below. The efficiency of damage creation by $^4He^+$ ions roughly the same as that of 100 keV electrons, despite the factor of over 300 in the ratio of the stopping powers. The differences in G_I' in Table 6.1 may be largely due to differences in the definitions of amorphousness in quartz. It seems reasonable to conclude that the inelastically-induced damage rate is only weakly dependent on $\bar{\theta}_\eta$, the inelastic energy deposition density, except insofar as $\bar{\epsilon}_\eta$ is related to other paramaters, primarily $\bar{\theta}_\nu$.

Table 6.1: Inelastic Damage Parameters in Quartz

Particle	Energy keV	$\left(\frac{dE}{dx}\right)_e$ eV/10^{13}mm^{-2}	$\Phi_{amorphous}$ mm^{-2}	G_I' keV/mm^3
electron[1]	100	0.12	1.8 x 10^{18}	1.7 x 10^{21}
electron[2]	100	0.12	3.5 x 10^{17}	3.4 x 10^{20}
$^4He^+$[3]	2000	40	2.0 x 10^{15}	6.4 x 10^{20}

[1] Hobbs et al., 1980

[2] Das, et al., 1974

[3] present work

The main difficulty with the $^4He^+$ damage is that it is not simply additive; subtracting a constant times the $^4He^+$ fluence does not give consistent results. Furthermore, it would appear that the values of $\left(\frac{dN_D}{d\Phi}\right)_{He}$ for a given set of conditions (i.e., ion, energy, fluence, temperature) varied broadly: this is largely due to statistical uncertainties, but probably there is a significant contribution from sample preparation since strain effects seem to be important.

6.4.2 Strain Effects

In section 3.5 Quéré's [1976] comments on the interpretation of channeling data were noted. He said that the surface peak area was not always a good indicator of the number of atoms "displaced", i.e., all bonds broken and the atom removed from its lattice site. This is because channeling will detect atoms nudged more than ~ 20 pm from their crystalline position by local strain. In a low–Z, open structure like quartz, where flux peaking probably makes a very small contribution, the strain factor may be quite important. From the quartz structure diagrams in figures 3.10 and 3.11 one can see that there is more open space and a lower potential near oxygen atoms than near silicon atoms; furthermore, the oxygen atoms have two bonds, whereas the silicon atoms have four. These factors should make it easier for local strain to shift oxygen atoms from their proper lattice sites by the small amounts needed to make them appear to RBS/channeling as if they were displaced atoms, in the sense of Frenkel defects. Hence strain effects should be expected to exaggerate the non-stoichiometry of the observed damage levels.

Sample preparation and surface conditions could contribute as well. The preparation technique of mechanically thinning the crystals can produce significant strain, as was evidenced by the slight but visible curl of a crystal which had been thinned just a bit too far.

If the surface was perfectly clean, and the analysis chamber's liquid nitrogen trap was cold, there would occasionally be bursts of noise in the detector, presumeably caused by sparking. It seems quite likely that there would have been some low–level sparking much of the time during data collection, contributing small amounts of noise, which would increase the apparent dechanneling level. A variation of this noise

from sample to sample may be responsible for some of the experimental uncertainty, especially if the sparks caused surface damage and/or strain.

6.5 Synergistic Effects

From the above discussions, it seems clear that the damage observed is created in a complex manner, and that the analysis technique contributes significantly to this complexity. It seems highly unlikely that the strain alone is responsible for the large differences between the damage observed and that expected. More likely, synergistic effects are present. For example, the rate of damage by MeV $^4He^+$ is about thirty times higher in the near-surface region (to a depth of $\sim 30 - 50$ nm) of the crystals than below this surface region. There are several possible contributing factors: (a) there is a higher probability of an elastic collision in the surface peak region, and the presence of elastically created defects will stabilize some inelastically created defects; (b) there is more water in the surface 20 nm of quartz [Alfred et al., 1978], up to one water molecule for every four SiO_2, and the water creates local strain which might stabilize inelastically created defects; and (c) the closer to the surface that an oxygen interstitial is created, the greater the chance of it migrating to the surface to be released. Thus, the rate of damage by the analysis beam, which is primarily by inelastic energy deposition, is dependent upon local strain, the defect concentration and the impurity concentration.

The same synergism probably applies to the heavy-ion collision cascades: the damage and strain created by elastic collisions would act to stabilize inelastically created defects.

6.6 A Semi-Empirical Model of Ion–Beam Damage in Quartz

A number of attempts were made to computer-model the RBS/channeling data reported above. The model which had the greatest success is a semi-empirical model which averages the damage level over the depth X_T. The model calculates the damage in five steps at each ion fluence, assuming that the effects are simply additive over small increments of the fluence, $\Delta\Phi^i$:

1) simple elastic collision damage, as in equation 2.41;

2) analysis beam damage;

3a) lattice relaxation in the most highly damaged core of a cascade, resulting in the production of amorphous micro–regions;

3b) lattice relaxation due to multiple overlap of the lesser–damaged regions surrounding the cascade cores, again producing amorphous micro-regions; and

4) strain effects.

Thus, for each ion dose, the computer adds the damage due to simple elastic collisions, then the increase due to analysis–ion damage, and then the increase due to the two relaxation effects; this damage level is then used to estimate the damage level observed, with the effects of strain included. Damage is calculated separately for each sub-lattice. The best fits were obtained when the effects of steps 2 and 4 were made proportional to the total damage level, $N_D(\mathrm{O}) + N_D(\mathrm{Si})$. The equations for these steps are:

$$\text{Step 1:} \qquad \Delta N_D^i(\mathrm{Si})_E = \Delta\Phi^i \cdot \frac{1}{3} \cdot \frac{0.42\nu(E)E}{E_d(\mathrm{Si})} \cdot \mathrm{Rem}^i(\mathrm{Si}) \tag{6.01}$$

$$\text{where:} \qquad \mathrm{Rem}^i(\mathrm{Si}) = \frac{\frac{X_T}{3} - N_D^{i-1}(\mathrm{Si})}{\frac{X_T}{3}} \tag{6.02}$$

$$\text{and:} \qquad \Delta N_D^i(\mathrm{O})_E = \Delta\Phi^i \cdot \frac{2}{3} \cdot \frac{0.42\nu(E)E}{E_d(\mathrm{O})} \cdot \mathrm{Rem}^i(\mathrm{O}) \tag{6.03}$$

$$\text{where:} \qquad \text{Rem}^i(\text{O}) = \frac{\frac{2}{3}X_T - N_D^{i-1}(\text{O})}{\frac{2}{3}X_T} \qquad 6.04.$$

Here. $\Delta\Phi^i$ is the i^{th} ion fluence step, and Rem is the fraction of atoms not yet displaced. X_T has been converted from nm to atoms/mm^2 by multiplying by N. It is assumed, as a first approximation, that no damage occurs beyond X_T, which will result in the model under–estimating the damage at very high fluences. At this point the program adds ΔN_D^i to N_D^i, and goes on to the next step, analysis beam damage:

$$\text{Step 2:} \qquad \Delta N_D^i(\text{Si})_{\text{He}} = \Delta\Phi_{\text{He}}^i \cdot \sigma_{\text{He}} \cdot N_D^i(\text{tot}) \cdot \text{Rem}^i(\text{Si}) \qquad 6.05$$

$$\text{and:} \qquad \Delta N_D^i(\text{O})_{\text{He}} = 1.5\Delta\Phi_{\text{He}}^i \cdot \sigma_{\text{He}} \cdot N_D^i(\text{tot}) \cdot \text{Rem}^i(\text{O}) \qquad 6.06$$

where $\Delta\Phi_{\text{He}}^i$ is the i^{th} analysis beam fluence step, $N_D^i(\text{tot}) = N_D^i(\text{Si}) + N_D^i(\text{O})$, and σ_{He} is the initial cross–section for damage–creation by the analysis ions, determined by roughly fitting this model to the data in figure 5.14. Following the results given in section 5.3.2, σ_{He} was assumed to be 50 % greater for oxygen atoms than for silicon atoms. Again, at this point the program adds ΔN_D^i to N_D^i, and goes on to the next step. relaxation within the cascade core:

$$\text{Step 3a:} \qquad \Delta N_D^i(\text{Si})_{\text{core}} = \frac{1}{3}R_{\text{core}} \cdot \Delta\Phi^i \cdot V_c \cdot R_v \cdot \bar{\theta}_\nu \cdot \text{Rem}^i(\text{Si})^2 \qquad 6.07$$

$$\text{and:} \qquad \Delta N_D^i(\text{O})_{\text{core}} = \frac{2}{3}R_{\text{core}} \cdot \Delta\Phi^i \cdot V_c \cdot R_v \cdot \bar{\theta}_\nu \cdot \text{Rem}^i(\text{O})^2 \qquad 6.08$$

where R_{core} is the proportionality constant (fitting constant), and $\bar{\theta}_\nu$ is normalised by dividing by the threshold energy density of 0.08 eV/atom derived from Table 5.1. Note that in equations 6.07 and 6.08, the Rem factor is squared. This was found to give a much better fit to the data than linear proportionality, although the reasons for this are not clear. The program continues with the relaxation due to overlap, without yet adding ΔN_D^i to N_D^i, but only does step 3b if the average damage level

is greater than a threshold value, which is a fitted value, determined by the damage level at which the rate of damage begins to increase, i.e., at the beginning of the "Φ^2" region, if such occurs.

$$\text{Step 3b:} \qquad \Delta N_D^i(\text{Si})_{\text{overlap}} = \frac{1}{3} R_{\text{overlap}} \cdot N_D^i(\text{tot}) \cdot \text{Rem}^i(\text{Si}) \tag{6.09}$$

$$\text{and:} \qquad \Delta N_D^i(\text{O})_{\text{overlap}} = \frac{2}{3} R_{\text{overlap}} \cdot N_D^i(\text{tot}) \cdot \text{Rem}^i(\text{O}) \tag{6.10}$$

where R_{overlap} is the proportionality factor for the overlap relaxation. Now the program adds the two relaxation damage increments to the N_D^i values. Next the program calculates the strain contribution:

$$\text{Step 4:} \qquad \Delta N_D^i(\text{Si})_{\text{strain}} = \frac{1}{3} R_{\text{strain}} \cdot N_D^i(\text{tot}) \tag{6.11}$$

$$\text{and:} \qquad \Delta N_D^i(\text{O})_{\text{strain}} = \frac{2}{3} R_{\text{strain}} \cdot N_D^i(\text{tot}) \tag{6.12}$$

where R_{strain} is the proportionality factor for the strain contribution. Note that the Rem term is not included in equations 6.11 and 6.12: this term was left out here in order to roughly account for the damage build-up beyond X_T, as well as the strain between the damaged layer and the underlying crystal. The strain contribution, added to N_D^i, produces $N_D^i(\text{apparent})$, the value determined from the RBS/channeling measurements: the strain contribution is *not* included in the N_D^i values used to calculate the next round of damage contributions.

Typical results are plotted in figures 6.1 – 6.5, and the relevant fitting parameters listed in Table 6.2. Here, 60 keV Bi^+ is representative of very high density cascades, 120 keV Bi^+ and 60 keV Kr^+ are representative of intermediate density cascades, and 120 keV Kr^+ and 35 keV He^+ are representative of the low density cascades. Note that the parameters were not fitted by an optimization routine, but

by trial and error, because of the complexity of the model: it was considered to be important that the parameters all be carefully constrained to be within physically reasonable limits. The proportionality constants R_{core}, $R_{overlap}$ and R_{strain} are dimensionless multipliers reflecting the amount by which the processes of lattice relaxation at the core of the cascades, overlap of the dilute "wings" of the cascades, and strain affect the damage as seen by RBS/channeling. The absolute value of these constants was expected to be ≤ 1, in order to be significant enough to affect the results without being so large as to swamp the other factors. In the case of the highest – density cascade, 60 keV Bi^+, R_{core} is larger than in the other fits, as might be expected: this cascade should have the largest fractional volume in which the elastically deposited energy is > 0.08 eV/atom, so the lattice relaxation effect should be dominant. In fact, Table 6.2 shows that R_{core} decreases as the cascade energy density decreases (going down the column). The other two proportionality constants seem to show no clear trend, but rather they seem to have an average value of 0.75 ± 0.24.

Table 6.2: Fitting Parameters for Quartz Damage Model

Ion	Energy keV	V_c at/mm^2	R_{core} —	$R_{overlap}$ unitless	R_{strain} —	σ_{He} mm^2	E_{He} MeV	threshold
Bi^+	60	3.3×10^4	1.5	0.51	0.51	2.0×10^{-16}	2.0	0.05
Bi^+	120	1.77×10^5	0.70	1.35	0.60	2.75×10^{-16}	1.0	0.05
Kr^+	60	1.14×10^5	0.65	0.45	1.05	2.0×10^{-16}	2.0	0.05
Kr^+	120	6.38×10^5	0.55	0.96	0.51	2.0×10^{-16}	2.0	0.07
He^+	35	5.3×10^5	0.30	0.45	0.45	2.0×10^{-16}	2.0	0.15
He^+	2000	–	–	1.20	1.05	2.0×10^{-16}	2.0	–

Note that, although the core–relaxation damage was made proportional to the elastic energy deposition density, $\bar{\theta}_\nu$, the proportionality factor R_{core} seems to

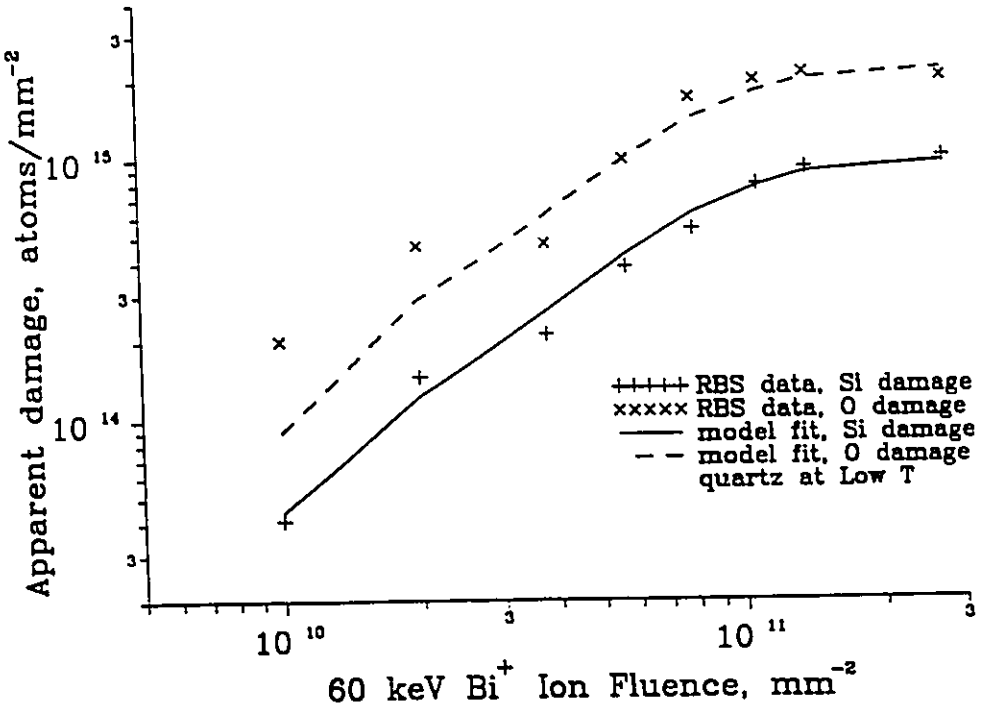

Figure 6.1: Comparison of RBS and Model Damage, 60 keV Bi

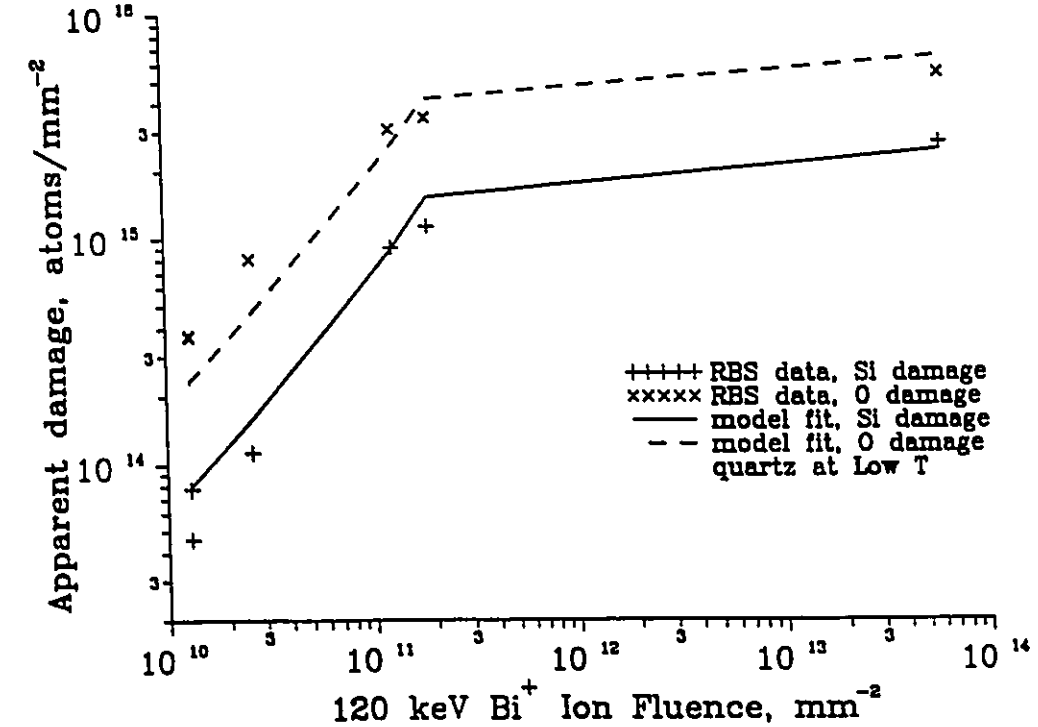

Figure 6.2: Comparison of RBS and Model Damage, 120 keV Bi

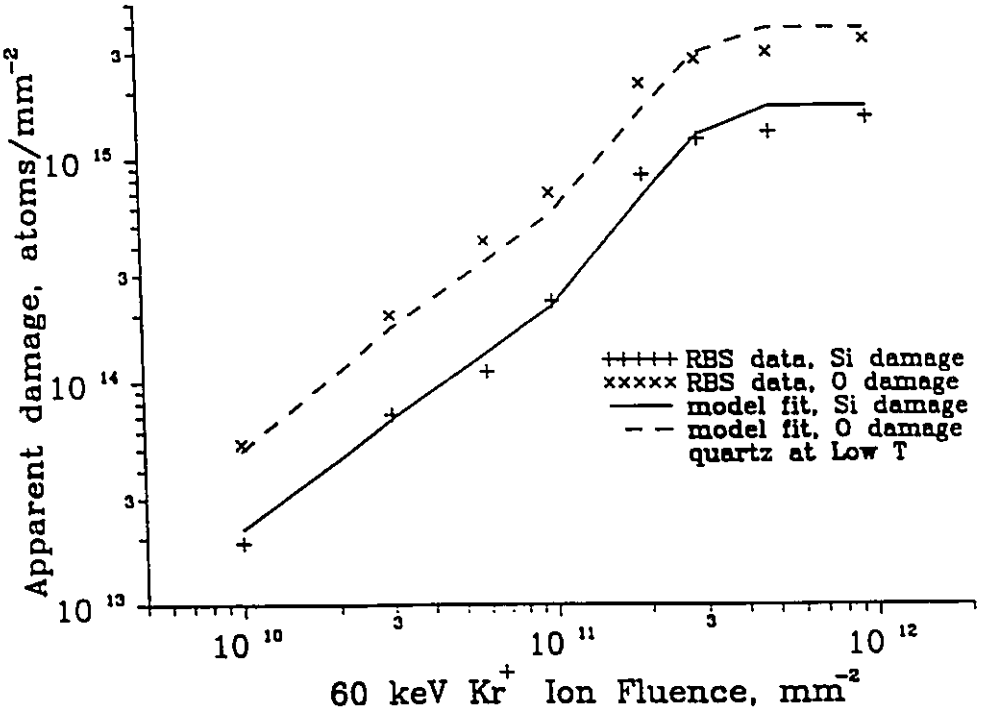

Figure 6.3: Comparison of RBS and Model Damage, 60 keV Kr

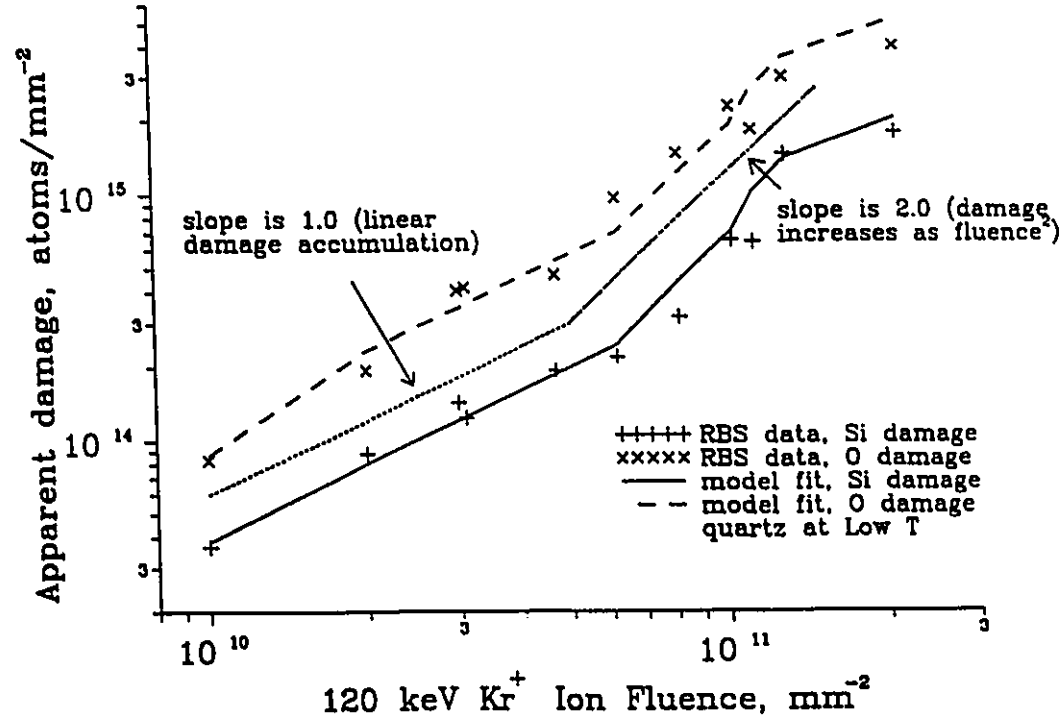

Figure 6.4: Comparison of RBS and Model Damage, 120 keV Kr

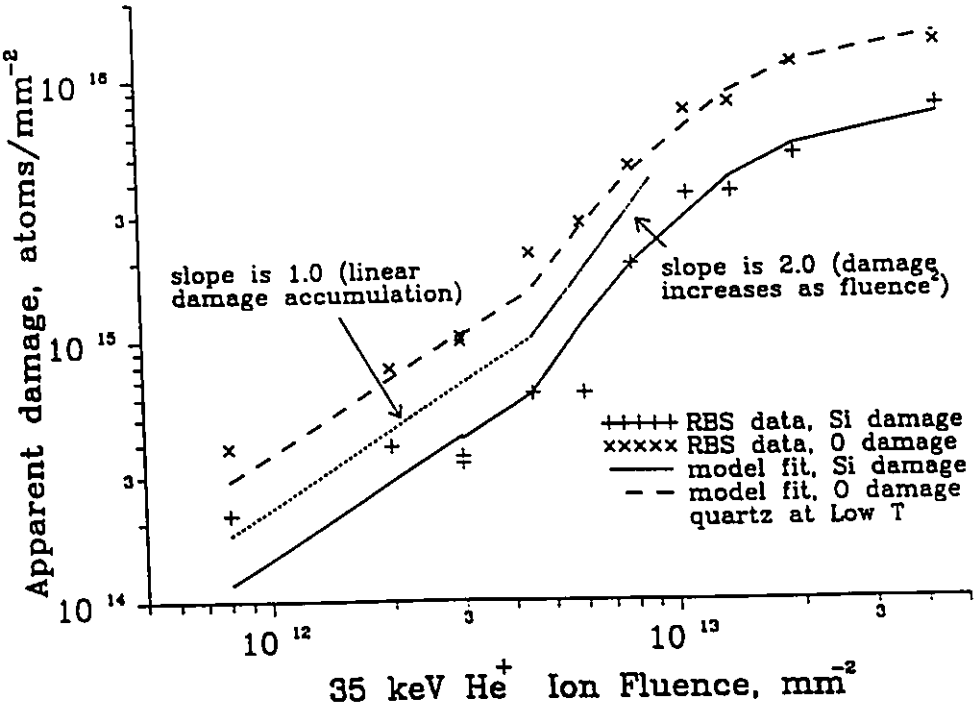

Figure 6.5: Comparison of RBS and Model Damage, 35 keV He

decrease as the energy density decreases. Also, a better fit was obtained when even the high density cascade ions had a threshold for overlap relaxation damage. As the energy density decreased, the threshold for overlap relaxation damage seemed to increase. The cross-section for 2 MeV $^4He^+$damage, σ_{He}, was determined by fitting the data in Figure 5.14; in the case where the analysis beam energy was 1 MeV, σ_{He} was multiplied by the ratio of the inelastic stopping powers of 1 and 2 MeV $^4He^+$. Attempts to confirm this experimentally were inconclusive, presumeably due to the large experimental uncertainties.

The model gives a moderately good fit to the data, with fairly reasonable variations in the fitting parameters. The model has three main fitting parameters, and several other parameters which were varied less freely, in order to fit the data. This is

justified by the large number of data parameters which had to be fit: initial damage production rates, a threshold damage level beyond which the damage rate increased, damage stoichiometry, and damage "turnover" and saturation levels. In order to improve the model it would be necessary to account for the depth profiles of the energy deposition and damage accumulation, which introduces very large uncertainties in both the theoretical distributions and the experimental data.

CHAPTER VII: CONCLUSIONS

The processes by which ions create damage in quartz are complex and interactive. There is considerable disagreement in the literature about the source of the damage (elastic vs inelastic energy deposition), about the mechanisms of damage production (point defects by elastic collisions or by radiolysis; thermal spikes; strain and various strain-induced effects, such as lattice relaxation into an amorphous state; synergistic effects of the above), and even about the definition of "amorphous" quartz. No single analysis technique seems capable of giving the full picture: channeling is strongly affected by strain, and the analysis ions create considerable damage, in a non-linear fashion; electron-microscopy requires high electron doses because of the low atomic numbers of oxygen and silicon, and creates considerable damage itself, which has only been identified as "substantially disordered or amorphous...strain centers" [Hobbs and Pascucci, 1980]; electron-spin resonance and magnetic nuclear resonance see only particular defects, and the data are subject to considerable interpretation; optical techniques and stress-induced bending [Eernisse's cantilever technique, 1974] are both subject to considerable interpretation as well.

The estimates of the average energy required to create an elastic displacement vary from 4 eV to 100 eV, and for inelastic displacements from $\sim$ 40 eV to $\sim$ 1000 eV.

Thus it is clear that, where quartz is concerned, much is not clear. However, some conclusions can be reached. The present work shows that both elastic and inelastic energy deposition create defects, and that the amount of damage created depends upon the level of damage already present, and its nature (point defects; impurities; "amorphous regions" and other extended defects, probably largely due to

the strain associated with them). The relatively large intial rates of damage and the presence of the transition from linear damage build-up ($N_D \propto \Phi$) to "super-linear" damage build-up ($N_D \propto \Phi^2$) can be modelled using two kinds of major lattice relaxation leading to the formation of amorphous micro-regions. One of these relaxation processes is due to the very high density of elastic collisions in the core of the ion damage cascade, and the other is due to the overlap of the lesser damaged "wings" of the cacades. The large non-stoichiometry present in the low-level damage of the high-density cascade data suggests that strain accounts for much of the increased damage associated with the amorphous micro-regions, since otherwise the damage would be expected to be close to stoichiometric.

In practical terms, radiation damage can be used to tailor the optical properties of quartz and other materials. This is true not only of the density (and therefore the index of refraction), but also of the other optical properties such as the polarizability [Primak, 1960, 1964, 1972a].

One of the primary factors affecting the suitability of glasses for nuclear waste disposal is the rate at which ground water might leach out of the radioactive waste. The large amounts of strain caused by radiation would be expected to increase the leaching rate, and this has been shown by Dran et al. [1980] and Stevanovic et al. [1988]. However, these results, and the results reported above, can only be used as an indicator that radiation damage might be a factor. To know how a waste system will behave probably requires engineering measurements on the specific glass/waste mixtures proposed.

Appendix I: Properties of α–Quartz and its Polymorphs

A1.1 General Properties of SiO_2 Polymorphs

At equilibrium at room temperature and pressure, a single crystal of SiO_2 is in its α–quartz phase [Weast, 1972, and Laudise, 1970]. Its lattice is composed of unit cells of three SiO_4 tetrahedra arranged spirally about the c–axis with trigonal symmetry (spatial group $32D_3$). This structure is "enantiomorphic," i.e. "left–handed" or "right–handed." resulting in properties such as optical rotation. The cell dimensions are a = 0.4913 nm and c = 0.5405 nm, so that the axial ratio is c/a = 1.100. Its density is 2.65 g/cm^3. It melts at $T_m \approx$ 1883 K, with the heat of fusion, $\Delta H_f \approx$ 56.7 cal/g, or 0.0493 eV per atom. The temperature of crystallization, T_c, has been estimated [Kelly, 1978] to be approximately $0.6 \cdot T_m \approx$ 1130 K. Its index of refraction is n = 1.554. From the difference in the electronegativities of Si and O, the simple model commonly used [Naguib and Kelly, 1975] gives an ionicity of 51% (i.e. the bonds are 49% covalent). This model would imply a charge on each silicon ion of approximtely +0.96 e, and -0.48 e on each oxygen ion [Sosman, 1965]. However, Harrison [1978] found that he could predict the band energies and bond angles much better with a model assuming an ionicity of about 20%. Much of the literature seems to assume that SiO_2 is mostly covalent.

The Debye temperature of α–quartz is approximately 487 K. The Si–O–Si bond angle is 144°; and the Si–O distance is 0.161 nm. The thermal conductivity of α–quartz is low and highly anisotropic: it reaches a maximum of about 18 W/cm·s (parallel to the c–axis) and about 10 W/cm·s (perpendicular to the c–axis) at 15 K. At room temperature these values drop to 0.14 W/cm·s (parallel) and 0.06 W/cm·s (perpendicular).

At 846 K and a pressure of one atmosphere, α–quartz transforms quickly and reversibly to β–quartz, which has the same basic structure, but is slightly less dense and has increased symmetry: in place of the threefold axis of α–quartz there is a sixfold axis in β–quartz. β-quartz has a density of 2.53 g/cm^3; a = 0.4999 nm; c = 0.5457 nm; and the axial ratio has changed by 1% to c/a = 1.092. Above approximately 1140 K, β–quartz transforms slowly to tridymite, which has a density of 2.26 g/cm^3. There are four SiO_2 tetrahedra in a unit cell, with dimensions a = 0.504 nm and c = 0.824 nm. The transformation is slow because Si–O bonds must be broken and the tetrahedra rearranged. Since the transformation is so slow, the trydimite used in phase transformation experiments is highly doped with other oxides which speed up the process; however, trydimite has never been reported as pure SiO_2: the above numbers are extrapolations to 100% SiO_2. If cooled to about 413 K, trydimite will transform (quickly and reversibly) into a low temperature form with 64 tetrahedra in a unit cell.

At 1470 K, trydimite (or β-quartz) will transform slowly into cristobalite, the highest symmetry form of SiO_2. Its density is 2.32 g/cm^3, its index of refraction is 1.486, and there are four SiO_2 tetrahedra in a unit cell, which is cubic with a = 0.713 nm. Cristobalite, too, has a low temperature form, into which it transforms quickly and reversibly at about 493 K. This low–temperature form has a Si–O–Si bond angle of 180°. Cristobalite melts at about 1996 K.

Vitreous silica (lechatelierite, or fused silica) has a density of 2.19 g/cm^3 and index of refraction of 1.459. It has no long–range order but some short–range structure: the Si–O–Si bond angle and the average Si–O distance are the same as α–quartz, 144° and 0.16 nm respectively.

Another state of SiO_2 is the "metamict" state, which is defined as the final state reached by quartz or any of its polymorphs after prolonged irradiation with energetic particles and/or photons. The metamict state is 14% less dense than α-quartz, and 3% denser than vitreous silica [Wittels and Sherrill, 1954, and EerNisse, 1974], i.e. its density is 2.26 g/cm^3.

The Si–O bond energy is about 5 eV [Hobbs and Pascucci, 1980].

A1.2 Electronic Properties of SiO_2

Estimates of the dielectric constant of α–quartz range from 3.9 – 4.7 at low frequencies ($< 10^{13}$ Hz) and 2.2 – 2.4 at optical frequencies (about 5×10^{16} Hz). The low–frequency dielectric constant of silica is approximately 3.8.

SiO_2 has an indirect band-gap of 8.5 – 9.3 eV, depending upon the method used to determine it, and a direct bandgap of about 10.5 eV. The electron mobility in silica at low fields is approximately 30 cm^2/V·s, as compared to a hole mobility of only about 1 cm^2/V·s. In contrast, Hughes, referred to in Greaves [1978], says that the hole mobility in silica at room temperature is 20 cm^2/V·s, and that it decreases as T is increased. As measured by optical phonon scattering the mean–free–path of electrons is about 2 nm.

The above mobilities were determined by defect scattering, and are reduced by up to a factor of 10^5 by radiation damage or the introduction of impurities such as Na, Al and H_2O. (Alfred et al. [1978] found that the surface 20 nm or so of quartz crystals, both natural and hydrothermally grown, contained about 13 atomic per cent of hydrogen, which corresponds to slightly less than one H_2O molecule per four SiO_2 molecules; they also determined that the concentration in the surface 200 nm was 4 – 5 atomic per cent hydrogen, and one atomic per cent in the bulk of the crystals.)

The electrical conductivity of quartz is approximately one thousand times greater parallel to the c–axis than perpendicular to it [King et al.. 1983], indicating the strong anisotropy of quartz.

Appendix II: Calculations of Damage Effects on Displacement Rates

The simplest case would be for a dilute cascade, such as that created by 35 keV $^4He^+$ ions in quartz, which are expected to produce an average of about 0.004% defects in the silicon sub–lattice and 0.008% defects in the oxygen sub–lattice. This was determined using the modified Kinchin–Pease theory, as in section 6.3.1, to get the number of displacements per ion, and $V_c \cdot R_v$, the approximate volume of an individual cascade, as in section 2.2.5 (R_v is so small that it is very approximate in the case of 35 keV He ions). Now, by factor (a) from section 6.3.2, where the rate of damage is reduced by the fractional damage present: $\frac{dN_D}{d\Phi}$ becomes $\left(\frac{dN_D}{d\Phi}\right)_{\Phi \to 0} \cdot \left(1 - \frac{N_D}{N_{SAT}}\right)$. By factor (b) from section 6.3.2, where atoms neighboring on vacancies have reduced displacement energies because of fewer bonds: E_d becomes $E_d^o\left(1 - \frac{n_1 N_D}{N_{SAT}} + f \cdot \frac{n_1 N_D}{N_{SAT}}\right)$. The first part, $1 - \frac{n_1 N_D}{N_{SAT}}$, is the fraction of atoms which do not neighbor on vacancies; the last term is the fraction of atoms which do neighbor on vacancies, times the fractional change in the displacement energy. Here, n_1 is the number of atoms affected by the removal of one atom from its lattice position, f is the ratio of the modified displacement energy to the original displacement energy, E_d^o, and N_{SAT} is the number of atoms (silicon or oxygen) in the target over the range in which the ions are creating damage; for silicon, $N_{SAT} = X_T/3$; for oxygen, $N_{SAT} = X_T \cdot \frac{2}{3}$. It is assumed that the elastically deposited energy is distributed uniformly amoung the atoms in the cascade, i.e., two–thirds of the energy goes towards displacing oxygen atoms, and one–third goes towards displacing silicon atoms, because there are twice as many oxygen atoms as silicon atoms. Parkin [1990] indicates that this is a reasonable assumption for oxides, as long as the mass ratio of the elements is < 2; for quartz, $M_{Si}/M_O = 1.75$.

Note that the above factors would only apply when the amount of damage present is small, i.e., in dilute cascades at low ion fluences. Then, by applying factor (b) to equation 2.41, one obtains:

$$\left(\frac{dN_D}{d\Phi}\right)_b = \frac{\left(\frac{dN_D}{d\Phi}\right)_{KP}}{1+\frac{(f-1)n_1 N_D}{N_{SAT}}} \qquad A2.1$$

Since oxygen only has two bonds, the simplest approximation would be that it has three bonding states: normal, with $E_d^o = 2 \times 5$ eV $= 10$ eV; single–bonded, when a neighbouring Si atom has been displaced, with $E_d^o = 1 \times 5$ eV $= 5$ eV, and therefore $f = \frac{1}{2}$; and no–bond, i.e., displaced. Oxygen atoms bond only to silicon atoms in a perfect quartz crystal, so the only time one would get single–bonded oxygen atoms is when a silicon atom has been displaced, or possibly when an ionization event is followed by significant relaxation. The former would create four such single–bonded oxygens, so $n_1 = 4$. Therefore, in the simplest case, $\frac{dN_D}{d\Phi}$ for oxygen would become:

$$\left(\frac{dN_D}{d\Phi}\right)_{KP} \frac{1-\frac{N_D(O)}{N_{SAT}(O)}}{1+\left(\frac{1}{2}4-4\right)\frac{N_D(Si)}{N_{SAT}(Si)}} = \left(\frac{dN_D}{d\Phi}\right)_{KP} \frac{1-\frac{N_D(O)}{N_{SAT}(O)}}{1-2\frac{N_D(Si)}{N_{SAT}(Si)}} \qquad A2.2$$

As shown in section 6.3.1, equation 2.41 predicts that $N_D(O) = 4N_D(Si)$; and in quartz $N_{SAT}(O) = 2N_{SAT}(Si)$. Thus, $\frac{N_D(O)}{N_{SAT}(O)} = \frac{2N_D(Si)}{N_{SAT}(Si)}$, and $\frac{dN_D}{d\Phi}$ is unchanged: the effects of factor (a) and factor (b) simply cancel each other in a dilute cascade.

Similarly, for $\frac{dN_D}{d\Phi}(Si)$, there is again no change in $\frac{dN_D}{d\Phi}(Si)$, as long as $\frac{N_D(O)}{N_{SAT}(O)}$ is small enough that one can assume that the vast majority of oxygen vacancies are isolated. In this case, for every oxygen vacancy there are two silicon atoms with a missing bond, and thus $n_1 = 2$, and $f = \frac{3}{4}$.

As $N_D(O)$ increases the fraction of silicon atoms with two or more dangling bonds would increase. However, the average fractional decrease in the value of $E_d(Si)$ would continue to be the same as the increase in the fractional oxygen damage. For

example, in the above–mentioned case, one might assume that most oxygen vacancies were isolated, at a dose where there were about 5% oxygen vacancies and 2.5% silicon vacancies. Then factor (a) would reduce $\frac{dN_D}{d\Phi}$ by 2.5%, and factor (b) would reduce $E_d(Si)$ by:

$$\frac{1}{2} \cdot \frac{N_D(O)}{N_{\mathrm{SAT}}(O)} = \frac{1}{2} \cdot 5\% = 2.5\%$$

thereby cancelling factor (a). Now, at some higher dose one would expect a mixture of isolated and neighbouring oxygen vacancies, say, $X_1\%$ isolated and $X_2\%$ neighbouring, where $X_1\% + X_2\% = \frac{N_D(O)}{N_{\mathrm{SAT}}(O)} \cdot 100\%$. The fraction of silicon atoms with one bond missing would be $2X_1\% + X_2\%$, and the number of silicon atoms with two bonds missing would be $\frac{X_2\%}{2}$, as can be seen by looking at the quartz crystal structure diagram, figure 3.10. Then the reduction multiplier for $E_d(Si)$ would be:

$$\frac{1}{4}(2X_1\% + X_2\%) + \frac{1}{2} \cdot \frac{1}{2} \cdot X_2\% = \frac{1}{2}X_1\% + \frac{1}{2}X_2\% = \frac{1}{2}(X_1\% + X_2\%) = \frac{1}{2}\frac{N_D(O)}{N_{\mathrm{SAT}}(O)} \qquad A2.3$$

just as in the simple case. This would also apply to the case where a silicon atom was lacking three of its bonds.

Hence there would be no change in $\frac{dN_D}{d\Phi}$ or on $\frac{N_D(O)}{N_D(Si)}$ until $N_D(O)$ reached a value such that there would be a significant chance of an atom being displaced when nearby damage has created enough strain to reduce the effective bonding energy significantly, causing the damage rate to increase. This might occur at an average damage level as low as approximately 2 – 10% in a dilute cascade, and probably would always occur within dense cascades.

REFERENCES

Abel, F., Amsel, G., Bruneaux, M., d'Artemare, E., J. Phys. Chem. Sol. 30 (1969) 687.

Abel, F., Amsel, G., Bruneaux, M., Cohen, C., Rad. Eff. 12 (1972) 35.

Alfred, D.D., White, C.W., "H–Profiles in SiO_2 by Nuclear Reaction Analysis", The Physics of SiO_2 and Its Interfaces, S.T. Pantclides, ed. New York: Pergammon Press, (1978).

Armstrong, B.H., "Thermal Conductivity of SiO_2", The Physics of SiO_2 and Its Interfaces, S.T. Pantelides, ed. New York: Pergammon Press, (1978).

Arnold, G.W., Mazzoldi, P., in Ion Beam Modification of Insulators, P. Mazzoldi and G.W. Arnold, ed. New York: Elsevier Press, (1987).

Baroody, E.M., J. Appl. Phys. 36 (1965) 3562.

Barrett, J.V., Phys. Rev. B3 (1971) 152–157.

Beez, H., Fasold, D., Karge, H., phys. stat. sol. (a) 76 (1983) K171.

Biersack, J.P., Städele, M., Phys. Rev. 120 (1960) 1744.

Biersack, J.P., in Ion Beam Modification of Insulators, P. Mazzoldi and G.W. Arnold, ed. New York: Elsevier Press, (1987).

Block, W., Meissner, M., Spitzman, K., "K of SiO_2, Transitory and Static", The Physics of SiO_2 and Its Interfaces, S.T. Pantelides, ed. New York: Pergammon Press, (1978).

Born, M., Mayer, J.E., Z. Physik 75 (1932) 96.

Bragg, W.H., Kleeman, R., Phil. Mag. 10 (1905) 318.

Brandt, W., Kitigawa, M., Phys. Rev. 25B (1982) 5631.

Briggs, J.S., Pathak, A.P., J. Phys. C.6 (1973) L153.

Brinkman, J.A., J. Appl. Phys. 25 (1954) 961.

Brinkman, J.A., Amer. J. Phys. 24 (1956) 246.

Carrière, B., Lang, B., Surf. Sci. 64 (1977) 209

Carter, G. Ion Implantation of Semiconductors, New York: Wiley Press, (1976)

Carter, G., Armour, D.G., Donnelly, S.E., Webb, R., Rad. Eff. 36 (1978) 1.

Chang, C.C., Surf. Sci. 25 (1971) 149

Cheshire, I.M., Dearnaley, G., Poate, J.M. Phys., Lett. 27A (1968) 304.

Chu, W., Mayer, J.W., Nicolet, M.A., Backscattering Spectrometry. New York: Academic Press, (1978).

Clark, G., Morgan, D.V., Poate, J.M., "Energy Loss of Channeled Protons in the MeV Region", Atomic Collision Phenomena in Solids, D.W. Palmer, M.W. Thompson, P.D. Townsend, eds. Amsterdam: North Holland Publishing Co., (1970).

Collins, R., Rad. Eff. 37 (1978) 13.

Das, G., Mitchell, T.E., Rad. Eff. 23 (1974) 49

Datz, S., Mock, C.D., Appleton, B.R., Robinson, M.T., Oen, O.S.,"Energy Dependence of Channeled Energy Loss Spectra", Atomic Collision Phenomena in Solids, D.W. Palmer, M.W. Thompson, P.D. Townsend, eds. Amsterdam: North Holland Publishing Co., (1970).

Davies, J.A., Denhartog, J., Eriksson, L., Mayer, J.W., Can. J. Phys. 45 (1967) 4053.

Davies, J.A., Material Characterization Using Ion Beams, J.P. Thomas, A. Chachard, eds. New York: Plenum Press, (1978).

Davies, J.A., Böttinger, J., Hoffer, W., Littmark, U., "Collision Cascades and Spike Effects", NATO Advanced Study Institute Proceedings on "Surface Modification and Alloying", Trevi, Italy. J.M. Poate, G. Foti, D.C. Jacobson, eds., New York: Plenum Press, (1983).

Devine, R.A.B., Nucl. Instr. and Meth. in Phys. Res. B46 (1990) 245.

Dexter, D.L., Phys. Rev. 118 (1960) 934.

Dran, J.C., Maurette, M., Petit, J.C., Science 209 (1980) 1518.

Drigo, A.V., Russo, S.L., Mazzoldi, P., Goode, P.D., Hartley N. Rad. Eff. 33 (1977) 161.

Ecuyer, J.L., Matsunami, M., Davies, J.A., Nucl. Instr. Meth. 160 (1979) 337.

EerNisse, E.P., J. Appl. Phys. 45 (1974) 167.

Eisen, F.H., "Chapter 14", Channeling, ed. D.V. Morgan. New York: Wiley Press, (1973).

Eisen, F.H. Phys. Rev. Lett. 23 (1966) 401.

Feigl, Fowler and Yip, Sol. State Commun. 14 (1974) 225

Feldman, L.C., Mayer, J.W., Picraux, S.T., Materials Analysis by Ion Channeling. Toronto: New York: Academic Press, (1982).

Firsov, O.B., Sov. Phys. JETP 6 (1958) 534.

Fischer, H., Götz, G., Karge, H. phys. stat. sol. (a) 76 (1983a) 249.

Fischer, H., Götz, G., Karge, H. phys. stat. sol. (a) 76 (1983b) 493.

Fleischer, R.L., Price, P.B., Walker, R.M., Ann. Rev. Sci. U.S.A. 15 (1965) 1.

Fleischer, R.L., Price, P.B., Walker, R.M., J. Appl. Phys. 36 (1968) 3645.

Freibele, E.J., Griscom, D.L., Staplebroek, M., Weeks, R.A., Phys. Rev. Lett. 42 (1979) 1346.

Gibbons, J.F., Proc. IEEE, 60 (1972) 1062.

Goldstein, H., Classical Mechanics. Cambridge, Mass.: Addison-Wesley, (1958).

Gombas, P., Handbuch der Physik, 36th edition. Berlin: Springer, (1956).

Greaves, G.N., Phil. Mag. B37 (1978) 447.

Griscom, D.L., Nucl. Instr. and Meth. in Phys. Res. B1 (1984) 481.

Griscom, D.L., in The Southwest Conference on Otics: Radiation Effects on Optical Materials, P. Levy, ed. Proc. SPIE 541 (1985) 38.

Haff, P.K., Appl. Phys. Lett. 31 (1977) 259.

Harrison, W.A., "Is SiO_2 Covalent or Ionic?" The Physics of SiO_2 and Its Interfaces, S.T. Pantelides, ed. New York: Pergammon Press, (1978).

Hartree, D.R., Calculations of Atomic Structures. New York: Wiley and Sons, (1957).

Hines, R. L., Arndt, R., Phys. Rev. 119 (1960) 623

Hobbs, L.W.., Pascucci, M.R., J. de Physique, Colloque C6–238 (1980).

Howard, R.E., Smoluchowski, R., Phys. Rev. 116 (1959) 314.

Howard, R.E., Vosko, S., Smoluchowski, R., Phys. Rev. 122 (1961) 1406.

Howitt, D.G., DeNatale, J.F., Radiat. Phys. Chem. 21 (1983) 445

Hvelpund, P., Fastrup, B., Phys Rev. 165 (1968) 408.

Izumi, T., Taku, T., Matsumori, T., Proc. Int. Conf. Ion Implant. in Semicond., ed. F. Chernov, J.A. Borders, D.K. Brice, Plenum Press, New York, (1977).

Jollet, F., Duraud, J.P., Noguera, C., Dooryhee, E., Langevin, Y., Nucl. Instr. and Meth. in Phys. Res. B46 (1990) 125.

Katenkamp, U., Karge, H., Prager, R., Rad. Eff. 48 (1980) 31

Kelly, R., Lam, N.Q., Rad. Eff. 19 (1973) 39.

Kelly, R., Nucl. Instr. Meth. 149 (1978) 553.

Kinchin, G.H., Pease, R.S., Rep. Prog. Phys. 18 (1955) 143.

King, B.V., Kelly, J.C., Dalglish, R.L., Nucl. Instr. Meth. 209/210 (1983) 1135.

Kool, W. H., Roosendahl, H.E., Wiggers, L.W., Saris, F.W., Nucl. Instr. Meth. 132 (1976) 285

Kool, W. H., Roosendahl, H.E., Wiggers, L.W., Saris, F.W., Rad. Eff. 36 (1978) 41.

Krefft, G.B., Beezhold, W., EerNisse, E.P., IEEE Trans. Nucl. Sci. NS-22 (1975) 2247.

Laudise, R.A., Growth of Single Crystals, Prentice-Hall, N.J., (1970).

L'Hoir, A., Cohen, C., Amsel, G., Proc. Second Conf. Ion Beam Surf. Layer Analysis, Karlsruhe, Plenum, (1975).

Lindhard, J., Scharff, M., Phys Rev. 124 (1961) 128.

Lindhard, J., Scharff, M., Schiott, H.E., Kgl. Dan. Vid. Selsk. Mat. Fys. Medd. 33 #14 (1963a).

Lindhard, J., Nielson, V., Scharff, M., Kgl. Dan. Vid. Selsk. Mat. Fys. Medd. 33 #10 (1963b).

Lindhard, J., Kgl. Dan. Vid. Selsk. Mat. Fys. Medd., 34 #14 (1965).

Lindhard, J., Nielson, V., Scharff, M., Kgl. Dan. Vid. Selsk. Mat. Fys. Medd. 36 #10 (1968).

Macaulay-Newcombe, R.G., Thompson, D.A., Nucl. Instr. and Meth. in Phys. Res. B1 (1984) 176.

Macaulay-Newcombe, R.G., Thompson, D.A., Davies, J.A., Stevanovic, D.V., Nucl. Instr. and Meth. in Phys. Res. B46 (1990) 180.

Matzke, Hj., phys. stat. sol. 18 (1966) 285.

Matzke, Hj., Whitton, J.L., Can. J. Phys. 44 (1966) 995.

Mayer, J.W., Eriksson, L., Picraux, S.T., Davies, J.A., Can. J. Phys. 46 (1968) 663.

Mayer, J.W., Rimini, E., Ion Beam Handbook for Material Analysis. New York: Academic Press, (1977).

Meyer, L., phys. stat. sol. 44 (1971) 253.

Molière, G., Z. Naturforsch 20 (1947) 133.

Monnin, M., Radiat. Res. 59 (1973) 291.

Morgan, D.V., ed., Channeling, Wiley Press, New York, (1973).

Morgan, D.V., Van Vliet, D., Contemp. Phys. 11 (1970) 173.

Naguib, H.M., Kelly, R., Rad. Eff. 25 (1975) 1.

Nishimura, T., Aritome, H., Masuda, K., Namba, S., Japan J. Appl. Phys. 13 (1974) 1317.

Norris, C.B., EerNisse, E.P., J. Appl. Phys. 45 (1974) 3876

Northcliffe, L.C., Phys. Rev. 120 (1960) 1744.

Pages, L., Bertel, E., Joffre, H., Sklavenitis, L., Atomic Data 4 (1972) 1.

Palmer, D.W., d'Artemare, E., Phil. Mag. 17 (1968) 1165.

Parikh, N.R., Ion Implantation Damage in CdS Using TEM and RBS/Channeling Ph.D. Thesis, (1985), Dept. Metallurgy and Materials Science, McMaster University, Hamilton, Ontario, Canada.

Parkin, D.M., Nucl. Instr. and Meth. in Phys. Res. B46 (1990) 26. Pickering, H.W., J. Vac. Sci. Tech. 13 (1976) 618.

Primak, W., Phys. Rev. 110 (1958) 1240.

Primak, W., J. Phys. Chem. Sol. 13 (1960) 279.

Primak, W., J. Appl. Phys. 35 (1964) 1342.

Primak, W., Phys. Rev. B.6 (1972a) 4846.

Primak, W., J. Appl. Phys. 43 (1972b) 2745.

Primak, W., Phys. Rev. B.14 (1976) 4679.

Quéré, Y., Radiat. Eff. Lett. 28 (1976) 253.

Revesz, A.G., J. Non-Cryst. Solids 13 (1973) 309.

Robinson, M.T., Proc. Brit. Nucl. Energy Soc. Conf. Nucl. Fusion Reactors. New York: Abingdon Press, (1969).

Seitz, F., Koehler, J.S., Prog. Sol. State Phys. 2 (1956) 305.

Shimizu, H., Ono, M., Nakayama, K., Surf. Sci. 36 (1973) 817.

Sigmund, P., Inelastic Ion-Surface Collisions. eds. N.H. Tolk, J.C. Tully, W. Heiland, C.W. White. New York: Academic Press, (1977).

Sigmund, P., Appl. Phys. Lett. 14 (1969a) 114.

Sigmund, P., Phys. Rev. 184 (1969b) 383.

Sigmund, P., Phys. Rev. 184 (1969c) 396.

Sigmund, P., Scheidler, G.P., Roth, G., BNL 50083. C-52 (1968) 374.

Sigmund, P., Winterbon, K.B., Nucl. Instr. Meth. 119 (1974) 541.

Sosman, R.B., The Phases of Silica, Rutgers University Press, New Brunswick, N.J., (1975).

Stevanovic D.V., Tognetti, N.P., Carter, G., Christodoulides, C.E., Ibrahim, A.M., Thompson, D.A., Rad. Eff. 71 (1983) 95.

Stevanovic, D.V., Thompson, D.A., Vance, E.R., J. Nucl. Mat. 161 (1989) 169.

Swanson, M.L., Parsons, J.R., Hoelke, C.W., Radiat. Eff. 9 (1974) 249.

Tait, J.C., W.N.R.E., Pinawa, Manitoba, Canada: private communication to M.P. Puls, (1981).

Tanimura, K., Tanaka, T., Itoh, N., Phys. Rev. Lett. 51 (1983) 423.

Tanimura, K., Tanaka, T., Itoh, N. Nucl. Instr. Meth. in Phys. Res. B1 (1984) 187.

Thomas, S., J. Appl. Phys. 45 (1974) 161.

Thompson, D.A., Rad. Eff. 56 (1981) 105.

Thompson, D.A., Walker, R.S., Davies, J.A., Rad. Eff. 32 (1977a) 135.

Thompson, D.A., Robinson, J.E., Walker, R.S., Rad. Eff. 32 (1977b) 169.

Thompson, D.A., Walker, R.S., Rad. Eff. 36 (1978) 91.

Thompson, D.A., Golanski, A., Haugen, H.K., Stevanovic, D.V., Carter, G., Christodoulides, C.E., Radiat. Eff. 52 (1980) 69

Thompson, M.W., Defects and Radiation Damage in Metals. London: Cambridge University Press, (1969).

Toulemonde, M., Balanzat, E., Bouffard, S., Grob, J.J., Hage-Ali, M., Stoquert, J.P., Nucl. Instr. and Meth. in Phys. Res. B46 (1990) 64.

Townsend, P.D., Rep. Prog. Phys. 50 (1987) 501.

Townsend, P.D., Nucl. Instr. and Meth. in Phys. Res. B46 (1990) 18. Varley, J.H.O., Nature. 174 (1954a) 886.

Varley, J.H.O., J. Nucl. Energy. 1 (1954b) 130.

Walker, R.S., Thompson, D.A., Poehlman, F.W.S., Rad. Eff. 34 (1977) 157.

Walker, R.S., Ion Implantation Damage in Semiconductors at Low Temperatures, Ph.D. thesis, (1977) Dept. of Electrical Engineering, McMaster University, Hamilton, Ontario, Canada.

Weast, R.C., C.R.C. Handbook of Chemistry and Physics (1972) B133.

Webb, R., Carter, G., Collins, R., Rad. Eff. 39 (1978) 129.

Wiggers, L.W., Koekkoek, H.G., Buth, A.H., Saris, F.W., Roosendahl, H.E., Rad. Eff. 42 (1979) 77.

Williams, F.E., Phys. Rev. 126 (1962) 70.

Winterbon, K.B., Ion Implantation Range and Energy Deposition Distributions, vol 2. New York: Plenum, (1975).

Winterbon, K.B., Rad. Eff. 30 (1976) 199.

Winterbon, K.B., Sigmund, P., Sanders, J.B., Kgl. Dan. Vid. Selsk. Mat. Fys. Medd. 37 #14 (1970).

Wittels, M., Sherrill, F.A., Phys. Rev. 92 (1954) 1117.

Young, R.A., Post, B., Acta. Cryst. 15 (1962) 337.

Ziegler, J.F., Chu, W.K., Atomic Data and Nuclei Data Tables. 13 (1974) 463.

Ziegler, J.F., Biersack, J.P., Littmark, U., Vol. I of the series, Stopping Power and Ranges of Ions in Matter, J.F Ziegler, ed. New York: Pergammon Press, (1985).